Title

Soft Materials meet Active Matter: Sticky Colloids in a Bacterial Bath

Author

Grober, Daniel

Publication Date

2023

UNIVERSITY OF CALIFORNIA SAN DIEGO

Soft Materials meet Active Matter: Sticky Colloids in a Bacterial Bath

A dissertation submitted in partial satisfaction of the
requirements for the degree Doctor of Philosophy

in

Physics

by

Daniel Grober

Committee in charge:

Professor Jérémie Palacci, Chair
Professor Michael Sailor
Professor David Saintillan
Professor Mattia Serra
Professor Oleg Shpyrko

2023

The Dissertation of Daniel Grober is approved, and it is acceptable in quality and form for publication on microfilm and electronically.

University of California San Diego

2023

EPIGRAPH

So it goes

Kurt Vonnegut

TABLE OF CONTENTS

LIST OF FIGURES

LIST OF SUPPLEMENTAL MOVIES

Movie S1: (Experiment) Comparison of aggregation in thermal versus active baths. Sticky colloids aggregate in either a thermal (ρ_B=0) or active bath of swimming *E. coli* ($\rho_B = 0.5\rho^*$).

Movie S2: (Experiment) An accelerated video of sticky colloids in the active bath of swimming *E. coli* ($\rho_B = \rho^*$), which highlights the persistent clockwise motion of the aggregates..

Movie S3: (Simulation) Conventional aggregation in a thermal bath. The internal torque for each particle is set to $0\,k_\mathrm{B}T$.

Movie S4: (Simulation) Aggregation at low activity. The internal torque for each particle is set to $1\,k_\mathrm{B}T$.

Movie S5: (Simulation) Aggregation at high activity. The internal torque for each particle is set to $10\,k_\mathrm{B}T$.

Movie S6: (Simulation) Zoomed in view of aggregation and folding at high activity. The internal torque for each particle is set to $10\,k_\mathrm{B}T$).

Movie S7 (Simulation) Mechanical test of a gel assembled in thermal conditions. The gel was previously assembled with the internal torque for each particle is set to $0\,k_\mathrm{B}T$, and the internal torque remains at $0\,k_\mathrm{B}T$ during the stretching experiment.

Movie S8 (Simulation) Mechanical test of a gel assembled in active conditions. The gel is previously assembled in active conditions (the internal torque for each particle is set to $3\,k_\mathrm{B}T$), and the internal torque is set to $0\,k_\mathrm{B}T$ during the stretching experiment.

ACKNOWLEDGEMENTS

First and foremost, I would like to acknowledge my advisor, Professor Jérémie Palacci. Thank you for your patience, guidance, and most importantly your enthusiasm to engage in rigorous debate during the past few years.

I owe Ivan Palaia and Mehmet Can Ucar a debt of gratitude for their tireless effort on our paper. Additionally, I would like to acknowledge all my colleagues in Materiali Molli Lab. Specifically, Quentin Martinet, Iaroslava Golovkova, Mac Huang, and Antoine Aubret have been exceptional mentors and role models during my PhD.

I would not have made it this far without my friends, both in San Diego and Vienna. Max Poore and Palka Puri, thank you both for your companionship during many long nights in our first years at UCSD. Scott Conrad, thank you for being a weird dude and an amazing friend. Heloisa Chiossi, Nick Machnik, Nina Thür and Sam Scudder, thank you for many soft catches and long talks in the woods. Andreas Ehrmann and Jonny Scott, thank you for skiing Breite Ries with me next winter. Last but not least my sister, Jenny Grober, for consistently exposing me to a different way of looking at the world.

Finally, I would like to acknowledge my parents, Bob and Louise Grober. I was lucky enough to be raised by two Physicists, in a household which always valued science and encouraged curiosity. The more I see of the world, the more I appreciate the way you two raised me.

Chapter 3, in full, is a reprint of the material as it may appear in Nature Physics, 2023. Daniel Grober, Ivan Palaia, Mehmet Can Ucar, Edouard Hannezo, Anđela Šarić, Jérémie Palacci. The dissertation author was the primary investigator and author of this paper.

Chapters 2, 4, and 5, in part, contains material as it may appear in Nature Physics, 2023. Daniel Grober, Ivan Palaia, Mehmet Can Ucar, Edouard Hannezo, Anđela Šarić, Jérémie Palacci. The dissertation author was the primary investigator and author of this paper.

VITA

2017	Bachelor of Engineering, University of Illinois - Urbana Champaign
2018–2023	Doctoral Researcher, University of California San Diego
2021-2023	Predoctoral Visiting Scientist, Institute of Science and Technology Austria
2023	Doctor of Philosophy, University of California San Diego

PUBLICATIONS

“Unconventional colloidal aggregation in chiral bacterial baths”,
Daniel Grober, Ivan Palaia, Mehmet Can Ucar, Edouard Hannezo, Anđela Šarić, Jérémie Palacci,
in press Nature Physics 2023

FIELDS OF STUDY

Major Field: Physics

ABSTRACT OF THE DISSERTATION

Soft Materials meet Active Matter: Sticky Colloids in a Bacterial Bath

by

Daniel Grober

Doctor of Philosophy in Physics

University of California San Diego, 2023

Professor Jérémie Palacci, Chair

This thesis is an experimental work, investigating how active matter can control the assembly of soft materials. We design a novel experimental system, combining sticky colloids sedimented on the bottom surface of a glass capillary with a bath of motile *E. coli*. The colloids diffuse and stick together, assembling into large, quasi - 2D aggregates. Motile *E. coli* generate forces and flows in the surrounding media: an active bath which injects energy into the system through mechanical work. In the active bath, aggregates exhibit a a persistent clockwise rotation, leading to a non-conventional aggregation mechanism. These aggregates form structures which are not accessible via conventional aggregation in a thermal bath. Aided by numerical simulation of spinning, sticky beads, we elucidate that the rotation and folding of aggregates is the salient

feature driving the structural differences, and the activity of the bath controls the phase diagram of aggregation. Further experiments indicate that the bacteria collide with and then swim through the aggregates; additionally, the direction of rotation of the aggregates is correlated with the direction of the circular trajectories made by the *E. coli* bacteria. Based on these insights, we propose a simple model for the swimmer-aggregate interactions, and propose further experiments to test its validity. As a whole, this work constitutes a proof of concept that active matter can be harnessed to direct the assembly of soft materials. The experiments presented in this thesis lay the groundwork for the development of a new class active, soft materials, whose structure and mechanical properties are dictated by their assembly in an active bath.

Introduction

Dating back to early civilization, artists and craftsmen have used repeated heating and cooling cycles to hone the properties of metals. During the annealing process, energy is injected into the system, re-arranging the microscopic structure of the material and controlling its mechanical response. This thesis envisions the transfer of such concept to soft materials (i.e. gels) using small, self propelled particles (active matter) contained inside the material to agitate and re-organize the structure from within. From the outset, this thesis poses the question: can we leverage active matter to exact microscopic control over soft materials? This approach is supported by a scaling argument, comparing the typical elastic modulus of soft matter with the pushing pressure of active matter.

Soft matter encompasses a wide range of materials, from hummus to the LCD screen on your phone. These materials tend to have two things in common: a characteristic energy scale on the order of $k_{\mathrm{B}}T$, and a mesoscopic length scale on the order of µm [1, 2]. Through dimensional analysis, the elastic modulus (units energy per volume) can be estimated as $G \sim k_{\mathrm{B}}T/\mu\mathrm{m}^3$ leading to typical values on the order Pa.

Active matter is a broad term, defining particles which convert energy into motion [3]. Typical length scales of these particles are on the order $\ell \sim \mu\mathrm{m}$, with swimming speeds $v \sim 10\mu\mathrm{m\,s}^{-1}$. The pushing force of a micron scale particle can be estimated from Stokes drag, $F \sim 6\pi\eta\ell v$, with typical values on the order pN. This leads to a pressure (F/ℓ^2), once again on the order Pa. Through the lens of this argument, it appears possible to leverage active matter to shape soft materials. This scaling argument constitutes the motivation and thrust of this work. The development of a soft material, where the material properties are tuned by controlling the active matter within, would provide a new knob of control over material properties and represent a major shift in Materials Science.

This thesis is an experimental work, and completion of this ambitious goal requires the development of an experimental system, accompanied by techniques to study it. To this end, we define the three key pieces of our experimental system. First are passive, micrometer scale building blocks, which form the structure of the material. Second are interactions between the building blocks; we leverage an attractive potential to bind the building blocks together, allowing them to self-assemble into a macroscopic material. Finally, we need a source of energy; active matter provides a means to inject energy into the material from within.

In the interest of developing an experimental system which has potential to upscale at a later stage, we restrict ourselves to commonly available materials. We use micron scale particles (colloids) for building blocks; colloids of a variety of shapes, sizes and materials can be readily obtained (either commercially or synthesized in house) in macroscopic quantities. Long polymers provide interactions between the building blocks, through the depletion interaction, which is detailed later in the thesis. We use *E. coli* bacteria as an ideal active particle to inject energy into the system, having a large toolbox of biological techniques to tune their activity.

This approach is novel and, by design, this experimental work sits at the interface between a few different fields of science, borrowing elements from Physics, Chemistry and Biology. For this reason, in the first chapters of this thesis we will build a foundation, onto which the main findings can be presented and understood. Chapter 1 reviews meaningful concepts relevant to designing the experimental system, and Chapter 2 describes control and calibration experiments, used to develop a toolbox of techniques for studying the system. Having built a solid foundation, the following chapters describe experiments studying the aggregation of sticky colloids in a bacterial bath. Chapter 3 is a verbatim reprint of the paper "Non-conventional colloidal aggregation in chiral bacterial baths". Chapters 4 and 5 discuss in detail further experiments which are presented in the supplemental text of the paper. The thesis concludes with Chapter 6, where we reflect on our work and propose future steps for this project. Chapter 7 contains derivations to equations used throughout the work, and is included primarily as a reference for future students. The end of each chapter contains a short summary, outlining the salient information.

Chapter 1

Conceptual motivation behind experimental design

To our knowledge, there are few experimental systems similar to the proposed experiment: passive building blocks, self-assembled in an active suspension of *E. coli* bacteria. The following section outlines the conceptual motivation behind our experimental design. Along the way we borrow concepts from Physics, Chemistry and Biology, to design a system where we can study the interplay between soft materials and active matter. This section begins by discussing the properties of passive micro-scale matter (Section 1.1), followed by the interactions at play at this length scale (Section 1.2). Section 1.3 discusses how *E. coli* cam be used as an active bath to direct colloidal assembly. Finally, Section 1.4 reviews two conceptually similar experimental works, each harnessing active matter to inject energy into a soft matter system.

1.1 Micro-metric building blocks: Colloids

Colloids are broadly defined as solid particle of size between 10nm to 10µm suspended in a fluid [4]. They are available in a broad variety of shapes, sizes and materials; these properties can be controlled during particle synthesis through an expanding library of chemical methods [5]. We choose 2µm diameter spheres, made of 3-(trimethoxysilyl)propyl methacrylate (TPM), as an ideal building block to start with, understanding that the size, shape and material can later be specialized to fit specific needs or applications.

The length scale in this case plays a crucial role, giving colloidal systems interesting properties. Relevant to this work, colloids make an ideal building block because they are small enough to diffuse significant distances due to thermal fluctuations (enabling their self-assembly into aggregates at experimentally accessible timescales), yet large enough to be studied with visible light. This makes colloidal systems both spatially and temporally accessible to study with an optical microscope.

1.1.1 Limits of a microscope

The Abbe resolution limit is typically used to estimate the resolution limit of a microscope:

$$R \sim \frac{\lambda}{2NA} \tag{1.1}$$

where λ is the wavelength of light and NA the numerical aperture of the combined objective and condenser [6]. The numerical aperture can be thought of as the angular size of the cone of light which an objective can capture; values are less than 1 in air, with high end oil immersion objectives reaching 1.6. Abbe's equation is straightforward - to increase the resolution of a microscope, there are only two options: decrease the wavelength of light, or increase the NA of the objective. For visible light ($\sim$ 400-700 nm) and NA ~ 1 we find that the minimum resolution of an optical microscope is of the order 200 nm. Thus, our micro-metric building blocks sit at the edge of what can be resolved with visible light.

1.1.2 Diffusion at the micro-scale enables colloidal aggregation

In the classical picture of Brownian motion, particles suspended in a fluid are constantly bombarded by molecules in the surrounding fluid, driven by thermal fluctuations [7, 8]; these collisions lead to incessant motion, characterized by a random walk. The mean squared displacement ($\langle \Delta r^2 \rangle$) of a diffusing particle (in d dimensions) is proportional to the amount of elapsed time: $\langle \Delta r^2 \rangle = 2dD\Delta t$. For a a spherical particle of radius R, the diffusion coefficient in equilibrium with a thermal bath is given by the Stokes-Einstein equation:

$$D = \frac{k_B T}{6\pi\eta R} \tag{1.2}$$

where η is the viscosity of the surrounding media, k_B the Boltzmann constant, and T the temperature. A 1µm sphere in water diffuses roughly 1 μm^2 per second. This thermal motion allows colloids to explore their surroundings, sporadically colliding with one another. In the presence of a sufficiently large, attractive potential, they irreversibly bind and form aggregates. The following section (Interactions, section 1.2) describes how we create a large attractive potential between colloids without inhibiting their diffusion.

Summary: micro-metric building blocks

Micro-metric colloids are large enough to resolve with an optical microscope, yet small enough to diffuse significant distances, enabling them to explore their surroundings in experimentally accessible timescales. In the presence of a large, attractive potential, diffusing colloids will irreversibly bind to form aggregates.

1.2 Interactions

The next necessary piece of the puzzle are interactions. In the experimental system, we use an attractive potential to bind the building blocks (colloids) together, such that they assemble into aggregates. Relevant to this work, we will focus on four potentials: electrostatics, Van der Waals, steric repulsion, and depletion. In the interest of brevity, most of the equations will be presented without a derivation; a more thorough discussion can be found in the appendix (Chapter 7).

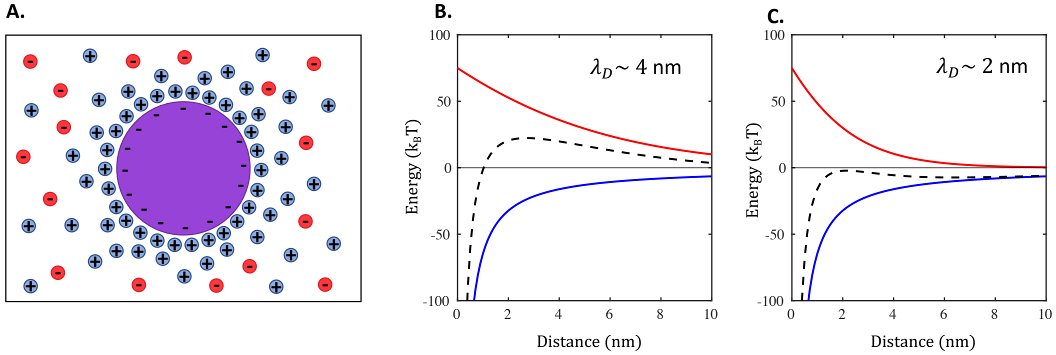

Figure 1.1. Intro to DLVO (A) Positively charged ions are attracted to the negatively charged TPM colloid. This results in a diffuse double layer of ions, which screens the electric potential from the charged colloid. **(B, C)** Plots of the repulsive electrostatic potential (red) and attractive Van der Waals potential (blue) for two colloids. The sum of the two potentials (DLVO theory) is plotted in black. As the ion concentration increases (i.e. decreasing λ_D), the repulsive barrier between colloids collapses, destabilizing the colloidal system. Equations, derivations, and parameters can be found in the supplement.

1.2.1 Electrostatics: repulsive potential

Consider the case of TPM colloids in solution with ions, confined in a glass capillary. The TPM colloids carry a negative charge in aqueous solution at neutral pH, due to de-protonation of a silonal moiety [9, 10]. Therefore, the electrostatic potential between two colloids is generally repulsive, as the colloids are both negatively charged. The glass substrate below is similarly negatively charged [11]. The negative charge attracts a diffuse double layer of positively charged ions near the surface, which effectively screens the charge of the colloid [Fig. 1.1A]. It results that the electric potential from a charged sphere & diffuse double layer combination decays exponentially with distance from the colloid surface, with a characteristic length termed the Debye length (λ_d) [12, 13, 14]; Following the Debye-Huckel approximation for monovalent ions, the Debye length is given by:

$$\lambda_D = \left[\frac{e^2 \sum_i n_i^0 z_i^2}{\varepsilon k_B T}\right]^{-1/2} \tag{1.3}$$

with ε the electric permittivity, e the elementary charge, and n_i^0 the bulk concentration of ion species i, with charge z_i. A derivation of this equation, following Chapter 7 of Robert J. Hunter *Foundations of Colloid Science*, can be found in the supplemental materials (Section SI.1.2.3 Debye-Hückel approximation). We notice that $\frac{1}{2}\sum_i n_i^0 z_i^2$ gives the ionic strength of the solution (i.e. in a solution of 10mM NaCl dissolved in water, the ionic strength is 10mM); thus the Debye length is inversely proportional to the square root of the ionic strength. A useful formula is given by [14], where c is the ionic strength in units of mM:

$$\lambda_D(\text{nm}) \sim \frac{10}{\sqrt{c}} \tag{1.4}$$

In the experimental system (c $\sim$ 32mM) , we estimate the Debye length is $\sim$ 2 nm. In order to remain bio-compatible, we have limited latitude to lower the ionic strength, as a minimal amount of buffer is required to maintain *E. coli* motility (see: Section 2.2.1 , and Section 2.1.3). Since the electrostatics act over such a short distance in the experimental system (1-5 nm), the Van der Waals potential becomes relevant.

1.2.2 Van der Waals: attractive potential

Van der Waals potentials are attractive, originating from attraction between molecular dipoles. For a pair of dipoles separated by a distance r, the potential is extremely short range

$$V_A^{dipole}(r) \sim -r^{-6} \tag{1.5}$$

For macroscopic bodies, the total potential due to Van der Waals is obtained by integrating over the volume [12]. For two spheres of radius R, the Van der Waals potential (as a function of r, the distance between them) is given by:

$$V_A^{sphere}(r) = -\frac{A_{ijk}R}{12\pi r} \tag{1.6}$$

where A_{ijk} is the Hamaker constant, a material property which describes the interaction of material i with material j in media k [12]. Typical values for the Hamaker constant in water for various materials are between 10^{-21} J and 10^{-20} J [13, 14].

1.2.3 DLVO theory : Electrostatics + Van der Waals

In the standard treatment (DLVO theory), the combined electrostatic and Van der Waals potentials are considered as a function of increasing ion concentration. As the ionic concentration increases, the repulsive electrostatics are increasingly screened while attractive Van der Waals are unaffected; eventually, the repulsive barrier from the electrostatics collapses, and colloids are able to come close enough for Van der Waals to take over [12]. A graphical representation of this can be seen in Fig. 1.1B and Fig. 1.1C, and in depth derivation of the relevant equations can be found in the appendix.

Once the repulsive potential barrier collapses, the colloidal suspension becomes unstable and begins to aggregate. This is a standard method to induce aggregation in a 3D colloidal system (see [15], for example). In our 2D experiments, this results in colloids sticking to the glass substrate, inhibiting their diffusion. As described in the previous section, diffusion is key to enabling colloidal aggregation. In the following section we introduce a polymer brush to the surface of the colloids, which stops them from getting close enough to stick to the glass.

Summary: DLVO

In the experimental system, ions screen the electrostatic repulsion to short range ($\lambda_D \sim$ 2nm), allowing the Van der Waals attractive potential to take over. This causes colloids to stick to the glass substrate, inhibiting their diffusion.

1.2.4 Steric repulsion via polymer brush

To stabilize the colloidal suspension (i.e. stop colloids from sticking to the glass substrate), we use steric repulsion via a polymer brush (Pluronic F-108, see Fig. 1.2A). Before two colloids can come into contact with one another (or, before colloids can touch the glass surface) the polymer brush must be either collapsed or displaced. In effect, this creates an additional repulsive potential barrier, on the length scale of the polymer brush. The polymer brush enables diffusion of the colloids by setting a minimum distance between the colloids and the glass.

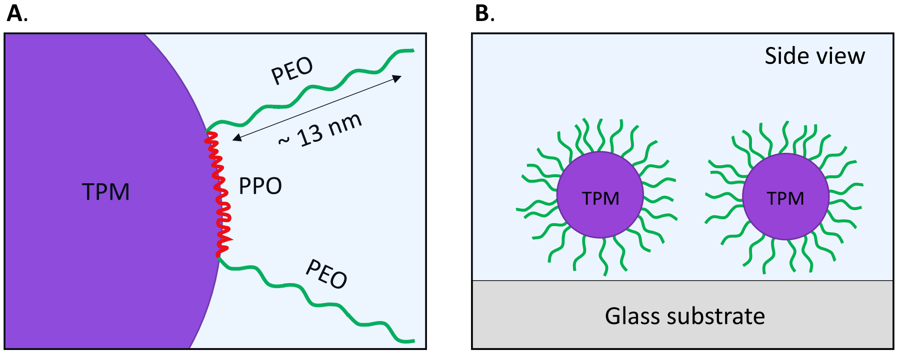

Figure 1.2. Steric stabilization via polymer brush (A) F-108 triblock polymer brush self assembled on surface of TPM colloid (purple) in water (blue). The middle section of F-108 (PPO, red), is hydrophobic, and prefers the hydrophobic TPM. The first and third section (PEO, green, ∼ 13 nm) are hydrophilic, and prefer to orient towards the water. **(B)** The polymer brush keeps the colloids from sticking to the glass via Van der Waals, allowing them to diffuse on the surface.

In practice, we add F-108, a pluronic triblock copolymer made up of three sections (PEO-PPO-PEO) in solution with the TPM colloids. The first and third sections of F-108 are PEO (each ∼ 13 nm long [16]), a hydrophilic polymer which prefers to orient towards the aqueous solution [13]. The middle section (PPO) is hydrophobic. Due to the hydrophobic nature of TPM, PPO prefers binding to the TPM surface and PEO prefers facing towards the aqueous solution [10], as depicted in Fig. 1.2A. We observe that the addition of 0.1% F-108 stops the colloids from adhering to the glass surface; the colloids behave as a 2D gas, diffusing and colliding on the glass substrate. In order to induce aggregation of the diffusing colloids, we use the depletion interaction to irreversibly bind colloids together.

Summary: Steric stabilization

We add a polymer brush to the surface of the TPM colloids which stops the short range, attractive Van der Waals potential from taking over. This enables their diffusion, by keeping the colloids from sticking to the glass substrate. But, now we need a strong attractive potential between colloids to enable aggregation.

1.2.5 Depletion interaction

We use a non-absorbing polymer (termed "depletants", 600K PEO, radius (a) $\sim$ 50nm [17]) to create an attractive potential between TPM colloids, via the depletion interaction. The depletion interaction is entropic in origin. A qualitative description begins by recognizing that, surrounding each colloid (purple circles, Fig. 1.3A), there is an excluded region (red region, Fig. 1.3A) where the center of mass of the depletants (blue circles, Fig. 1.3A) cannot enter. By forcing the colloids together, part of this excluded region overlaps; this results in more available space for the depletants [Fig. 1.3B], maximizing their entropy. The depletants vastly outnumber the colloids; thus, forcing the colloids together maximizes the entropy of the system. For a closed system in thermal equilibrium, $F = U - TS$, with F the free energy, U the internal energy, T the temperature and S the entropy. For hard spheres, $U = 0$ outside of contact. Thus, maximizing the entropy of the system (S) minimizes the free energy (F).

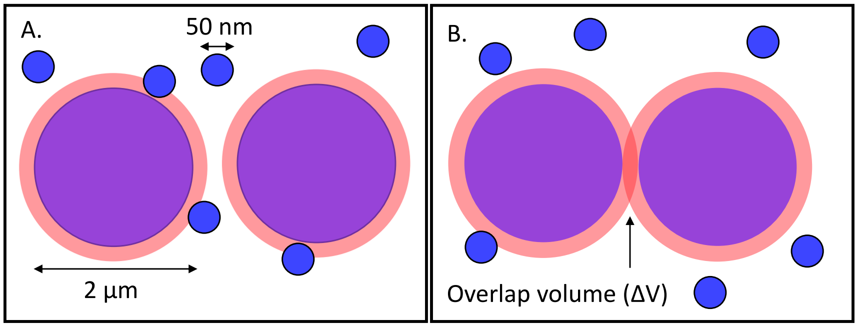

Figure 1.3. Depletion interaction (A) Colloids (purple), and depletants (blue) in solution. Surrounding each colloids is an excluded region (red), where the center of the depletant cannot enter. **(B)** Forcing the colloids together causes part of the excluded region to overlap. This maximizes the available space for the depletants. Since the depletants vastly outnumber the colloids, this maximizes the entropy of the system.

Starting with the partition function for an ideal gas, we derive the free energy from adding an available volume ΔV to the depletants. A full derivation can be found in the appendix; the relevant equation being:

$$\Delta F \sim -k_B T n_p 2\pi a^2 R \tag{1.7}$$

for n_p the number density of particles in solution, a the radius of the depletant (50nm), and R the radius of the colloid (1µm) [18]. We estimate the strength of attraction to be $\sim 75 k_B T$ at a depletant concentration of 3.25 g/L. The excluded volume begins to overlap when the colloids are separated by a distance of twice the radius of a depletant (roughly 100nm) [18, 17]; thus, the size of the depletant sets the length scale of the depletion interaction. Notably, there is no entropic cost to colloids translating on the surface of the glass, thus the colloids are still able to diffuse. Having engineered a system where colloids can both diffuse and stick together, we can now discuss the structures they form.

Summary: Depletion interaction

We harness the depletion interaction to create a strong, short range attractive potential between the colloids. The size of the depletant sets the length scale of the interaction ($\sim$ 50nm), and the concentration of depletant is linearly proportional to the strength of attraction.

1.2.6 Colloidal aggregation

The phase diagram of systems of colloidal spheres is generally classified by the interaction (i.e. length scale and strength), as well as the volume fraction of colloids. At high volume fractions, systems are categorized as either glasses or crystals, depending on the order (crystals) or disorder (glasses) of the structure [4]. Within the space of relatively low volume fraction and strong, short ranged attraction, aggregates form structures characterized by a scale invariant fractal dimension (ν), termed fractal colloidal aggregates. For the purposes of this thesis, we will focus on fractal colloidal aggregates.

The study of colloidal aggregation finds its roots in the early study of aerosols – a general term, describing aggregates of small particles suspended in air [19] (note that, by our broad definition of colloids, aerosols can be considered as a colloidal aggregate). These systems represent a broad range of scientific interests from atmospheric, environmental, industrial and medical sciences; as it would turn out, colloidal aggregates share much of the same physics as aerosols. Early work from Forrest and Witten observed that smoke-aggregates appear as thin, branched structures, with sizes varying over many orders of magnitude [20]. Surprisingly, these aggregates displayed a universal power law relationship between mass and length, describing a scale invariant fractal dimension (more on this below). The link to colloids came a few years later with the work of Weitz and Oliveria, who observed a similar scale invariant fractal structure in systems of charged gold particles, destabilized by increasing the ion concentration of the surrounding media [21] (as seen in Fig. 1.4). This has sparked nearly 5 decades of experiments, simulations, and analytical theory in the field of colloidal aggregation [22].

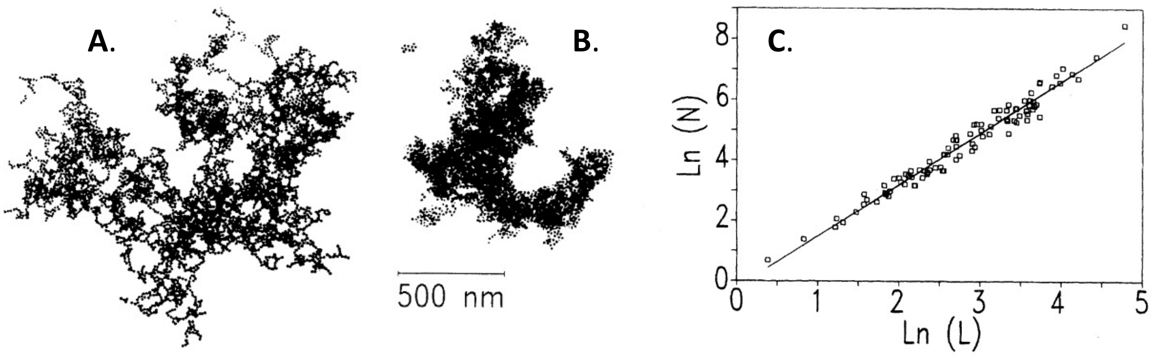

Figure 1.4. Colloidal Aggregates (A) Aggregates of gold colloids (radius 7.5nm), formed via DLCA aggregation. The structure is branched. **(B)** Aggregates of gold colloids formed via RLCA aggregation. Scale bar for both images is 500 nm. **(C)** Log-Log plot of number of colloids (N) vs length of aggregate (L) for aggregates of gold colloids formed via DLCA aggregation. The system displays a scale invariant fractal dimension. **(A) & (B)** Reprinted figure with permission from D. A. Weitz, J. S. Huang, M. Y. Lin, and J. Sung, PRL, Volume 54, Number 13, 1985. Copyright 1985 by the American Physical Society. **(C)** Reprinted figure with permission from D. A. Weitz and M. Olivera, PRL, Volume 52, Number 16, 1984. Copyright 1984 by the American Physical Society.

The characteristic length of an aggregate is typically given by the radius of gyration (R_G)

$$R_G^2 = \frac{1}{N}\sum_{i=1}^{N}(r_i - r_0)^2 \tag{1.8}$$

where r_i is the position of colloid i and r_0 the center of mass of the aggregate, containing N colloids [19]. The fractal dimension (ν) is given by the relationship between length (R_G) and mass of the aggregate (M)

$$M \sim (R_G)^{\nu} \tag{1.9}$$

At first glance, the units appear to be an issue. This relationship can be made non-dimensional by dividing the total mass (M) by the mass of a single colloid (m); henceforth, we define $\mathcal{M} = M/m$ as the number of colloids in an aggregate. A similar non-dimensional length is given by dividing R_G by the radius of a single colloid (R), such that $\mathcal{R}_G = R_G/R$ [22]. The fractal dimension is thus given by the relationship

$$\mathcal{M} \sim (\mathcal{R}_G)^{\nu} \tag{1.10}$$

Colloidal aggregation in a thermal bath can be broken into two regimes: diffusion-limited cluster aggregation (DLCA), and reaction-limited cluster aggregation (RLCA) [23]. In the former (DLCA), the attractive potential is so strong that as soon as colloids come into contact, they become irreversibly bound; therefore, the aggregation kinetics are only limited by the rate of diffusion [2]. In this regime, free colloids are immediately arrested whenever they encounter an aggregate, which makes it unlikely for them to penetrate to the center of an aggregate. The aggregates form branched, ramified networks [Fig 1.4A]. Both simulations and experiments confirm that for a 2D system, DLCA results in a fractal dimension $\nu \sim 1.4$ [24, 25].

RLCA, on the other hand, takes place under conditions where there is a small repulsive barrier between colloids before they can irreversibly bind; as a result, the kinetics are slower and determined by the the probability for a colloid to bind, hence reaction limited [2]. In this regime, free colloids are not immediately immobilized when encountering an aggregate and can explore a more possible configurations before binding; this leads to more compact, denser aggregates [Fig 1.4B]. Aggregates formed in RLCA have a larger fractal dimension ($1.4 < \nu < 2$) [24].

1.2.7 Scaling argument: Gel vs. Cluster phase

Fractal aggregates can be classified as either a gel or a cluster, depending on their size with respect to the system [Fig. 1.5]. We define a "gel" as an aggregate that contains all colloids in the system, and forms a space spanning network ($R_G \geq L$, with L the system size). This aggregate is expected to have solid-like properties, as colloids cannot freely re-arrange with respect to every other colloid in the system [2]. Similarly, we define a "cluster" as an aggregate which does not form a space spanning network ($R_G < L$); these systems are expected to have fluid-like properties, as the aggregate can freely translate [2]. A graphical representation of this can be seen in Fig. 1.5.

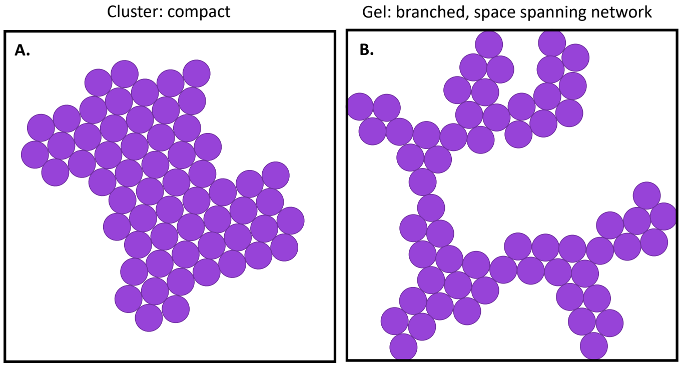

Figure 1.5. (A) Cluster phase A compact aggregate, formed of 60 colloids, which does not span the size of the system. Systems in the cluster phase exhibit fluid-like mechanical properties, as the aggregate can freely translate. **(B) Gel phase** A branched aggregate of 60 colloids, forming a space spanning network. Colloidal gels exhibit solid-like mechanical properties.

A scaling argument can be made whether the an aggregate is capable of spanning the size of the system, based on the volume fraction of colloids (ϕ) and the fractal dimensions (ν) [22, 2]. In d dimensions, the number of colloids in the system (N)is given by

$$N \sim \frac{\phi L^d}{R^d} \tag{1.11}$$

with R, the radius of a single colloid. Postulating that the system eventually aggregate such that every colloid is contained in a single aggregate (such that, $\mathcal{M} = N$), we can define the size of this aggregate using Eq. 1.10: $\mathcal{M} \sim (\mathcal{R}_G)^\nu$ (for $\mathcal{M}$ the number of colloids in the aggregate and $\mathcal{R}_G = \frac{R_G}{R}$ the radius of gyration of the aggregate normalized by the radius of a colloid).

$$N \sim \mathcal{R}_G^\nu \tag{1.12}$$

To be system spanning, the size of the aggregate must be equal the size of system. Inserting $R_G = L$, we come up with the relationship

$$\phi^* \sim \left(\frac{L}{R}\right)^{\nu - d} \tag{1.13}$$

Such that, at a given fractal dimension, there is a critical volume fraction (ϕ^*), above which the system is able to form a space spanning aggregate (i.e. colloidal gel). Taken the other way, at a given volume fraction we can define a critical fractal dimension, below which the system is able to form a space spanning aggregate (i.e. Gel phase, with solid-like mechanical properties); above this critical fractal dimension, the aggregates are too dense to span the system (i.e. Cluster phase, with fluid-like mechanical properties).

Summary: Colloidal aggregates

Taken together, we have discussed how the aggregation mechanism (DLCA vs RLCA, in a thermal bath) determines the fractal dimension of the colloidal aggregate. Furthermore, we have laid out a scaling argument describing how the fractal dimension determines the phase behavior of the system (i.e. gel or cluster). These phases are expected to have different mechanical properties, with a gel acting as a visco-elastic solid, and clusters acting as a fluid.

The aggregation mechanism is key to controlling the structural and mechanical properties of the colloidal system. My work centers around controlling these features with the activity of a bacterial bath.

1.3 *E. Coli* : an active particle of choice

Active particles are particles that convert energy into mechanical work. Motile *E. coli* present themselves as an ideal active particle in many respects, due to their abundance and the vast biological tools designed to work with them. In the following section, we describe concepts and previous work motivating our use of a bath of motile *E. coli* to inject energy into the system.

1.3.1 Swimming at the micro scale

E. coli live at low Reynolds number (RE). RE is a dimensionless quantity, representing the ratio of inertial forces to viscous drag. The Reynolds number is given by $\mathrm{RE} = \rho V L/\eta$, with V is the typical velocity, L the typical length, ρ the density and η the viscosity.

Using rough numbers for an Olympic Swimmer ($V \sim 1$ m/s, $L \sim 2$ meter) in water ($\eta \sim 10^{-3}$ Pa $\cdot$ s , $\rho = 1000$ kg/m^3) we find $\mathrm{RE} \sim 10^6$ - inertial forces are greater than viscous drag (i.e. $\mathrm{RE} > 1$). This makes sense, as we know from experience that diving headfirst into a pool, we can glide for some distance.

By contrast, for *E. coli* bacteria ($V \sim 20$ μm/s, $L \sim 1$ μm), we find $\mathrm{RE} \sim 10^{-5}$ [26]. Low RE has important consequences on the swimming dynamics. For example, momentum is irrelevant for the swimming *E. coli* – if it stops pushing, it will almost immediately stop moving ($\mathrm{RE} << 1$). At every moment, the propulsive force is balanced by viscous drag, making *E. coli* force and torque free swimmers. Additionally, at low RE, any reciprocal motion results in zero net displacement, the classic example being a clam opening and closing its shell [26].

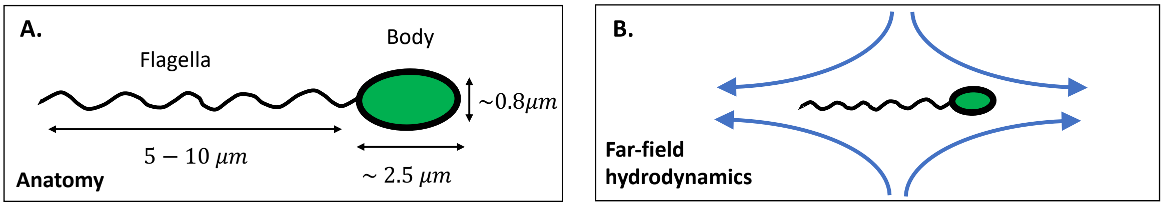

Figure 1.6. **(A)** Minimal anatomy of an *E. coli* bacteria, consisting of a body connected to a long flagella tail. Measurements from [27]. **(B)** Approximate far - field hydrodynamics of swimming *E. coli*. Fluid is pushed out the front and back, and sucked in from the sides. Experimental measurements of this reported in [28].

E. coli circumvent this constraint by spinning a long helical tail of proteins - the “flagella” - thus avoiding reciprocal motion. Measurements show the body is 2.4 µm long, .85 µm wide, and the flagella are $\sim$ 10 µm long [27][Fig. 1.6A]. Each flagella is connected to a motor (BFM, or bacterial flagellar motor), powered by exchanging protons across the cell membrane [29, 30]. When all BMF spin counter clockwise (as viewed from behind), the flagella bundles together and propels the *E. coli* forward, termed a “run” [31]. When all BMF do not spin in the same direction, the *E. coli* rotates and changes direction - termed a “tumble”. Runs last for roughly 1s, but can last longer when the cell senses a favorable chemical gradient (i.e. increasing concentration of an “attractant”, such as food) [32]. The *E. coli* can modify their run-tumble dynamics to navigate chemical gradients in their environment - a process termed chemotaxis.

E. coli are approximated as a hydrodynamic dipole, with the propulsive force and viscous drag balanced at every moment, as measured experimentally by Drescher et al. [28]. Fluid is pushed from the front and back; due to the incompressibility of the surrounding fluid, there is a net flow of fluid inwards from the sides [Fig. 1.6B]. This leads to a hydrodynamic attraction of *E. coli* to flat surfaces, as they are sucked in from the sides [33].

1.3.2 *E. coli* suspension as a “hot” bath

In 2000, Wu and Libchaber studied the diffusion of passive tracer colloids in a suspension of motile *E. coli*. Experiments were performed on a thin film at a bacteria concentration of $5 \cdot 10^{10}$ cells/mL [34]. They coined the term “hot” bacterial bath, reporting enhanced tracer diffusion at timescales $>\sim$ 1 s, akin to raising the temperature of the bath. Below 1s, they reported ballistic-like motion, with $\Delta r^2(t) \sim t^\alpha$ for $1.5 < \alpha < 2$. This seminal work has sparked a field of studies, generally interested in the interplay between active swimmers and passive tracers.

Nearly a decade later, Minõ et al., built upon the work of Wu and Libchaber, performing an experiment with passive colloids sedimented in a glass chamber, surrounded by a suspension of active swimmers [35]. They perform experiments both with self propelled rods, whose speed can be tuned with the concentration of H_2O_2, and *E. coli* bacteria whose concentration is varied between 10^9 and 10^{10} cells/mL. Further experiments, published by Minõ et al in 2013, repeat the experiment with *E. coli* whose speed can be tuned by the pH of the surrounding media [36]. In this low-concentration regime (i.e. below the onset of collective motion), the authors showed that the increased diffusivity of tracers is proportional to the "active flux" - the concentration of active swimmers (n_A) times the speed of the active swimmers (V_A) .

$$D_{eff} = D_0 + \beta n_A V_A$$

with β determining the rate of increase of the effective diffusion. This scaling for effective diffusion in a suspension of active swimmers seems to be quite general; namely, it has been reported in 3D using similar *E. coli* bacteria [37] as well in quasi-2D experiments using *C. Reinhardt* swimmers [38, 39].

1.3.3 *E. coli* suspension: more than a "hot" bath

The picture of a bacterial bath as a "hot" thermal bath is conceptually useful, but it is important to stress that it is not the end of the story. A bath of motile bacteria is intrinsically nonequilibrium: *E. coli* are constant injecting energy into the system through mechanical work. As such, the bacterial bath is more than a hot bath.

For example, motile *E. coli* can induce persistent rotation of asymmetric gears, effectively constituting a micron-sized motor [40, 41]. Recent work, built upon the ratchet design, combines a ramp which collects cells from the bottom and guides them into an elevated rotating micro chamber; each micro chamber fits a single cell, and each motor contains 15 chambers [42]. These motors are able to achieve speeds up to 20 rotations per minute. Additionally, these experiments utilize genetically modified *E. coli*, which are only motile in the presence of green light [43, 44]. This constitutes a micro-scale motor, whose rotation rate can be controlled by the intensity of green light.

Additionally, it has been show that motile bacteria induce effective attractive interactions between particles [45, 46, 47]. As evidenced by Angelani et al., tracer particles in a bacteria bath spend extended periods of time in contact, which can be interpreted as an effective attraction. This attraction is, however, intermittent, as the tracer particles do not remain in contact indefinitely. While these results hint at the possibility for a bacterial bath to drive colloidal assembly, the use of an external attractive potential is necessary to achieve large, stable aggregates. This notably inspires the present work, combining passive building blocks, an attractive potential between the building blocks, and an active bath of motile *E. coli*.

1.4 Review of conceptually similar experimental works by other groups

The proposed experiment, studying the aggregation of sticky colloids in a bath of bacteria, is novel; there are, however, some published works which share conceptual similarities to our proposed experiment. In the following section we describe two such experiments, each leveraging active matter to inject energy into a soft matter system.

Adkins et al. [48] investigate the injection of energy into a system undergoing liquid-liquid phase separation. They combine a mixture of dextran and PEG polymer – a solution which, in equilibrium, phase separates into a dextran rich phase and a PEG rich phase (similar to an oil-water mixture). Through the addition of microtubules and kinesin motors, Adkins et al. create an active fluid, where energy is injected into the system through mechanical work of kinesin motors moving the microtubules. They discover rich dynamics – at intermediate activity (i.e. concentration of kinesin motors), the additional fluctuations increase droplet mobility, speeding up the phase separation. Above a critical concentration of kinesin, the droplets continually coalesce and fragment, similar to shaking a vinaigrette salad dressing. These experiments show the promise for active matter to control the behavior of passive constituents, driving the system to unconventional phases which are non-accessible to a passive system.

Michael Solomon's group has published three experimental works studying 3D colloidal gels, formed via DLCA aggregation, imbedded with Janus particles. Janus particles are colloids coated with half a surface of platinum. In solution with H2O2, the particles swim using diffusiophoresis due to a chemical reaction between the metal and H2O2. Initial work by Szakastis et al. [49] showed that the moderate addition of active Janus particles into the colloidal gel (ratio 1:1200) increased the dynamics within the gel, promoting re-structuring and aging. Further work from Solomon's group tested the mechanical properties of these gels; both the elastic modulus [50] as well as the yield stress [51] of the active gel reduce with increased activity, resulting in a maximum reduction of 3x compared to the passive gel. Taken together, these works directly highlight the power of active matter to direct the mechanical properties of soft materials. The experiments proposed in this thesis are similar in that they leverage active matter to tune the properties of a colloidal gel. While the work from Solomon's group investigates how active matter can modify the properties of an aggregated structure, our work leverages an active bath to direct the aggregation process, resulting in novel structures.

Summary: Chapter I

Chapter I has laid the conceptual groundwork and motivation for the experiments to come. Micron sized colloids, small enough to diffuse yet large enough to study with an optical microscope, form the building blocks of the soft materials. Using the depletion interaction we create a strong, short range attractive potential between the colloids, irreversibly binding them together. Finally, a suspension of motile *E. coli* inject energy into the system through mechanical work.

Chapter 2

Control and calibration experiments

Chapter 1 of this thesis focused on building up a base of background knowledge, motivating our experimental design. Chapter 2 describes the control and calibration experiments performed while developing the experimental system. We begin by studying colloidal aggregation in a thermal bath (Section 2.1), and later characterize the active suspension of *E. coli* (Section 2.2).

2.1 Colloidal aggregation in a thermal bath

In the following section, we describe a series of experiments to calibrate the system, investigating colloidal aggregation in a thermal bath (i.e. without *E. coli*). Using the data from these experiments, we develop data processing techniques to analyze the fractal dimension and mass distribution of aggregates; these techniques will be used later to evaluate the morphology of aggregates is the active bath. This section concludes with a general materials and methods section for colloidal aggregation experiments, applicable to both this section and the following chapter.

2.1.1 Fractal dimension in thermal bath at varying concentrations of depletant

To establish a baseline for future work, we perform a series of experiments analyzing the aggregation of colloids in a thermal bath at varying concentrations of depletant. For these experiments, colloids (building blocks, 2.2 µm diameter TPM spheres), F-108 (polymer brush), and PEO (depletant, MW 600K) are combined in a glass capillary. To maintain consistency with experiments using *E. coli*, these components are suspended in Motility Medium, a minimal media designed to promote *E. coli* motility (10mM Potassium Phosphate buffer, 0.1mM EDTA, see: Section 2.2.1). The concentration of PEO is varied from 0.6 g/L to 3.25 g/L, which varies the strength of the attractive potential between colloids. A more in depth materials and methods section, describing how the experiment is set up, can be found below in Section 2.1.3.

The capillary is placed on the motorized stage of an inverted microscope and observed automatically for 8 hours, capturing one frame every minute at 5 locations along the capillary. Zoomed in images of the aggregates after 7 hours can be found in Fig. 2.1A and Fig. 2.1B. Aggregates in Fig. 2.1A are formed in 0.6g/L PEO (low binding energy), and are more compact, typical of RLCA aggregation (compare with Fig. 1.4B). Aggregates in Fig. 2.1B are formed in 3.25g/L PEO (high binding energy) and form ramified, branched structures, typical of DLCA aggregation (compare with Fig. 1.4A). We further quantify the morphology of aggregates using the fractal dimension.

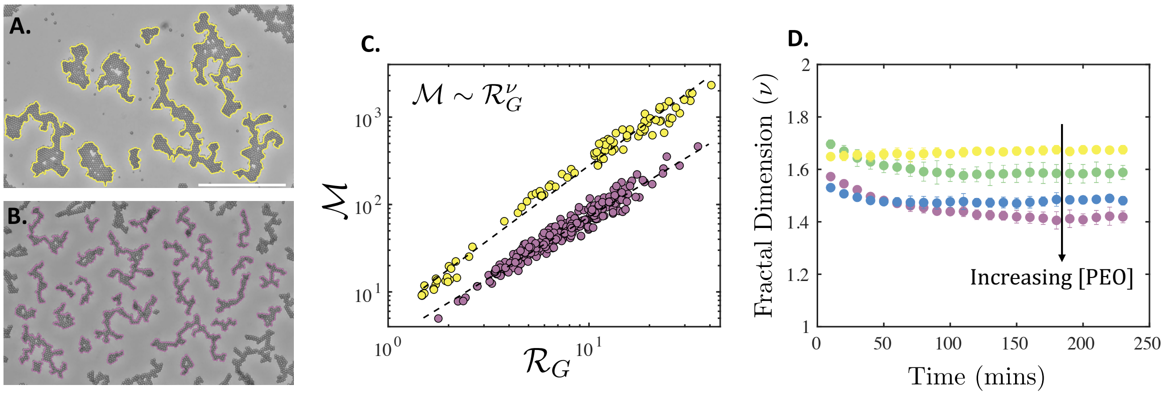

Figure 2.1. **(A)** Cropped image of colloidal aggregates in a thermal bath after 7 hours with 0.6 g/L of PEO (depletant). Aggregates are identified using image processing techniques described below, and outlined in yellow. Scale bar 100µm. Same scale for (A) and (B). **(B)** Cropped image of colloidal aggregates in a thermal bath after 7 hours with 3.25 g/L of PEO (depletant); aggregates outlined in purple. **(C)** Example of how fractal dimension is calculated, using full images from (A) (yellow) and (B) (purple). Dashed line is a fit to the data $\mathcal{M} \sim \mathcal{R}_G^{\nu}$. Yellow data points are offset vertically from purple. **(D)** Fractal dimension as a function of time, for aggregates formed in thermal baths at various concentrations of PEO (depletant). Concentrations of PEO are: 3.25 g/L (purple), 1.6g/L (blue), 0.8g/L (green) and 0.6g/L (yellow). Fractal dimension reaches a steady state after approximately one hour; the steady state fractal dimension increases with decreasing PEO concentration.

Image processing techniques: Fractal dimension

We employ image processing to quantify the morphology of colloidal aggregates. Generally, we first apply a gaussian filter to the image, with a standard deviation equal to the radius of a single colloid. Next, we binarize the image, and remove any regions touching the edge of the frame, to avoid analyzing the morphology of a partial aggregate. Finally, we remove any aggregates less than 5 colloids in size; as discussed in [24], small aggregates do not contain meaningful information regarding the fractal dimensions. After binarization, we can readily access the list of pixels contained in each binary region; this will be used to calculate a radius of gyration and area of the aggregate.

Using the list of pixels in each binary region, we calculate the radius of gyration (R_G) of each aggregate using the following formula:

$$R_g^2 = \frac{1}{n}\sum_{i=1}^{n}(x_i - x_{cm})^2 + (y_i - y_{cm})^2$$

where (x_i, y_i) specifies the location of each pixel, and (x_{cm}, y_{cm}) specifies the center of mass of the binary region.

For clarity, we repeat Eq.1.10, defining the fractal dimension (ν). As a reminder, $\mathcal{M}$ is the mass of an aggregate in units of number of colloids, $\mathcal{R}_G$ is the radius of gyration of the aggregate, normalized by the radius of a single colloid.

$$\mathcal{M} \sim (\mathcal{R}_G)^{\nu} \tag{2.1}$$

To calculate the average fractal dimension in a frame, we plot on log-log the normalized radius of gyration ($\mathcal{R}_G$) and normalized area ($\mathcal{M}$) for each aggregate; the slope gives the fractal dimension, as depicted in Fig. 2.1C.

Results and comparison to literature: Fractal dimension

We observe that, after about an hour of aggregation, the fractal dimension evolves to a steady state value [Fig. 2.1D]. Additionally, as the attractive potential between colloids is increased (i.e. increasing concentration of PEO), the steady state fractal dimension lowers to a minimum of $\nu \sim 1.4$; these findings are in line with DLCA simulations performed by Cerda et al. [24], as well as experiments performed by Griffiths et al. [25].

2.1.2 Aggregate mass distribution in thermal bath

In addition to the fractal dimension, we analyze the mass distribution of aggregates formed in the thermal bath. We investigate the mass distribution as a function of increasing PEO concentration, as well as how it evolves in time. These experiments follow the same set up as described previously; the experiment containing 3.25g/L PEO is observed for 40 hours, to analyze how the mass distribution evolves in time.

Image processing techniques: Mass distribution

Using the binary image processing techniques described previously, we calculate a empirical cumulative distribution function (or, eCDF).

$$\text{eCDF}(\mathcal{M}) = \frac{\text{number of aggregates with mass} < \mathcal{M}}{\text{total number of aggregates}}$$

In Fig. 2.2, we display $\mathcal{P}$, the complementary cumulative distribution function, equal to 1-eCDF($\mathcal{M}$). **$\mathcal{P}$ constitutes the probability of an aggregate to be of size larger than $\mathcal{M}$.**

Results and comparison to literature: Mass distribution

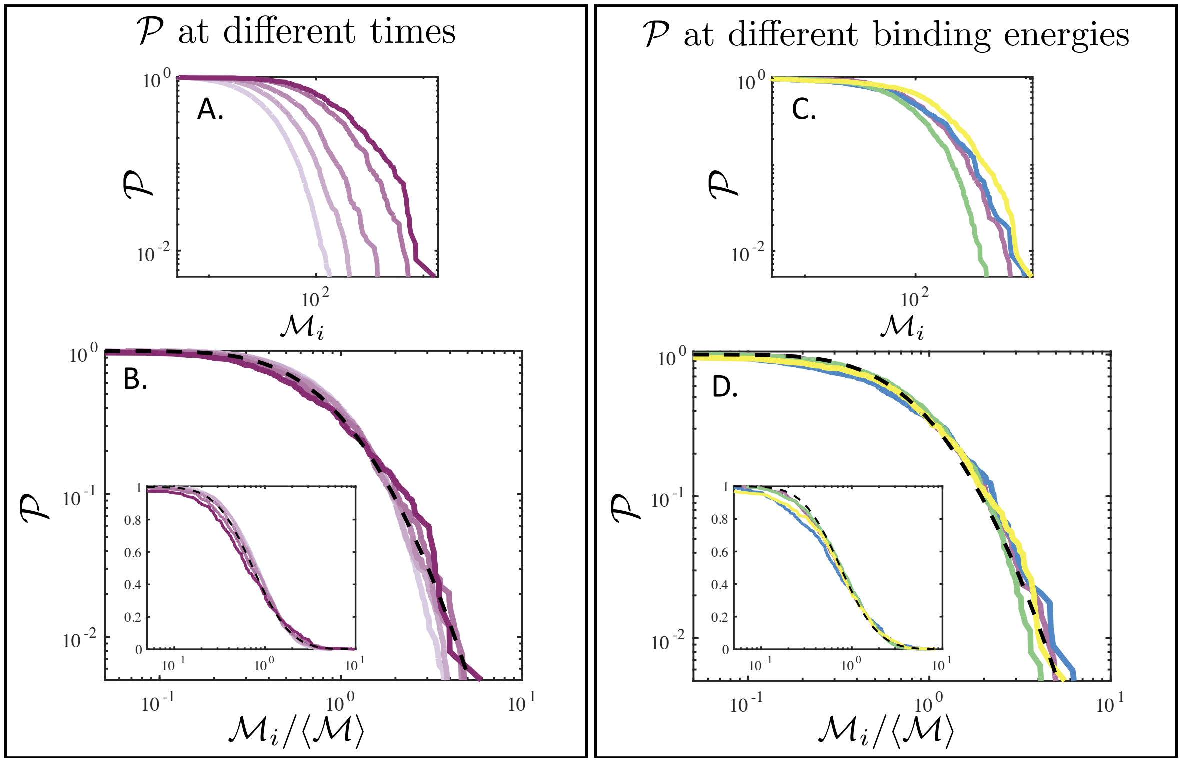

Figure 2.2. **(A) and (B)** Complementary cumulative distribution function ($\mathcal{P}$) of **(A)** aggregate mass, and **(B)** normalized aggregate mass, for the experimental conditions $\rho_B = 0$ and 3.25g/L PEO (MW 600k). Different times during the experiment are plotted on a gray to purple color palette : 2.5 hours (gray), 5 hours, 10 hours, 24 hours, and 40 hours (purple). **(C) and (D)** Complementary cumulative distribution function ($\mathcal{P}$) of **(A)** aggregate mass, and **(B)** normalized aggregate mass after 24 hours, for varying concentrations of PEO depletant (MW 600k), with $\rho_B = 0$. Concentrations of PEO are: 3.25 g/L (purple), 1.6g/L (blue), 0.8g/L (green) and 0.6g/L (yellow). In both (B) and (D) the same data is plotted on a Log-Lin scale in the inset. The black dashed line corresponds to a log-normal distribution with $\mu = 0.3$ and $\sigma = 0.75$

In Fig. 2.2A and Fig. 2.2B, we analyze the experiment with 3.25g/L PEO at various time-steps (2.5 hours, 5 hours, 10 hours, 25 hours, and 40 hours). We find that the mass distribution follows approximately a log-normal distribution [Fig. 2.2A]. Furthermore, this distribution can be made self-similar when normalized by the average aggregate mass [Fig. 2.2B]. In Fig. 2.2C and Fig. 2.2D, we extend these result to experiments at lower depletant concentrations, corresponding a concentration of PEO of 1.6g/L, 0.8 g/L, and 0.6 g/L; again, we find the mass distribution is approximately log-normal [Fig. 2.2C] and can be made self-similar when normalized by the average aggregate mass [Fig. 2.2B].

These results are in line with previous theory [52], and simulations [53] predicting that the mass distribution of aerosols aggregating via brownian coagulation (i.e. cluster-cluster merging mediated by diffusion) approaches a log normal distribution after sufficient time. Recently, this theory has been generalized to describe tissue cells, which slowly diffuse due to collisions with their surroundings, leading to aggregation via merging and fragmentation events [54]. Notably, Rulands et al., [54] find that cell lines which deviate from the identified merging-fragmenting aggregation do not exhibit the same scaling behavior. The log-normal size dependence and rescaling in Fig. 2.2 is characteristic of a universality class of systems which undergo aggregation via merging, fragmentation and diffusion [52].

2.1.3 Materials and methods for colloidal aggregation experiments

Here we document the materials and methods used for the colloidal aggregation experiments. This section applies to the experiments in the thermal bath, described previously, as well as the experiments in the active bath described in the following chapters. The general scheme is to combine colloids, depletants and *E. coli* in a sealed glass capillary, and observe it during aggregation. Images are captured automatically using a motorized stage, to enable observation over long times.

We describe the set up for 3 experiments. To investigate the short-time dynamics of aggregates, we perform experiments at low colloid concentrations (surface fraction $\sim 10\%$)

using a high frame rate and high magnification. To study the long-time dynamics, we observe aggregates over a period of four hours; these experiments use a higher colloid concentration (surface fraction $\sim$ 18%), a slower frame rate and a larger field of view (to observe large structures). Finally, we study the morphology of space spanning 2D colloidal gels formed in a high colloid concentration (surface fraction $\sim$ 38%).

The specifics of setting up these experiments are not relevant to understand the key findings of this thesis. This section has been included as a reference for future students, but can be skipped (until Section 2.2) by most readers.

Colloidal aggregation solution

Colloids (diameter 2.2 μm TPM Spheres) are diluted into solution containing Motility Medium (MM), 10mM NaCl, 0.1% F108, and 1% Glucose. The Motility Medium contains 10mM Potassium Phosphate buffer (pH 7) and 0.1mM EDTA (pH 8); thus we estimate the total ion concentration to be 32mM [25]. Unless otherwise stated, the concentration of depletant is 3.25 g/L PEO (MW 600K). *E. coli* cells are added from the high concentration sample of cells suspended in MM, described previously. To vary the strength of the active bath, we repeat the experiment with different bacteria concentrations. Bacteria concentrations are reported in fractions of the maximum concentration: $\rho^* = 6 \times 10^8$ cells/mL. The solution is confined in a 3mm x 0.3mm x 50mm rectangular glass capillary, utilizing capillarity, placed on a glass slide and sealed with a wax pen.

Short-time dynamics: experiment set up

First, we design experiments to measure the diffusion of aggregates over minutes. For these experiments, the concentration of colloids is chosen such that the surface area fraction is 10% ± 2%, once the colloids have sedimented onto the bottom surface of the glass capillary. We repeat the experiments at four *E. coli* concentrations: $\rho_B = \rho^*, \rho_B = 0.5\rho^*, \rho_B = 0.1\rho^*,$ and $\rho_B = 0$. The aggregates are observed using a 40x Nikon objective (NA = 0.6) for approximately 1 hour.

During this time, we capture a series of 3000 frame videos at 20fps along the capillary.

Long-time dynamics: experiment set up

Next, we aim to measure the long-time dynamics and morphology of colloidal aggregates, over a period of 4 hour. For these experiments, the concentration of colloids is chosen such that, once the colloids have sedimented the surface area fraction is $18\% \pm 3\%$. We repeat the experiments at 6 *E. coli* concentrations: $\rho_B = \rho^*, \rho_B = 0.5\rho^*, \rho_B = 0.2\rho^*, \rho_B = 0.1\rho^*, \rho_B = 0.05\rho^*$ and $\rho_B = 0$. The aggregates are observed using a 20x Nikon objective (Na = 0.45) for 4 hours; we capture one frame per minute time-lapses at 5 locations along the capillary.

Colloidal gel: experiment set-up

We investigate 2D colloidal gels assembled in the active bath, at surface area fraction $38\% \pm 2\%$. We repeat the experiments at 3 *E. coli* concentrations: $\rho_B = 0.1\rho^*, \rho_B = 0.05\rho^*$ and $\rho_B = 0$. The aggregates are observed using a 10x Nikon objective (NA = 0.3); we capture one frame per minute time-lapses at 5 locations along the capillary. Gels in the active bath are observed for 20 hours, but typically percolate before 4 hours. Aggregates in the thermal bath are observed for 120 hours.

Microscopy for colloidal aggregation experiments

All data for the colloidal aggregation experiments is taken on a Nikon TI Eclipse microscope equipped a motorized stage, controlled using Micro-Manager software. The microscope is equipped with two cameras. A Hamamatsu Orca Flash 4.0 CMOS, utilizing a 2048 x 2048 pixel Field of View (FOV) and 16bits, is used for taking time-lapses with a frame rate of 1 frame per minute (Long-time dynamics and Colloidal gel experiments). For videos requiring a faster frame-rate, we utilize an Edmunds Optics USB 3.0 CMOS camera, with a 480 x 752 pixel FOV and 8bits (Short-time dynamics).

Stock Solutions

In all stock solutions, chemicals are dissolved in 18 M-Ohm DI water from a Milli-Q EQ 7000 water purification system. A stock solution of 200mM NaCl (Sigma-Aldrich, MW 58.4) is prepared by dissolving .12g NaCl in 10mL of DI water. A stock solution of 2% w/v F108 (Sigma-Aldrich Synperonic F108 surfactant, MW 14600) is prepared by dissolving 0.2g of F108 in 10mL of DI water. Stock solution of 25 g/L PEO (Sigma-Aldrich, Poly(ethylene oxide), MW 600k) is prepared by dissolving 0.25g PEO in 10mL DI water, and stirred overnight using a magnetic stirring rod until dissolved. A stock solution of 0.1M Potassium Phosphate Buffer, used to prepare the Motility Medium, is prepared by dissolving 9.34g K_2HPO_4 (Sigma-Aldrich, MW 174.2) and 6.31g KH_2PO_4 (Sigma-Aldrich, MW 136.1) in 1L DI water. 0.5M EDTA stock solution is prepared by dissolving 186.1g EDTA dihydrate (Sigma-Aldrich, MW 372.2) into 1L DI water. The pH is adjusted to 8 using NaOH pellets, to dissolve the EDTA.

2.2 Characterizing the active suspension of *E. coli* bacteria

Section 1.3 lays out the conceptual motivation behind using a suspension of *E. coli* bacteria to inject energy into a soft material. In the following section, we tackle some of the practical aspects of working with the active suspension. We begin by quantifying the speed of the bacteria using the differential dynamic microscopy (DDM) technique. These experiments show that the *E. coli* speed decays over ∼60 minutes in the sealed glass capillary, and the addition of 1% w/v Glucose is required to maintain a constant speed in anaerobic conditions over 4 hours [Fig. 2.3]. Next, we investigate the trajectories of motile *E. coli* near the surface of the glass capillary using green fluorescent protein labeled cells, finding that they swim in circular trajectories of radius ∼ 50μm [Fig. 2.5B]. Finally, we perform a series of cell counting experiments to determine the concentration of cells in the active suspension.

2.2.1 Quantifying the speed of *E. coli*

Here we summarize the experiments to quantify the speed of the *E. coli*. We begin by reviewing the environmental conditions required for *E. coli* motility. Then, we perform experiments measuring the average speed over time of a suspension of *E. coli* in various environmental conditions relevant to the colloidal aggregation experiments described in the previous section. The final section describes the differential dynamic microscopy technique used to measure the speed of the *E. coli*.

Literature review: The effect of environmental conditions on the motility of *E. coli*

The seminal work of J. Adler and Bonnie Templeton lays the groundwork for understanding the environmental conditions required for *E. coli* motility [55]. Three important environmental conditions should be noted from this paper. First, Adler et al. describe that the addition of a chelating agent such as EDTA at μM concentrations induces motility in E. coli, even without the addition of a food source; it is hypothesized that heavy metals, even in trace amounts, suppress motility. Next, Adler et al. report the effect each of 20 amino acids, as well as Glucose; Only Glucose and L-serine are identified as giving rise to motility in both aerobic and anerobic conditions. Finally, Adler et al. report that motility is dependent on the pH of the surrounding media, with *E. coli* only motile within a range of $6 < \text{pH} < 8$. Subsequent work has shown that the speed of E. coli can be tuned via changing the pH in the presence of Potassium Acetate, but requires a more sophisticated growth procedure [56]. As a direct result of work of J. Adler and Bonnie Templeton, most modern experiments using E. coli as an active particle [34, 40, 41, 35, 43, 37, 27, 57, 58, 59, 45] suspend their *E. coli* in a media containing EDTA, buffer near pH 7, and an optional attractant.

Growth & re-suspension in motility media

E. coli (strain MG1655) are grown overnight until saturation at 33C, shaken at 200 RPM, in Tryptone Broth containing 10g/L Tryptone, and 5g/L NaCl. The saturated culture is diluted 1:100 into fresh Tryptone Broth and grown at 33C until optical density = 0.5, corresponding to mid-exponential growth phase. 1mL of cells are centrifuged at 2200 rpm for 10 min until a pellet forms.

Following the results of [55], the supernatant is removed and the cells are gently re-suspended in Motility Medium (MM), containing 10mM Potassium Phosphate buffer (pH 7) and 0.1mM EDTA (pH 8). This process is repeated twice more, to ensure the growth media is sufficiently diluted. In the final step, the cells are re-suspended in 10% of the volume of the supernatant, to create a highly concentrated sample of cells.

Experiments: environmental conditions for *E. coli* motility in colloidal aggregation solution

The goal of these experiments is to engineer the environmental conditions such that the active bath gives a constant injection of energy into the system during the 4 hour colloidal aggregation experiment. Based on the findings of Miño et al. [35] (i.e. effective diffusion is proportional to number of swimmers times their speed, see Section 1.3.2), we require a constant speed and constant motile fraction of *E. coli*. In each experiment, *E. coli* cells are suspended in MM at a concentration of 6×10^8 cells/mL. 10mM NaCl and 0.1% F-108 and are added, in agreement with solution used for Colloidal Aggregation; the solution is sealed a glass capillary.

We find that this solution is not sufficient to maintain constant motility, as the average *E. coli* speed decays over $\sim$ 60 minutes [Fig. 2.3A, red line]. We then add 1% w/v Glucose and observe that *E. coli* maintain a constant speed of 16μm/s ± 1μm/s and constant fraction alive for at least 4 hours in these conditions [Fig. 2.3A and Fig. 2.3B, green line]. Finally, we add both 1% w/v Glucose and 3.25g/L PEO, identical to the conditions in the colloidal aggregation experiment; we observe an increase in the average *E. coli* swim speed to 23μm/s ± 2μm/s, while the speed and fraction alive remain relatively constant over the four hours [Fig. 2.3A and Fig. 2.3B, blue line]. An increase in speed is consistent with previous literature regarding the effect of polymers on *E. coli* motility [60].

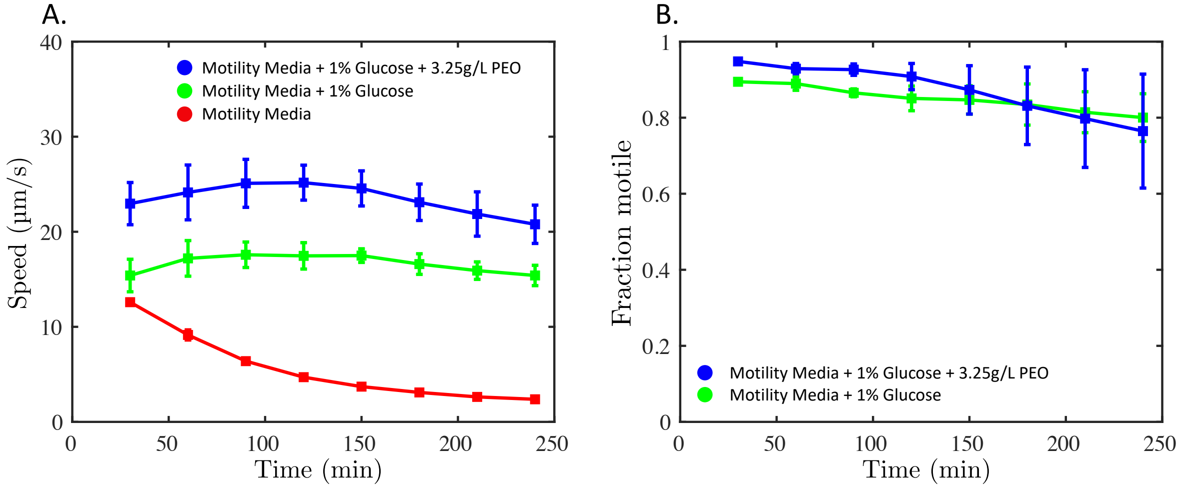

Figure 2.3. **(A)** *E. coli* swim speed as a function of time, analyzed using the DDM technique. *E. coli* motility is analyzed in three environmental conditions: Motility Medium (Red), Motility Medium and 1% w/v Glucose (Green), or Motility Medium, 1% w/v Glucose, and 3.25g/L PEO (Blue). **(B)** Fraction of motile *E. coli* as a function of time, analyzed using the DDM technique. The *E. coli* are suspended in Motility Medium and 1% w/v Glucose (Green), or Motility Medium, 1% w/v Glucose, and 3.25g/L PEO (Blue).

DDM technique to measure dynamics of the active suspension

We use differential dynamic microscopy (DDM) to characterize the dynamics of our active suspension of *E. coli* [Fig. 2.3]. DDM is a high throughput method which relies on taking the difference in intensity between pairs of images, and extracting information about the dynamics from the intensity auto-correlation function [61]. It was originally developed by Cerbino et al. [61], to analyze the dynamics of colloids undergoing Brownian motion, but has been expanded to characterize an active suspensions of *E. coli* bacteria [62, 63]. This technique provides many advantages over single cell tracking techniques, as each particle does not need to be individually resolved.

During the experiments displayed in Fig. 2.3, we capture 3000 frames at 20fps using a 10x Nikon objective (NA = 0.3) in the focal plane of the bottom of the glass capillary, using phase contrast microscopy. Videos are captured automatically every 30 minutes, for 4 hours. We calculate a radially averaged intensity auto-correlation function from the difference in intensity between pairs of images. The dynamics of the physical system are extracted by fitting the intensity auto-correlation function (calculated from the data) to the density auto-correlation function for self propelled swimmers, as described in [62, 63]. The average velocity and fraction of *E. coli* moving ballistically are reported in Fig. S2A and Fig. S2B, respectively. Error bars represent the standard deviation in average velocity (or, fraction of motile *E. coli*) over 6 realizations of the experiment.

Summary: Quantifying the speed of *E. coli*

We add 1% Glucose to the colloidal aggregation solution (developed in section 2.1), such the active suspension of *E. coli* maintain a constant speed and fraction motile for 4 hours. The dynamics of the active suspension are quantified using the DDM technique.

2.2.2 *E. coli* swimming near a flat surface

Having characterized the average dynamics of the active suspension, we now focus in on the swimming trajectories of single *E. coli*. The motion of *E. coli* near a flat surface is of particular importance to this thesis, as the experiment is quasi-2D, taking place in the bottom plane of a glass capillary. We being by reviewing the literature, and then perform experiments using green fluorescent protein labeled *E. coli*, to investigate their motion.

Literature review: Swimming in circles

As described by Lauga et al. [58], *E. coli* swim in clockwise, circular trajectories when swimming near a solid surface. The qualitative description of this begins by recalling that, whenever the *E. coli* swims forward (during a "run"), all flagella spin counter clockwise. The spinning flagella induces an opposite, clockwise rotation of the body [Fig. 2.4A]. At the interface between the fluid and the solid surface (glass substrate) is a no-slip boundary condition: the fluid must have zero speed relative to the boundary. The no-slip boundary condition results in viscous forces on the spinning body and the flagella, similar to friction acting on a ball as it rolls across a table. The viscous forces acting on the body and flagella act laterally, in opposite directions [Fig. 2.4B], causing the *E. coli* to swim in clockwise, circular trajectories [58]. The direction of rotation can be reversed by replacing the no-slip boundary with a near perfect-slip boundary (i.e. performing the experiment on a pendant drop, thus a fluid-air interface) [57].

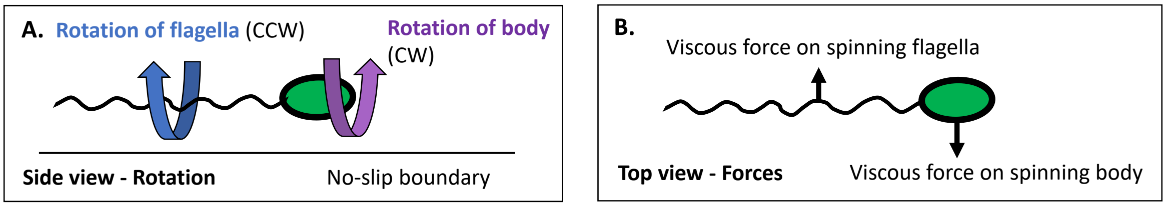

Figure 2.4. (A) Counter-clockwise rotation of flagella induces an opposite rotation of the head while swimming. **(B)** Due to the no-slip boundary condition at the solid surface, rotation of the flagella and head result in viscous forces on the swimming *E. coli*, acting perpendicular to swimming direction. It results that *E. coli* swim in circles near a solid surface. Adapted from [58].

Additionally, the radius of the circular trajectories is dependent on the distance between the *E. coli* and the interface [58]. It has been shown that the radius can be decreased by increasing the salt concentration of the surrounding media [64]. This effect can be explained using our previous knowledge of DLVO theory: the *E. coli* carry a negative zeta potential on the order of -30mV at pH 7 [65], and are thus repelled from the glass substrate due to electrostatics; increasing the ionic concentration screens the electrostatics, causing the *E. coli* to swim closer to the wall. In the following section, we quantify the radius of the circular trajectories made by *E. coli* in our experimental system.

Fluorescence microscopy of GFP labeled *E. coli*

We use green fluorescent protein (GFP) labeled *E. coli* to further investigate the dynamics of motile *E. coli*. For all experiments in Fig. 2.5, *E. coli* are suspended in Motility Medium (MM), 3.25g/L PEO, 10mM NaCl, 0.1% F108, and 1% Glucose (the standard colloidal aggregation solution, without colloids).

Fig.2.5A shows a 3 second exposure of *E. coli* swimming above the surface of the glass capillary. The *E. coli* swim in curved trajectories. We fit each arc to a circle [red line, Fig.2.5A], and extract a radius of curvature for each trajectory; the distribution of radii of curvature in Fig.2.5B is obtained by fitting the trajectories in 100 images. We find a median radius of 43 µm.

Fig.2.5D shows the distribution of *E. coli* as a function of the distance from the bottom of the glass capillary. We observe a high probability for *E. coli* to be located in the bottom $\sim$ 5µm of the glass capillary, as well as a peak in probability in the top $\sim$ 5µm [Fig. 2.5]. These results are reminiscent of the work by Berke et al. [33], finding that the *E. coli* are hydrodynamically attracted to flat surfaces [Fig.1.6B].

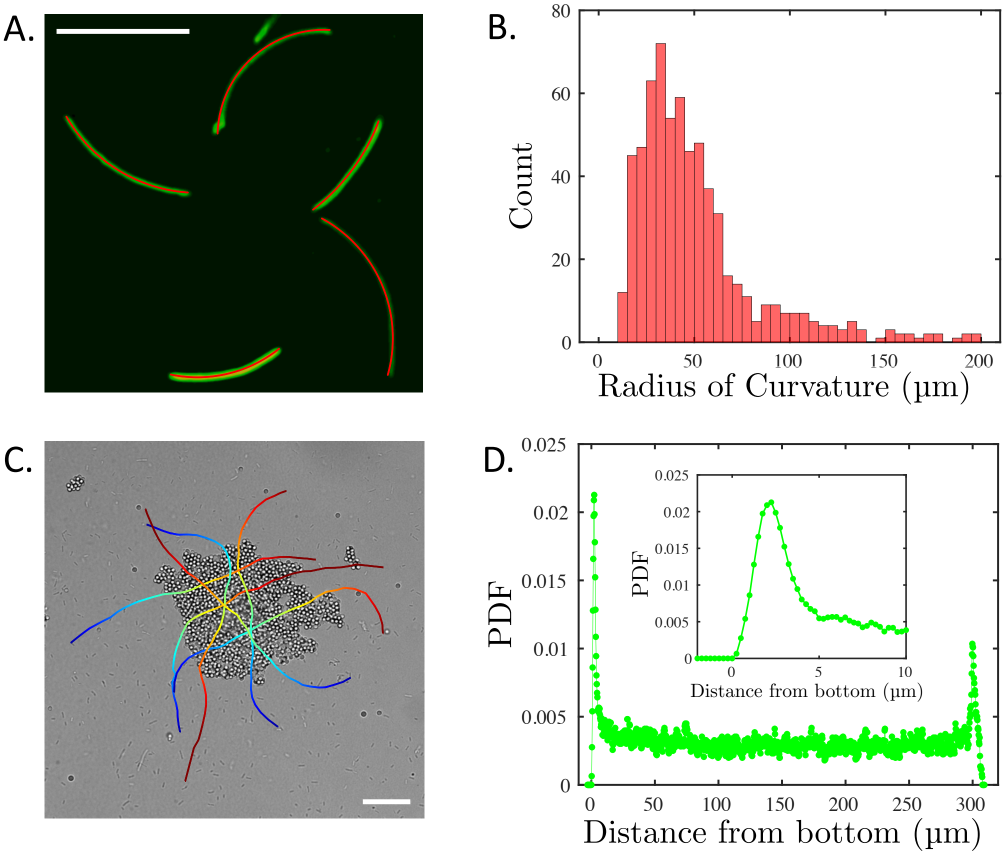

Figure 2.5. **(A)** 3s exposure images of GFP *E. coli* swimming near the bottom plane of the the glass capillary. Trajectories are fit to a circle (red line). Scale bar 50 µm. **(B)** Distribution of radius of curvature of *E. coli* trajectories; median radius is 43 µm **(C)** *E. coli* trajectories swimming through a colloidal aggregate. Trajectories are captured using confocal microscopy and overlaid on a bright-field image of the aggregate. Within each trajectory, color indicates time, with blue the initial position. Scale bar 50 µm **(D)** Probability density function of *E. coli* as a function of distance from the bottom of the glass capillary. Inset shows the same data in the region near the bottom.

Finally, in Fig.2.5C, we add colloids to the active suspension of *E. coli*. Fig.2.5C displays trajectories of GFP labeled *E. coli* as they interact with an aggregate; time is indicated by the color of the trajectory, with blue the initial position of the *E. coli* and red the final position. We observe that the *E. coli* swim through the aggregates, and while inside they swim in approximately straight trajectories. These results are reminiscent of [66], who find that *E. coli* trajectories are rectified from circular to straight as they navigate through a crystal of large, spherical colloids.

Methods: Fluorescent microscopy

GFP labeled *E. coli* are made in house by transforming the MG-1655 strain with a DNA plasmid containing both the GFP gene and an ampicillin-resistance gene, using a standard electroporation protocol.

Figs. 2.5A-B are obtained using episcopic fluorescence microscopy on a Nikon Ti2E inverted microscope equipped with a CoolLed pE-300 light source (460nm), and a GFP-4050B filter cube. All images are captured using a Teledyne Photometrics BSI sCMOS camera with a 2048 x 2048 pixel field of view. By adding an ND filter, we are able to achieve a dark backfield, as seen in Fig. 2.5A. In Fig. 2.5A, we image the motile bacteria at the bottom surface of the capillary using a Nikon 40x water immersion objective (NA 1.15), ND filter, and 3 second exposure. *E. coli* show circular clockwise trajectories. The distribution of *radii* of curvature are obtained by fitting each trajectory to a circle, using 100 images [Fig. 2.5B]. We find a median radius of 43 µm.

Confocal microscopy is used to obtain the data in Figs. 2.5C and 2.5D. Confocality is achieved on the same Nikon Ti2E microscope, through the addition of a Yokogawa CSU-W1 spinning disk with 25 µm pinhole; the sample is excited using an Omicron LightHUB Ultra laser system at 488nm. Fig. 2.5C is constructed through a combination of bright-field microscopy and confocal microscopy. First, a bright-field image of the aggregate is captured using a 20x water immersion objective (NA 0.95). Immediately after, we switch to confocal microscopy and capture a 30s video at 5fps using the same objective and field of view, focused in the bottom plane of the glass capillary. *E. coli* trajectories are tracked using the confocal data, where only the fluorescent *E. coli* are visible; trajectories are overlaid on the bright-field image to create Fig. 2.5C. Tracking is performed semi-manually; the user assigns an approximate position of the center of the bacteria in each frame, and image analysis software determines an exact location by finding the center of the nearest bright region. We see that the trajectories are approximately straight as they move through the aggregate, and return to curved trajectories before and after exiting the aggregate.

Finally, we use confocal microscopy to create a probability distribution of *E. coli* as a function of height from the bottom surface. Z-stack images are taken every 0.25 µm, starting below capillary and extending above using a 20x water immersion objective (NA 0.95). The data in Fig. 2.5D is averaged over 3 z-stacks. We observe a high probability for *E. coli* to be located in the bottom $\sim$ 5µm of the glass capillary.

2.2.3 Cell counting

Optical Density is used to quantify the concentration of cells in a sample. This measurement is made by shining light through a cuvette of known size containing a suspension of cells. The optical density is obtained from the ratio of the light intensity output and the light intensity input, and related to the density of cells in the suspension through the below equation:

$$OD = \log_{10}(\frac{I}{I_0}) = \varepsilon * l * \rho$$

Where ρ is the density of cells in suspension, l is the path length of the light and ε a constant which must be calibrated experimentally using cell counting experiments.

We conducted cell counting experiments by diluting a sample of *E. coli* at a known Optical Density one part per million into Phosphate Buffered Saline Solution (PBS); 100uL of the diluted sample is then spread on an LB agar plate and left overnight at 33C. The following morning, individual colonies, originating from a single cell, are counted by eye. These experiments are repeated three times for each bacteria concentration. The results of these experiments are summarized in Fig. 2.6; based on the data, we measure $OD1 = 7 \times 10^8$ cells/mL.

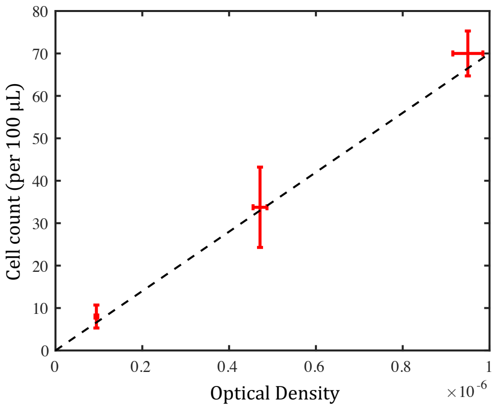

Figure 2.6. Results of the cell counting experiments, used to quantify the number of cells at a specific optical density. Data is binned, and the averages and standard deviations of those bins are displayed in red. The black line is an approximate fit to the data; we determine that $OD(1) = 7 \cdot 10^8$ cells/mL.

Summary: Chapter 2

In Chapter 2, we have laid the groundwork for the following experiments. Section 2.1 began by studying colloidal aggregation in a thermal bath, calibrating our experimental system against the literature. We have designed an experimental system with automatic, high-throughput image acquisition, allowing us to observe aggregates over many hours. Analyzing these experiments, we developed image processing techniques to quantify the fractal dimension and mass distribution of aggregates. Section 2.2, focuses on the active suspension of motile *E. coli*. Using the DDM technique, we quantified the speed and fraction of motile *E. coli* in the active suspension. We found that adding 1% Glucose results in a constant speed and motile fraction for 4 hours, amounting to a constant injection of energy into the system for the duration of the colloidal aggregation experiment. Additional experiments using GFP labeled *E. coli* were performed, identifying that they swim in circles of radius $\sim$ 50μm, and are able to navigate through colloidal aggregates. Finally, we used a series of cell counting experiments to quantify the number of *E. coli* in the suspension. The following chapter merges Section 2.1 and 2.2, investigating colloidal aggregation in a bacterial bath.

Chapter 2, in part, contains material as it may appear in Nature Physics, 2023. Daniel Grober, Ivan Palaia, Mehmet Can Ucar, Edouard Hannezo, Anđela Šarić, Jérémie Palacci. The dissertation author was the primary investigator and author of this paper.

Chapter 3

Unconventional colloidal aggregation in chiral bacterial baths

The following chapter is a verbatim reprint of the paper “Unconventional colloidal aggregation in chiral bacterial baths”, Daniel Grober, Ivan Palaia, Mehmet Can Ucar, Edouard Hannezo, Anđela Šarić, Jérémie Palacci, in press Nature Physics 2023.

Unconventional colloidal aggregation in chiral bacterial baths

Daniel Grober, Ivan Palaia, Mehmet Can Ucar, Edouard Hannezo, Anđela Šarić, Jérémie Palacci

Abstract

In equilibrium, thermal forces agitate molecules that diffuse, collide, and bind to form materials. However, the space of accessible structures in which micron-scale particles can be organized by thermal forces is limited, owing to slow dynamics and metastable states. Active agents present in a passive fluid generate forces and flows: a bath with active fluctuations. An unanswered question is whether those active agents can drive the assembly of passive components into unconventional states, and which material properties they will exhibit. Here, we show that passive, sticky beads immersed in a bath of swimming *E. coli* bacteria aggregate into unconventional clusters and gels that are controlled by the activity of the bath. We observe a slow but persistent rotation of the aggregates that originates in the chirality of the *E. coli* flagella and directs aggregation into structures that are not accessible thermally. We elucidate the aggregation mechanism with a numerical model of spinning, sticky beads and reproduce quantitatively the experimental results. We show that internal activity controls the phase diagram and the structure of the aggregates. Taken together, our results highlight the promising role of active baths in designing structural and mechanical properties of materials into unconventional phases.

In the classical picture of Brownian motion, the incessant motion of microscopic particles results from collisions with the fluid molecules. The particles and solvent are passive, driven by thermal fluctuations [8, 7]. Agitated molecules diffuse, interact and collide, building materials. This view on assembly constituted an elemental inspiration for colloidal science, aiming to translate the versatility of chemistry to the microscale.

It led to the design of a broad library of building blocks (1-10 µm in size) with various shapes and chemical properties to mimic the chemical bonds [5]. A major obstacle remains, that thermal energy is not sufficient to allow micrometric particles to explore the conformational space efficiently, making assembly challenging and often elusive. In living systems, assembly is assisted by molecular motors that generate active fluctuations [67, 68] and enhance intracellular transport [69, 70]. Active agents present in a solvent generate forces and flows, adding active noise to thermal fluctuations. They constitute an effective medium, *an active bath*, that can, in principle, overcome kinetic barriers and control the (non-equilibrium) assembly of passive building blocks. Libchaber coined the term *bacterial bath* to describe the effect of swimming *E. coli* on the positional fluctuations of micron-scale tracers [34], later extended to suspensions of self-propelled particles: nanorods or bacteria at different concentration and speed [35]. Active baths can be defined with an effective temperature as hot thermal systems under certain conditions [71] but remain intrinsically non-equilibrium, featuring properties prohibited by thermal physics. Active baths produce work[72], power asymmetric gears [40, 41] and modulate effective interparticle interactions [45, 47]. Yet, the use of active baths to control assembly is largely unexplored.

Here, we investigate the aggregation of sticky colloids in an active bath of swimming *E. coli* bacteria. We show that the bacterial bath presents features of a hot thermal bath, effectively enhancing the dynamics of assembly. We further report that the aggregates exhibit a slow and persistent clockwise rotation, which makes the bacterial bath effectively chiral, and controls the morphology and phase diagram of aggregation. Our results are quantitatively reproduced by a minimal numerical model of attractive spinners, demonstrating the importance of the non-equilibrium rotation and folding in the reshaping of aggregates and the structuring of gels. We further highlight how the mechanical properties of such materials, assembled in active baths, differ from conventional, thermal ones.

The experiment consists of colloidal beads (2.2 µm TPM spheres) immersed in a suspension of swimming *E. coli* bacteria. Short-range attraction between the beads is obtained using conventional depletion interaction with non-absorbing polymer as depletant (PEO, 600K). We perform our experiments with an attraction strength $\sim 75\mathrm{k_B T}$, that effectively leads to irreversible binding of the colloidal beads after collisions, dubbed sticky colloids. The solution of sticky colloids, *i.e.* colloidal beads and depletants ([PEO]= 3.25g/L), is added to either pure motility medium (the thermal bath) or swimming *E. coli* bacteria suspended in motility medium, at concentration ρ_B (the active bath) and sealed in a glass capillary [SI]. In order to keep the activity of the bath constant in anaerobic conditions, we add 1% w/v glucose to the suspension, enabling constant *E. coli* swimming velocity, $V = 23$ µm/s ± 2 µm/s through the duration (4h) of an experiment [Fig. 2.3] [61, 62]. The concentration ρ_B of *E. coli* bacteria of the bath is controlled via optical density and adjusted by centrifugation and resuspension for each experiment [Fig. 2.6]. We consider active baths of varying bacterial concentrations ρ_B, where the maximal value $\rho^* = 6 \cdot 10^8$ cells/mL is an order of magnitude below the onset of bacterial turbulence [73].

The glass capillary containing the sticky beads is laid on the programmable stage of an optical microscope and observed [Fig. 3.1A]. Particles sediment to form a near 2D system, at constant surface fraction $\Phi_S \sim 18 \pm 3\%$. Colloidal beads in the passive bath are agitated thermally. They collide and bind, forming ramified aggregates resemblant to those obtained in Diffusion Limited Colloidal Aggregation (DLCA, [4]). The system reaches a near steady state in experiments as large clusters diffuse too slowly to further grow. Similar experiments performed in the active bath of swimming *E. coli* bacteria reveal an entirely different dynamical state. Aggregates appear more agitated and grow faster than in the thermal experiments. They are also visually distinct: more compact than the ramified aggregates of the thermal experiment and presenting cavities [Fig. 3.1B, Movie S1].

We first compare the dynamics of the aggregates in the thermal and active bath by tracking the aggregates. Collisions between aggregates are notably identified by abrupt changes in area and perimeter, and lead to novel aggregates. In addition to the translational dynamics of the center of mass, we take advantage of the anisotropy of the aggregates to track orientation and quantify angular dynamics [SI].

The complex and evolving shapes of the aggregates require a coarse-grained approach to perform meaningful comparisons. To this end, we characterize the size of the aggregates by their radius of gyration R_G, as conventionally performed for fluctuating polymers [SI]. Dynamics are averaged in time and isotropically in space over long trajectories (> 1min); this allows us to characterize the dynamics of aggregates, in both translation and rotation, by their size R_G and the concentration of the bacteria suspension ρ_B [Fig. 3.2].

In both thermal and active baths, the Mean Squared Displacement of the aggregates is linear at short times ($\Delta t < 5$s), $\Delta R^2(\Delta t) = 4D_{\text{eff}}\Delta t$, indicative of diffusive motion with effective diffusivity D_{eff} [Fig. 3.2A-inset]. The diffusivity in the thermal bath is lower than the Stokes-Einstein prediction for bulk diffusivity in water, a result of the increased viscosity of the motility medium with suspended depletant polymers [74] and the added hydrodynamic dissipation from the proximal glass substrate of the capillary [75]. We further observe that D_{eff} increases with bacterial concentration ρ_B, up to 8-fold larger than in the thermal bath. At fixed bacterial concentration ρ_B, the diffusivity decreases with R_G, following the Stokes-Einstein scaling for a thermal system $D_{\text{eff}} = \alpha(\rho_B)/R_G$ [Fig. 3.2A]. Though non-monotonic behavior of the diffusivity of spheres in bacterial suspension has been previously reported [76], it was studied over a narrow range of sizes and remains compatible with our experimental results for aggregates of complex shapes and varying sizes. Next, we turn to the orientational dynamics of aggregates and report that the dynamics of the orientation θ is similarly diffusive at short times, with $\Delta\theta^2(\Delta t) = 2D^{\theta}_{\text{eff}}\Delta t$, and D^{θ}_{eff} the angular diffusivity [Fig. 3.2B-inset]. As for translational diffusion, D^{θ}_{eff} increases with increasing bacterial concentration ρ_B and follows the Stokes-Einstein scaling: $D^{\theta}_{\text{eff}} = \beta(\rho_B)/R_G^3$ [Fig. 3.2B].

In order to compare the amplitude of the fluctuations that lead to translational and rotational diffusion in the active bath, we normalize the measured diffusivities by the value in the thermal bath and report $\alpha(\rho_B)/\alpha_0$ and $\beta(\rho_B)/\beta_0$, where the subscript 0 refers to the thermal system [Fig. 3.2C]. Two comments are in order: (i) normalized fluctuations α/α_0 and β/β_0 collapse, highlighting the fluctuations of the active bath as common origin of the observed translational and rotational diffusion and (ii) scale linearly with bacterial concentration ρ_B. Those results are in line with previous reports of enhanced translational diffusivity of individual spheres in an active suspension [35], and extend the conclusions to tracers of complex shapes with a broader range of size. The same holds for rotational dynamics. This sets ρ_B as the relevant experimental parameter to control the activity of the bacterial bath.

The observation of the aggregates over the course of tens of minutes reveals a small but persistent angular rotation, $\Omega < 10^{-2}\text{rad/s}$, that was previously imperceptible at shorter times [Fig. 3.2D, Movie S2]. The rotation is consistently clockwise in experiments performed in the capillary [Fig. 3.2E-H], at a rate that increases with bacterial concentration ρ_B and decreases with aggregate radius R_G [Fig. 3.2I-inset]. Remarkably, the data collapses onto a master curve, $\Omega/(\mathcal{M}\cdot\rho_B) \propto 1/R_G^3$, where $\mathcal{M}$ is the mass of the aggregate [Fig. 3.2I]. It indicates a net torque $\tau \propto \mathcal{M}\cdot\rho_B$ imparted from the active bath to the aggregate and balanced by a viscous torque $\propto 1/R_G^3$. This linear dependence of the torque with the bacterial concentration ρ_B shows a cumulative effect of the bacteria bath leading to the rotation of the aggregates in a persistent (clockwise) direction. It notably departs from the non-chiral rotation that arises from the summation of randomly contributing bacteria in an aggregate [77]. Extracting the mobility μ_R from the measurements of rotational diffusivity in the thermal bath [Fig. 3.2B], we estimate the net torque exerted by the bacterial bath, $\tau_{R_G} = \mu_R \cdot \Omega(R_G) \sim 0.4$pN·µm for $R_G \sim 7$µm. This minute torque becomes significant in experiments of aggregations lasting a few hours. We intuit that the rotational symmetry-breaking originates from the native chirality of *E. coli* flagella, that leads to clockwise circular trajectories, with typical radius of curvature $R_B \sim 43$ µm [Fig. 2.5], near the no-slip boundary of the glass capillary [58]. Indeed, we can reverse the direction of rotation of the aggregates by performing experiments at the air-water interface of a pendant drop, where bacteria reverse direction of rotation into counterclockwise circles [57] [Fig. 4.1]. This corroborates that the chirality of *E. coli* flagella breaks the rotational symmetry and makes the bacterial bath effectively chiral.

In order to better understand the phenomenon, we consider a toy-model of a circular aggregate of radius a, in an active bath of persistent self-propelled rods. For simplicity, the self-propelled particles exert a constant force $\mathbf{F_0}$ aligned with their propulsion direction [SI; Fig. 4.3]. When the self-propelled particles navigate along straight segments, no net torque is exerted by symmetry, and the circular aggregate does not show persistent rotation [40, 41]. In contrast, when the self-propelled particles move along along circular clockwise trajectories, a wedge of unbalanced collisions appears. Its opening angle 2θ is controlled by the curvature $1/R_B$ of the trajectories, $\theta \sim 1/R_B$, [Fig. 4.3]. The asymmetric collisions lead to a tangential force of amplitude $F_{//} \propto 2\theta \cdot F_0$ exerting a torque onto the circular aggregate. The total torque, $\tau_{R_B} \propto \frac{F_0}{R_B} \cdot \rho_B a^2$, is obtained by integration over the perimeter and multiple collisions, leading to clockwise rotation of the circular aggregate. Hereby, this simple toy model highlights that an active chiral bath exerts an active torque onto a circular aggregate, which is absent for an active bath of straight swimmers. We further extend this result, showing that an active bath that results in constant tangential forces along the boundary of an aggregate produces a torque $\propto \rho \cdot \mathcal{A}$, proportional to the surface area $\mathcal{A}$ of the aggregate [SI]. Remarkably, this scaling, valid for aggregates of arbitrary shapes, agrees with the experimental results [Fig. 3.2I]. We however stress that the quantitative description of the rotation of the aggregates in the experiment certainly lies beyond this simple model, superimposing effects of complex shape of the aggregates, which can be locally asymmetric, as well as the forces exerted by the bacteria navigating inside the aggregate, as visible on [Fig. 2.5C]. The quantitative description of those effects lies beyond the scope of this paper and constitutes further work.

We now turn to the morphology and statistical properties of the colloidal aggregates formed in the thermal and active bath. In order to account for the accelerated dynamics of the active bath, we rescale time so that aggregates in the thermal and active bath reach the same average size. Aggregates formed after 25h (thermal bath) or 1h15 (active bath) reach comparable size, $\mathcal{M} = 150$ colloids, but are distinct to the naked eye [Fig. 5.2]. Thermal aggregates are ramified, as typical of DLCA, and a result of the low probability for a diffusing particle to reach the center of the aggregate. In contrast, aggregates of the active bath are compact and present cavities. Remarkably, aggregates formed in the thermal or active baths fall into distinct groups when representing the fraction of colloids on the perimeter, a salient control parameter in the mechanical response of gels [15][Fig. 5.5]. In order to further quantify morphological changes, we compute the fractal dimensions ν of an ensemble of aggregates, as $\mathcal{M}_i \propto R_{G,i}^{\nu}$, where $\mathcal{M}_i$ is the mass in units of colloids (or, number of colloids in the aggregate i) and $R_{G,i}$ the radius of gyration of aggregate i [See Fig. 3.3A]. Aggregates for which $\nu = 1$ are elongated, $\nu = 2$ are compact and intermediate values for ν are indicative of ramified, fractal structures. The fractal dimensions of the aggregates in the thermal as well as the active bath evolve in time before reaching a plateau after approximately 2 hours [Fig. 5.3]. The value of the fractal dimension measured in the thermal bath, $\nu_0 \sim 1.4$, are in line with reported values for DLCA in 2D [24]. As observed to the naked eye, aggregates in the active bath are more compact than in the thermal bath, reaching $\nu(\rho^*) \sim 1.8$ at the highest performed activity.

Aggregate morphology is further quantified via the normalized complementary cumulative size distribution, $\mathcal{P}$ [SI]. In the thermal bath, the size distribution of aggregates can be rescaled by the mean value, such that at all times the distributions collapse onto a single log-normal distribution [Fig. 2.2]; a universal feature of merging/fragmenting systems [52, 54]. In contrast, the size distribution of aggregates formed in the active baths cannot be collapsed and exhibits significant deviations from log-normal. Notably, tails become more prominent with increasing activity [Fig. 3.3B]. It results that aggregation in the thermal and active baths do not belong to the same universality class, highlighting a profound effect of the bacterial bath on the properties of aggregation[52, 54]. We intuit that those non-equilibrium properties originate in the compaction and folding of the aggregates that arise from the observed rotation [Fig. 3.4A]. In order to better understand the mechanism, we develop a minimal physical model aimed to capture the chirality of the bacterial bath without explicitly considering the swimming bacteria. We expect the chiral bath to cause aggregates of colloids to rotate and we model the system as an ensemble of attractive rotating beads coupled to each other by friction [Fig. 3.3C][SI]. The rotation is implemented in a mean-field fashion, attributing a constant torque to each bead. The simulations are similar in spirit to previous models of internally driven gears [78, 79] with the addition of strong attraction between the spinners. The latter leads to irreversible aggregation, a notable difference from crystals of rotating cells reported at moderate attraction [80]. The clockwise rotation of the beads is implemented via an internal driving torque whose amplitude controls the internal activity of the system, allowing comparison between the simulations and our experimental results. The numerical simulations capture visually the difference between aggregation in the thermal and active bath [Fig. 3.3D-E, Movies S3-S5]. They furthermore reproduce quantitatively the experimental increase in fractal dimensions and distributions of size of the aggregates [Fig. 3.3F-G], thus validating the predictive power of the model. Aggregates rotate and grow faster than thermal aggregation, in line with a simple model of aggregation-collision, accounting for the sweeping effect from rotation on the collision rate [Fig. 4.4]. The simulations, as the experiment, show two different effects of the rotation: *(i)* the mentioned sweeping motion of spinning aggregates and *(ii)* the self-folding of the aggregates [Fig. 3.4B, Movie S6]. In order to disentangle their role, we compare our initial set of simulations, where aggregates can deform as a result of the internal torques [Fig. 3.4C], with another set where aggregates are treated as rigid objects [Fig. 3.4D]. At low internal torque, both simulations of deformable and rigid aggregates form 2D gels [Fig. 3.4C,D]. The obtained structures are, however, markedly different. The gels formed by the percolation of deformable aggregates are structurally heterogeneous, with both compact and ramified regions [Fig. 3.4E]; the gels built from rigid aggregates appear more uniform in structure [Fig. 3.4G]. At sufficient internal torque, simulations of rigid aggregates lead to space-spanning networks that resemble thermal DLCA gels [Fig. 3.4G,H]. In contrast, simulations of deformable aggregates at high internal torques do not percolate; the internal torque folds the large, deformable aggregate onto themselves. This leads to large compact clusters with internal cavities [Fig. 3.4F] and prevents the formation of a percolated network [Fig. 3.4C]. The rotation enhances the dynamics of aggregation while the self-folding of the ramified aggregates controls their fractal dimension. This mechanism highlights the difference in the nature of the reported aggregation with conventional Reaction Limited Colloidal Aggregation, and leads to different morphologies [4]. We next investigate the phase behavior of aggregation for varying surface fraction Φ and internal torque and observe the existence of a gel and a cluster phase controlled by activity [Fig. 3.5A]. The (ν, Φ) diagram is obtained by measuring the fractal dimension of the aggregates and allows us to characterize the experimental data in bacterial baths [Fig. 3.4A-inset, Fig. 5.1]. The gel phase is separated from the cluster phase by a critical fractal dimension $\nu_C \sim d + \alpha \log \Phi$, where $d = 2$ is the dimension of space and $\alpha \sim 0.29$ is phenomenologically adjusted to the data – the scaling in $\log \Phi$ originating from the definition of $\Phi \propto \mathcal{M}$ [2]. Overall, sufficient activity suppresses the gel phase in favor of compact aggregates.

Having established that the activity of the bath controls the phase behavior of aggregation into a cluster phase or a gel phase, we next investigate the structural and mechanical properties within each phase. In the cluster phase, we observe that the porosity of aggregates is controlled by the internal activity. Increased internal torque augments the compaction of the aggregates, leading to dense and compact structures [Fig. 3.5B]. We next consider 2D gels (at $\Phi = 0.31$), that differ on whether they are assembled in a thermal bath or with internal activity. We probe those *passive* gels mechanically by performing numerically stress-strain measurements [Movies S7, S8]. Gels obtained by aggregation in the thermal bath exhibit a conventional elastic behavior in the limited range of considered strain $\sim 10\%$. In contrast, gels assembled with internal activity are highly non-linear and behave like mechanical diodes: elastic in compression and stiffening under extension [Fig. 3.5C]. The onset of the plastic regime also appears controlled by the activity of the assembly. In order to gain insight in the origin of this unconventional mechanical behavior, we perform additional experiments and simulations, at $\Phi = 0.39$, a surface fraction, for which we can experimentally achieve a 2D percolated network, greater than 1mm x 1mm in size in both the thermal or the bacterial baths. We use bacterial concentration up to $\rho_B = 0.1\rho^*$, beyond which the gel phase is replaced by the cluster phase, showing once again a solid agreement between our experiments and the phase diagram predicted numerically [Fig. 3.5A]. The gels achieved in the active baths display significant structural differences compared to those achieved thermally [Fig 6A-B]; this could, at first, be seen as surprising, considering that the added fluctuations of the bacterial bath are comparable to the thermal energy itself [Fig. 3.2C]. It simply highlights that the bacterial bath is more than a mere hot bath, and that the acquired rotation of the aggregates has profound effect on the dynamics and structure of the aggregates, as already apparent on the anomalous size distributions [Fig. 3.3B, G]. We quantify the structural differences by measuring number fluctuations of density in the gels [Fig. 3.6C]. We can define extract a typical length-scale for the gel structure by identifying the local maximum of the number fluctuations $\sigma^2(N)/\langle N \rangle$ [81]. As visible to the naked eye, the length scale grows from ~ 10 colloid diameter in the thermal gel to $\sim 30-40$ colloid diameters in the gels assembled in bacterial bath. Additionally, the emergence of giant number fluctuations (GNF) for gels assembled in the active bath highlight more heterogeneous structures compared to the passive bath. To further quantify this aspect, we characterize the pores of the 2D gels by computing the distance from points in the pore to the nearest colloid in the network backbone [82]; this distribution is plotted in [Fig. 3.6D]. Gels assembled in the active baths show broader distributions than gels assembled thermally, indicative of large heterogeneous voids in the structure. These structural heterogeneities arise from the rotation of aggregates induced by the chiral bacterial bath. The rotation results in the jamming of ramified aggregates into each other and the formation of large isostatic structures [Fig. 3.6B-inset]. Remarkably, our simple numerical model of rotating aggregates with internal torques once again show good agreement with the experimental realization of gels [Fig. 3.6F-G]. This highlights how rotation and folding of the aggregates is the key ingredient in shaping and forming heterogeneous structures and driving exotic mechanical responses. These results should be taken in relationship with the role of structural heterogeneities in determining the breaking and re-structuring of gels [83, 84]. Previous works reported that the moderate substitution of passive particles by active particles facilitate the annealing of colloidal monolayers [85, 86] or control the yield stress of gels [51, 87]. Our results highlight how the assembly in an active bath directs the structural and mechanical properties of materials entirely made of passive constituents. We are hopeful our results will stimulate future work to provide a complete microscopic model that translates aggregation in bacterial baths into the design of gels with unconventional mechanical response.

In summary, we demonstrate that active baths are a potent instrument to devise unconventional aggregates and gels and that activity is a salient parameter for phases of matter out-of-equilibrium. It is noticeable that simulations of a purely active system of spinners reproduce quantitatively experimental results of passive particles in a chiral bacterial bath, possibly highlighting generic features between these two classes of systems. The importance of chirality in morphogenesis [88, 89, 90] further hints to the potential of chiral active baths to achieve materials beyond thermal. While our study is limited to 2D, it is a proof of concept for materials powered from within, in phases and structures not achieved via thermal treatments, as also recently highlighted in the effect of activity on liquid interfaces [48]. It will motivate efforts to assemble 3D materials in active baths, while the characterization of their non-conventional mechanical and rheological properties will drive further experimental and theoretical work. This work effectively lays out a roadmap establishing the concept of *bacterial forging*, where gels structures are controlled by the bacterial bath, the way forging in metallurgy controls the properties of metals through sequences or annealing and quenching. Because activity can in principle be controlled in time and space externally [43], our findings open up a branch of materials science, where the properties of passive materials are tailored upon their assembly in active baths and active materials are supplied with energy as desired, to induce healing or annealing.

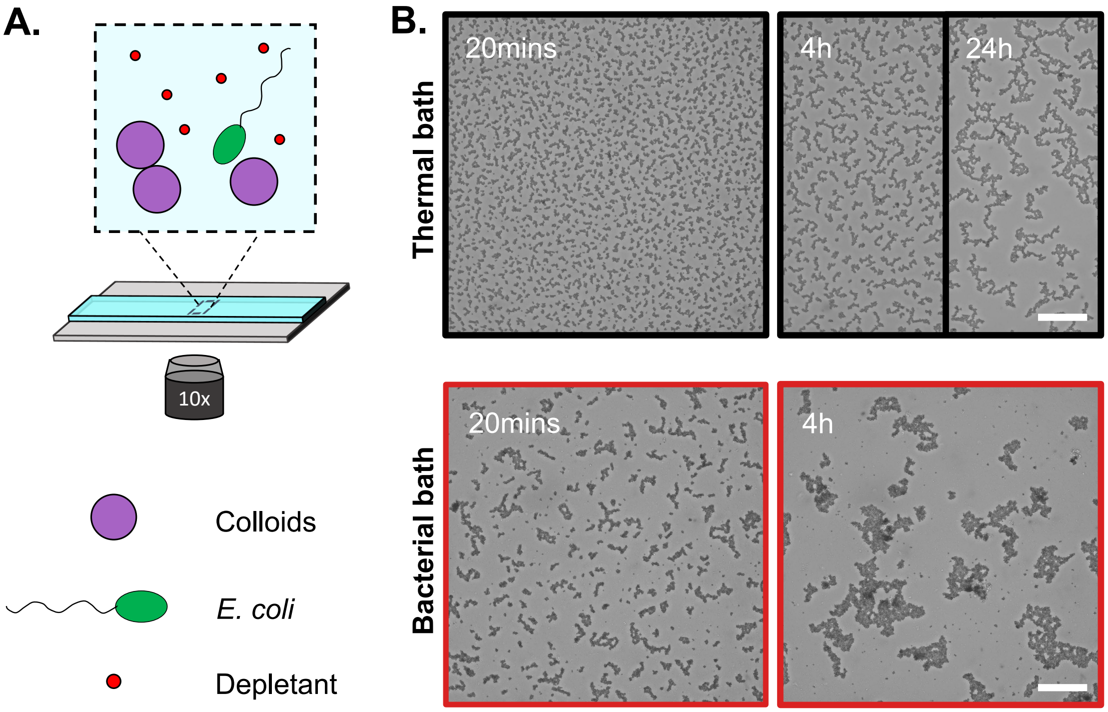

Figure 3.1. A) Sketch and components of the experiment of aggregation of sticky beads. Colloidal beads (purple) are mixed with depletant (red) that controls the strong attraction between the colloidal beads. The suspension is mixed with either pure motility medium (the thermal bath) or swimming *E. coli* bacteria (green) suspended in motility medium (the bacterial bath). **B)** Bright-field images of the colloidal aggregation after 20mins, 4h and 24h in a thermal bath (top, black) and after 20mins and 4h in an active bath (bottom, red) with bacterial concentration $\rho_B \sim \rho^* = 6 \cdot 10^8 \text{cells/mL}$. Scale bars are $100\mu m$.

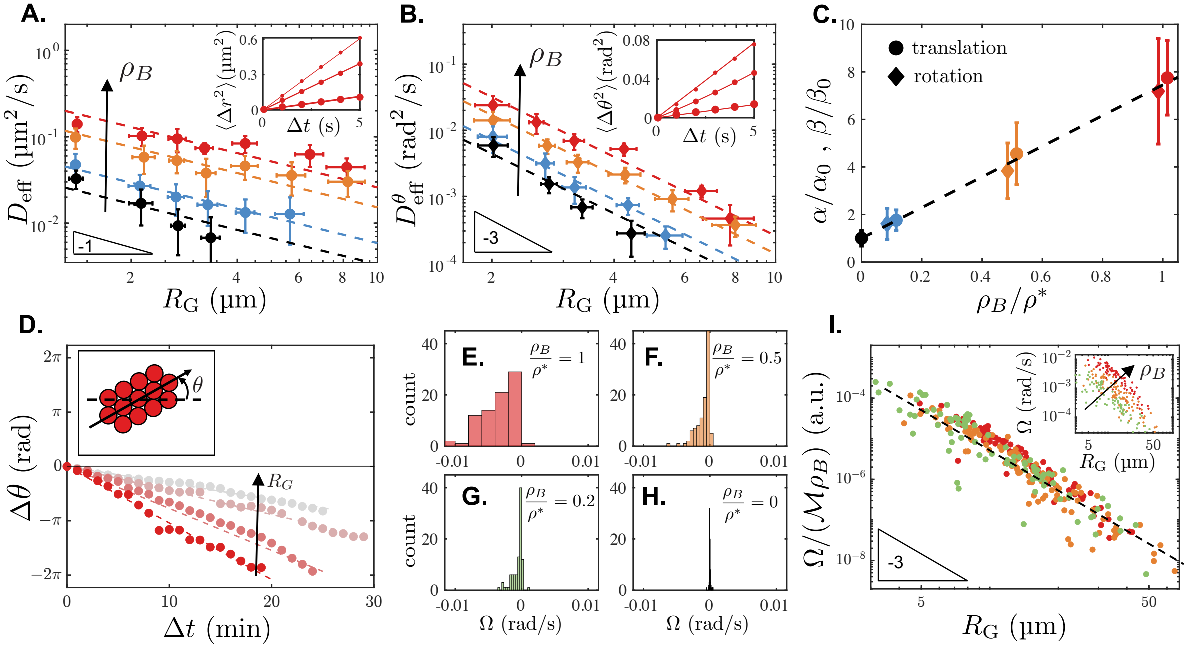

Figure 3.2. Short time dynamics of the aggregates ($\Delta t < 5s$). **A-inset)** Mean Squared Displacement (MSD) for fixed bacterial concentration $\rho_B = \rho^*$ and increasing aggregates' size R_G (larger symbol for larger R_G). The MSD increases linearly with time allowing to measure an effective diffusivity $D_{\mathrm{eff}}(\rho_B, R_G)$. **A)** Translational diffusivity D_{eff} for various bacterial concentration ρ_B and aggregates' size R_G (black is thermal and hotter color represents higher ρ_B). For each bacterial concentration, $D_{\mathrm{eff}} = \alpha(\rho_B)/R_G$ as predicted by Stokes-Einstein relationship for a thermal bath (dashed lines). Each point represents an average over at least 5 aggregates. **B-inset)** Mean Squared Angular Displacement (MSAD) for fixed bacterial concentration $\rho_B = \rho^*$ and increasing aggregates' size R_G, (larger symbol for larger R_G). The MSAD increases linearly with time, allowing to measure an effective diffusivity $D^{\theta}_{\mathrm{eff}}(\rho_B, R_G)$. **B)** Rotational diffusivity $D^{\theta}_{\mathrm{eff}}$ for various bacterial concentration ρ_B and aggregates' size R_G (black is thermal and hotter color represents higher ρ_B). For each bacterial concentration, $D^{\theta}_{\mathrm{eff}} = \beta(\rho_B)/R_G^3$ as predicted for Stokes-Einstein relationship in a thermal bath (dashed lines). Each point represents an average over at least 5 aggregates. **C)** Normalized diffusivity in translation, α/α_0 (circles) and in rotation, β/β_0 (diamonds), where subscript 0 refers to the thermal bath. Normalized translational and rotational diffusivity collapse. The symbols are slightly offset on the horizontal axis for clarity. **Long time dynamics of the aggregates. D)** Persistent clockwise rotation of aggregates observed at longer times (minutes to tens of minutes) in the glass capillary. The linear dependence of the angle θ allows to extract a rotation rate $\Omega(\rho_B, R_G)$. **E-H)** Histograms of rotation rates Ω for different bacterial concentration ρ_B for all aggregates sizes R_G. **E)** $\rho_B = \rho^*$, **F)** $\rho_B = 0.5\rho^*$, **G)** $\rho_B = 0.2\rho^*$, **H)** $\rho_B = 0$, thermal. **I-inset)** Rotation rates Ω for different bacterial concentrations ($\rho_B \sim 0.2\rho^*$ (green), $\rho_B \sim 0.5\rho^*$ (orange) and $\rho_B \sim \rho^*$ (red), with $\rho^* = 6 \cdot 10^8$cells/mL) and aggregates sizes R_G. **I)** Data collapse onto the master curve $\Omega/(\mathcal{M}\rho_B) \propto 1/R_G^3$, where $\mathcal{M}$ is the mass of the aggregate. Each point represents a measurement for an aggregate.

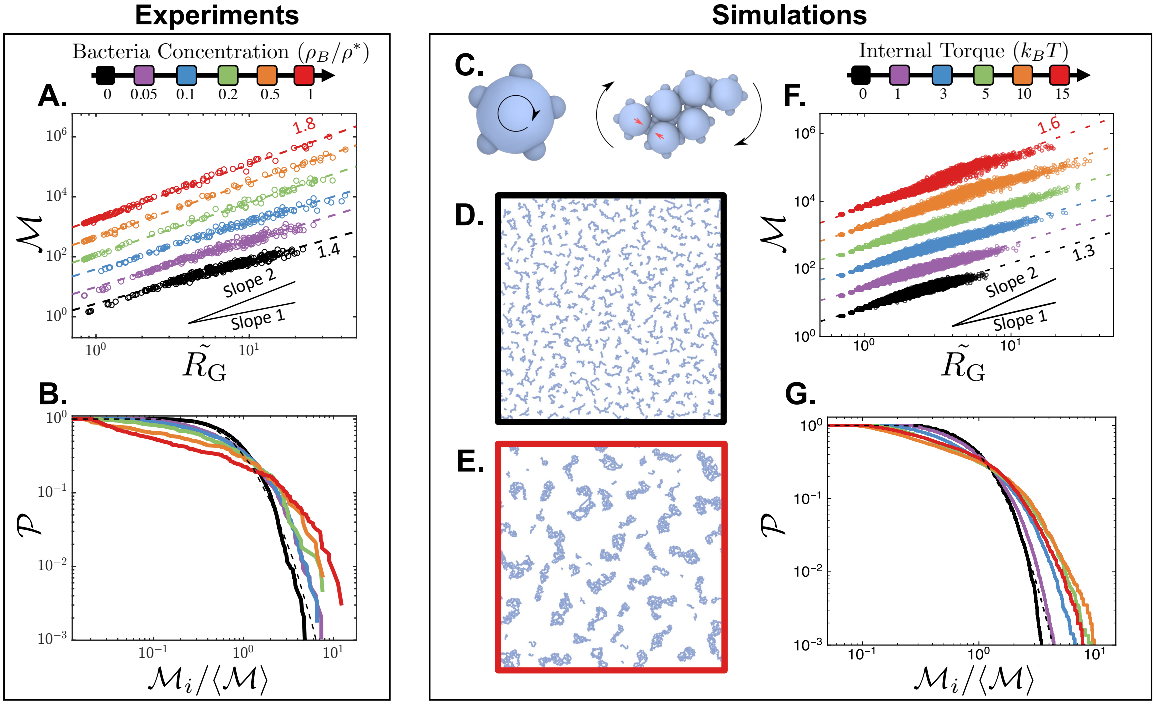

Figure 3.3. Aggregate morphology A, B: Experiments. A) Measurements of the fractal dimension, ν, with $\mathcal{M} \propto \tilde{R}_G^{\nu}$ of aggregates of radii $\tilde{R}_G = R_G/a$, where a is the radius of a colloidal bead, and mass $\mathcal{M}$ and **B)** Complementary cumulative size distributions $\mathcal{P}$ of the aggregates for increasing bacterial concentration ρ_B (black:thermal, ranging from $0.05\rho^*$ to ρ^* - see colorbar). The black dashed line is the log-normal distribution predicted for passive colloidal aggregation. In both A and B, aggregates are characterized after 4 hours. **C-G: Simulations. C)** Sketch of the numerical model of active spinners with internal torque and attractive interactions coupled by tangential friction [SI]. **D-E)** Snapshots of the simulations of our minimal model for **D)** thermal (black) or **E)** active with an internal torque (red) [see main text], resembling the experimental results of [Fig.1B]. **F)** Measurements of the fractal dimension $\mathcal{M} = R_G^{\nu}$ of aggregates in simulations and **G)** Complementary cumulative size distributions $\mathcal{P}$ of the aggregates with increasing internal torque (see colorbar). The black dashed line is the log-normal distribution predicted for passive colloidal aggregation.

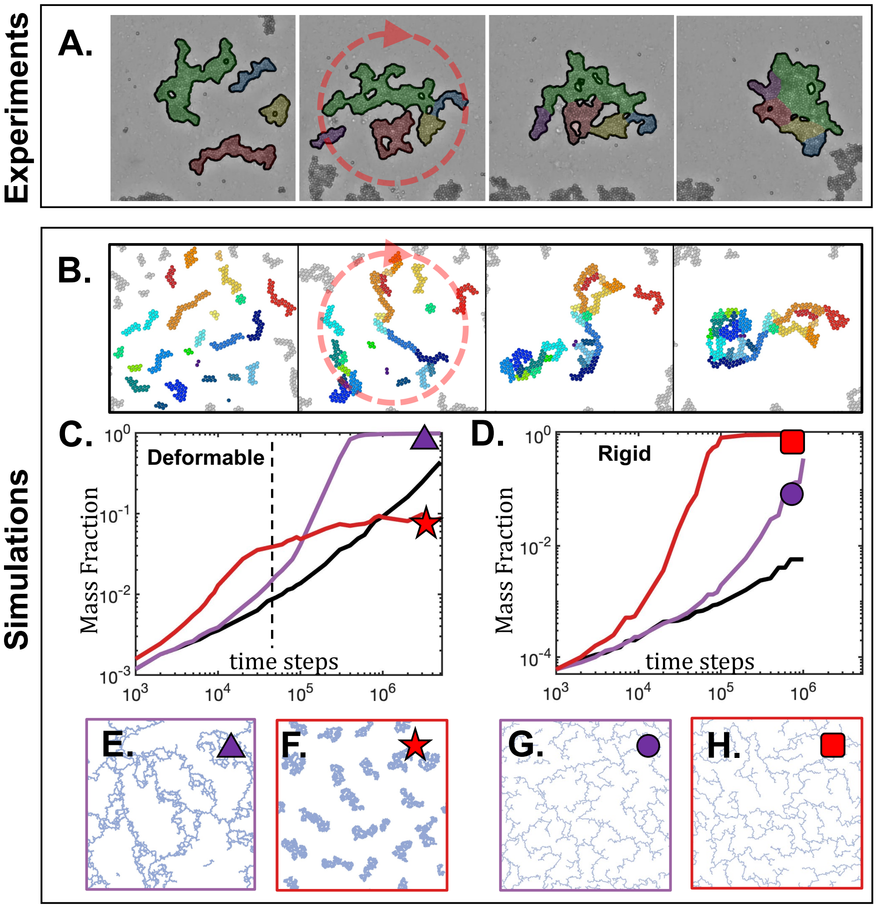

Figure 3.4. **A, B)** Rotation and folding of aggregates in **A: experiments** and **B: simulations** leading to the compaction of the aggregates in active bath. Red arrows indicate the direction of rotation of the aggregates.**C-H: simulations.** Colors indicate the internal torque, with $0k_\mathrm{B}T$ (black), $1k_\mathrm{B}T$ (purple), and $15k_\mathrm{B}T$ (red). **C,E,F:** Simulations of deformable aggregates (see main text) **C)** **C-H: simulations.** Colors indicate the internal torque, with $0k_\mathrm{B}T$ (black), $1k_\mathrm{B}T$ (purple), and $15k_\mathrm{B}T$ (red). **C,E,F:** Simulations of deformable aggregates (see main text) **C)** Time evolution of the mass fraction of the largest aggregate in the system for increasing internal torque of the spinner. Mass Fraction is the fraction of colloids contained in the largest aggregate with respect to the total number of colloids. The rotation of aggregates accelerates growth in comparison with thermal aggregation (black line). In the thermal case and at low activity, the largest aggregate grows until incorporating all particles to form a percolated structure and a space-spanning network as visible on the snapshot of the simulation presented on **(E)** (corresponding to the purple triangle on panel C). At sufficient activity (red curve), large aggregates fold and the largest cluster become more compact, exhibiting a plateau of growth (vertical dashed line). The gel phase is suppressed, replaced by compact clusters, with cavities as visible on the snapshot of the simulation presented on **(F)** (corresponding to the red star on panel C). **D,G,H:** Simulations of rigid aggregates (see main text) **D)** Time evolution of the mass fraction of the largest aggregate in simulations of rotating rigid aggregates, without folding . (**G, H**) Snapshots of the simulations as indicated by the symbols on panel D). They show the formation of a percolated structure for all activity (internal torque). The folding is responsible for the suppression of the gel phase at higher activity.

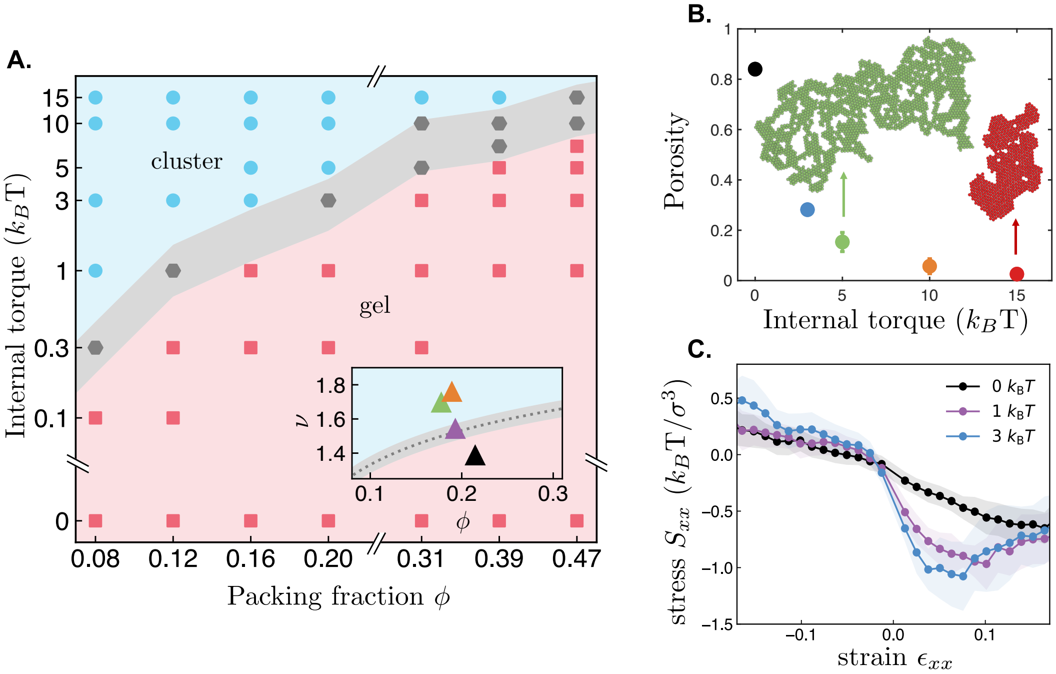

Figure 3.5. (A) Phase diagram of the colloidal aggregation for varying internal torques and surface fractions showing the existence of a space-spanning gel phase (pink, squares are simulations data) and cluster phase (blue, circles are simulations data) controlled by activity. **(A-inset)** Phase diagram in (ν, Φ) variables obtained by measuring the fractal dimension of the aggregates. A gel phase (pink) is separated from a cluster phase (blue) by a critical fractal dimension $\nu_C \sim 2 + 0.29 \log \Phi$ (dashed line) [see main text for the scaling]. Triangle symbols are the experimental data for different activity: thermal (black), $\rho_B = 0.05\rho^*$ (purple), $\rho_B = 0.2\rho^*$ (green) and $\rho_B = 0.5\rho^*$ (orange). **(B) Activity control of the structure of aggregates.** Simulations performed at constant $\Phi = 0.16$. The system is in a gel phase in the thermal bath (black circle) and, for all other represented activities, forms compact clusters (shown as insets), whose porosity is set by the internal torque. **(C) Mechanical stress-strain curves of** ***passive*** **gels**, whose initial structures are prepared through thermal (black) or active aggregation set by the amplitude of the internal torque as indicated by the color of the curve: $1\,k_BT$ (purple) and $3\,k_BT$ (blue). All simulations are performed for $\Phi = 0.31$. The extensile response (positive strain) is markedly different for gels obtained *via* thermal or active aggregation. The gels assembled in the thermal bath respond linearly and symmetrically, behaving as an elastic solid in the considered range. The gels achieved through active aggregation are highly non-linear, elastic in compression and stiffening under extension. Compression and extension curves are performed independently and plotted on the same figure [see SI for the deformation protocol].

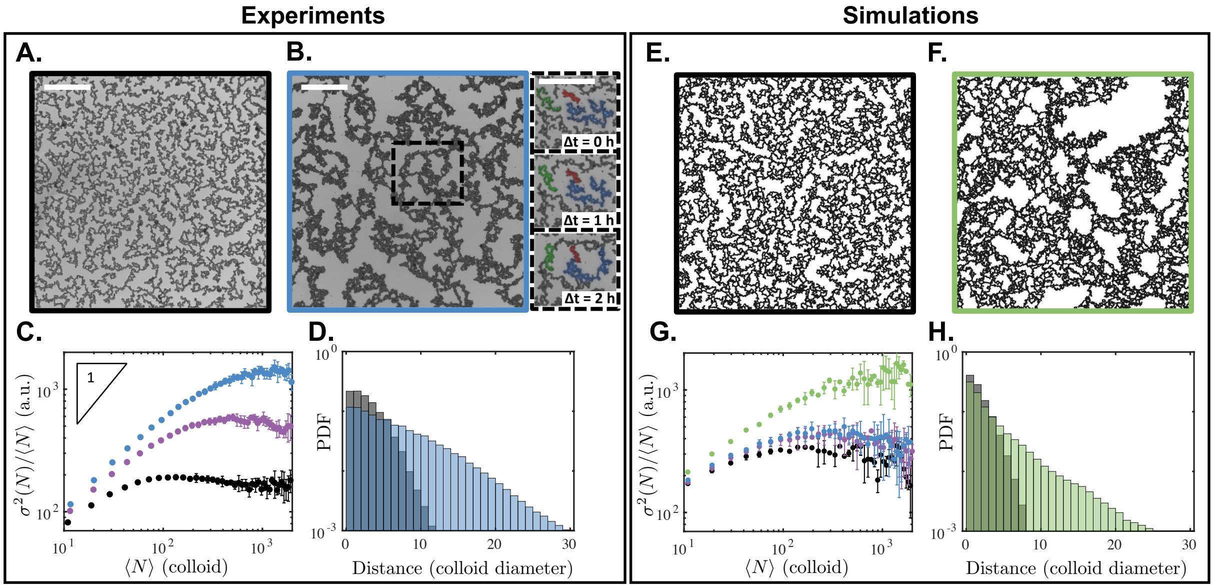

Figure 3.6. A-D: Experiments. A, B) Bright-field image of a 2D colloidal gel aggregated in **(A)** a thermal bath ($\rho_B = 0$) and **(B)** an active bath ($\rho_B = 0.1\ \rho^*$). Scale bar is 200 µm. **B-inset)** Time-lapse showing the formation of large heterogeneities via the rotation and jamming of large aggregates. Scale bar is 200 µm. **C)** Number fluctuations $\sigma^2(N)/\langle N\rangle$ of colloidal gels aggregated in thermal bath and active bath of various strengths [SI]. **D)** Probability density function of the distance from the colloidal backbone to points of the pores. Black is the thermal bath ($\rho_B = 0$) and blue is the active bath ($\rho_B = 0.1\ \rho^*$). **E-H: Simulations. E, F)** Snapshot of simulated 2D colloidal gels, aggregated at **(E)** internal torque = 0 k_BT and **(F)** internal torque = 5 k_BT. **G)** Number fluctuations $\sigma^2(N)/\langle N\rangle$, calculated from simulated colloidal gels. **(H)** Probability density function of distance to the nearest colloid for all pixels in holes in the simulated colloidal gels. Black is a gel aggregated at internal torque = $0k_BT$ and green is internal torque = $5k_BT$. The simulations show again a solid agreement with the experiments.

Chapter 3, in full, is a reprint of the material as it may appear in Nature Physics, 2023. Daniel Grober, Ivan Palaia, Mehmet Can Ucar, Edouard Hannezo, Anđela Šarić, Jérémie Palacci. The dissertation author was the primary investigator and author of this paper.

Chapter 4

Further discussion and results on the rotation of aggregates

The persistent, clockwise rotation of aggregates is the salient feature of the unconventional aggregation reported in the previous chapter; the following section expands upon this observation. The chapter is broken up into 3 sections: Section 4.1 builds an intuition for the swimmer - aggregate interactions, based on both additional experiments and a review of theoretical models available in literature. Section 4.2 develops a microscopic model to explain the persistent clockwise rotation, based on the knowledge built in the previous section. Finally, Section 4.3 discusses the effect of a clockwise persistent rotation of aggregates on the mass distribution and growth rate.

4.1 Source of aggregate rotation: theory and experiments

This section begins by discussing additional colloidal aggregation experiments, performed on an inverted drop. The experiments performed in Chapter 3 take place on the bottom surface of a sealed glass capillary (solid-liquid interface), where *E. coli* swim in clockwise, circular trajectories [58]. On a liquid-air interface (i.e. the bottom of an inverted drop) *E. coli* trajectories reverse direction, swimming in counter clockwise circles [57]. These experiments establish a positive correlation between the direction of rotation of the aggregates and the chirality of *E. coli* trajectories. We further our understanding of the interactions between swimmers and aggregates by reviewing the experiments using green fluorescent protein labeled bacteria, as well as a review of the literature, promoting a collision - based model for the swimmer - aggregate interactions. This information motivates our model for how the aggregates in the bacterial bath rotate, presented in the following section (Section 4.2).

4.1.1 Inverted drop experiments

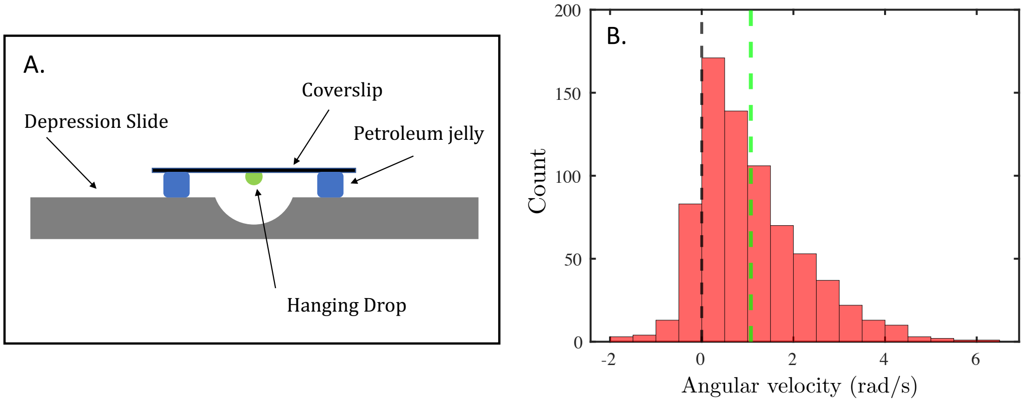

Figure 4.1. **(A)** Sketch of the experimental set up for the inverted drop experiment. **(B)** Distribution of angular velocities for all clusters tracked during the aggregation experiment on an inverted drop; the bacteria concentration is $\rho_B = 6 \times 10^8$ cells/mL. The black dashed line is zero, and the green dashed line is the average angular velocity.

We perform colloidal aggregation experiments on the bottom surface of a hanging drop [Fig. 4.1A]. In doing so, we are able reverse the fluid boundary condition at the interface where the experiment takes place: a no-slip condition at the bottom of a glass capillary becomes a near perfect-slip fluid-air interface at the bottom of a hanging drop. A 10 µL drop of the Colloidal Aggregation Solution, described previously, is suspended between a coverslip and a circular depression glass slide, as represented in Fig.4.1A. We observe the apex of the drop, capturing a series of 3000 frame videos at 20 fps using a 20x Nikon objective (NA 0.45). We observe that all colloids in the field of view are in focus, ensuring that the surface of the drop is locally flat. Following the tracking protocol described in Chapter 5, we extract information about the rotational dynamics of the aggregates from a linear fit between orientation and time for trajectories longer than 100 frames. We observe that 86% of clusters rotate counter clockwise

[Fig. 4.1B], reversing direction from the previous experiments. These results are reminiscent of the findings of Di Leonardo et al. [57], who found that *E. coli* swim in counter-clockwise circles at a liquid-air interface, due to the perfect-slip boundary conditions.

Summary: Inverted drop experiments

Performing experiments on an inverted drop (liquid-air interface), we find that aggregates rotate counter clockwise, reversing direction from the previous experiments performed on a solid-liquid interface. Di Leonardo et al. [57] found that *E. coli* reverse the chirality of their trajectories on a liquid-air interface, swimming in counter clockwise circles. This establishes a positive correlation between the direction of rotation of the aggregates, and the chirality of the swimmer trajectories.

4.1.2 *E. coli* trajectories swimming through aggregates

In this section, we review Fig. 2.5C, originally introduced in Chapter 2. This figure displays trajectories of *E. coli* interacting with a colloidal aggregate; trajectories are color coded, such that blue represents the initial position of the bacterium and red the final position. We observe that the *E. coli* swim through the aggregate, as opposed to scattering off the perimeter. Additionally, we notice that the *E. coli* swim in clockwise, curved trajectories before entering the aggregate, but approximately straight trajectories once inside.

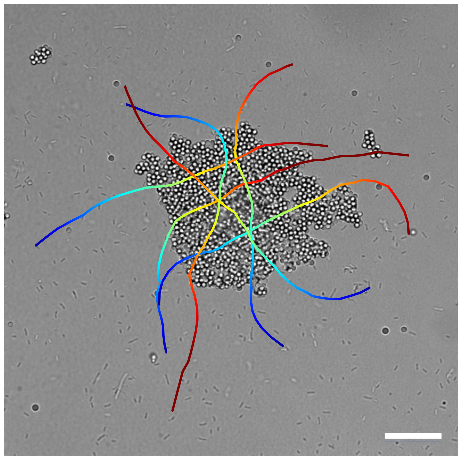

Figure 4.2. *E. coli* trajectories swimming through a colloidal aggregate. Trajectories are captured using confocal microscopy and overlaid on a bright-field image of the aggregate. Within each trajectory, color indicates time, with blue the initial position. Scale bar 50 µm. This figure originally appears in Chapter 1 as Fig. 2.5C.

4.1.3 Swimmer-tracer interactions (review of theoretical models)

The mechanism behind enhanced diffusion of passive tracers in a bath of active swimmers (Section 1.3.2) is an active field of research, with a variety of mechanisms proposed. The literature can be generally broken into three sections: far-field hydrodynamics, near-field hydrodynamics, and collisions. We first review the relevant literature, and finally relate these models to the experimental observations.

Experimental findings of Leptos et al. [38] reported that 1 µm tracers made large, looped trajectories in a bath of *C. reinhardtii*. Many models, based on far-field hydrodynamic interactions, have been developed to explain how these looped trajectories relate to the observed enhanced diffusion. Dunkel et al. [91] proposed that the tracer is displaced by far-field hydrodynamic flows generated by the swimmer. The authors find that, in the limit of low Reynolds, tracer particles execute large, quasi-closed loops as the swimmer passes, with the exact shape of trajectory determined by the hydrodynamic model of swimmer. In the case of a hydrodynamic pusher such as *E. coli*, the particle is first pushed away from the swimmer, and then pulled back to nearly the same position as the swimmer passes. Minõ et al. adapted this to model the enhanced diffusion of passive tracers interacting with motile *E. coli* near a wall [36]. Notably, the net displacement of the tracer over a quasi-closed loop is independent of the swimmer speed (a result of low RE dynamics); the dependence on “active flux”, as measured experimentally, manifests in the frequency of looping events (i.e. how often a tracer encounters a bacteria), which is proportional to the swimmer concentration and the swimmer speed [36]. Several similar models have been proposed, namely a general model for both 2D and 3D enhanced diffusion [92], as well as incorporating run and tumble swimmer dynamics [93]. All of these models approximate the tracer as a point particle, such that the tracer velocity can be interpreted at the fluid velocity at its center of mass; it is unclear how this approximation fares in the case of aggregates, orders of magnitude larger than the swimmer.

Other works have focused on hydrodynamic entrainment, the process by which a swimmer moving near to a tracer deforms the fluid and drags the tracer along with it, similar to the wake on a boat [94] [93]. Recent experimental and theoretical work [39], concerning the motion of passive tracers in a bath of *C. reinhardtii* has built upon the work of Leptos et al. [38]. Jeanneret et al. [39], argue that the looping mechanism identified previously makes a negligible contribution to the motion of tracers; rather, they propose that tracer dynamics are dominated by rare ”jumping” events where tracers become directly entrained in the wake of a swimming algae. Additional theory suggests that the size of the active swimmer determines the effectiveness of hydrodynamic entrainment, with *E. coli* being too small to effectively entrain a 1μm tracer [95].

Recent work by Lagarde et al.[59] has provided experiments of single *E. coli* scattering off 5 μm tracer particles, coupled with a minimal collision based model. They track the center of mass of both the *E. coli* and the tracer during many individual scattering events; placing the incoming *E. coli* along the x-axis, they determine that the displacement in the y-direction of the tracer and *E. coli* typically opposite. This observation seems to rule out hydrodynamic entrainment as a dominant effect. Additionally, they observe no average displacement of the tracer if the incident bacterium never gets closer than 1 colloid radius from the center of the colloidal tracer; this seems to rule out far-field hydrodnamics, via the previously described looping mechanism. Lagarde et al. propose a simple model which credibly reproduces their experimental findings, only considering normal forces applied to the surface of the colloid.

Summary: theoretical models

While we cannot rule out near or far field hydrodynamic effects, the results of Lagarde et al. [59] suggest that **collisions are the dominant interactions between** *E. coli* **and large, passive colloids**. These results are in line with initial experiments, observing that *E. coli* collide with and swim through aggregates [Fig. 2.5C]. In the following section we develop a collision based model for the persistent rotation of aggregates, as observed in experiments.

4.2 Collision-based model for rotation of aggregates

In the following section, we develop a model which explores the experimentally observed rotation of the aggregates. The model is collision based, and predicts that the aggregate rotates in the same direction as the chiral *E. coli* trajectory, in line with the findings in Section 4.1. Notably, the model describes a torque applied to the aggregate proportional to the concentration of bacteria times the surface area of the aggregate ($\tau \propto \rho \mathcal{M}$), in line with the experimental observations [Fig. 3.2I].

We begin with a toy model describing the collisions between a chiral swimmer and a circular aggregate. Later, we apply Stokes' theorem to determine the applied torque from a constant force per unit length applied along the perimeter of a 2D aggregate.

4.2.1 Toy Model: Net torque applied by an active chiral bath on a circular aggregate

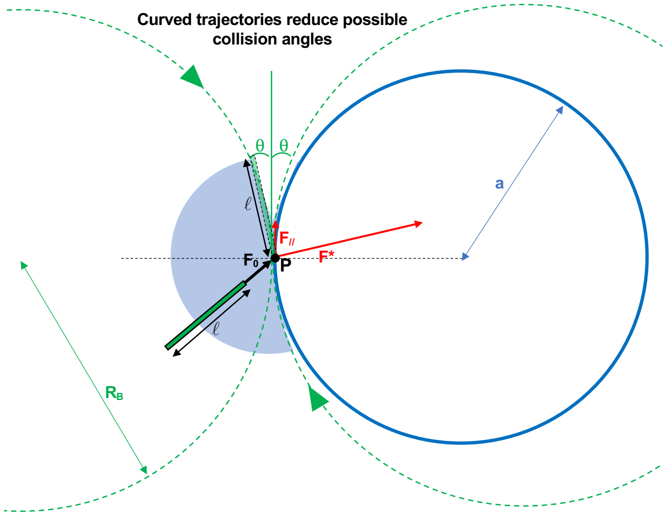

Figure 4.3. Toy Model. A circular aggregate with radius a is surrounded by self-propelled particles of length ℓ, whose center of mass follow circular clockwise trajectories with curvature radius $R_B > a$. Due to the curvature of the trajectories, a wedge of unbalanced collisions appears, with opening angle 2θ. The asymmetry of collisions lead to a tangential component of the force: $F_{//} \propto 2\theta F_0$. This leads to a net torque and the clockwise rotation of the circular aggregate [see model below]. The scale of objects are magnified on the scheme for clarity.

Self-propelled particles going along straight trajectories do not generate a net torque and rotation of symmetric gears. In contrast, they exert a torque leading to the rotation of asymmetric gears, a ratchet effect resulting from asymmetric collisions with the gears [40, 41]. Hereby, we show that the collisions of active particles propelled along chiral curved trajectories lead to the persistent rotation of a circular aggregate. This active torque exerted by the chiral active bath onto a circular aggregate is absent from a conventional active bath of straight swimmers.

To provide an intuitive picture, we introduce a toy model of a circular aggregate of radius a surrounded by self-propelled rods, of length ℓ. The center of mass of the self-propelled rods follows clockwise curved trajectories of radius of curvature R_B. The self-propelled particles exert a constant force $\mathbf{F}_0$ aligned with the propulsion direction and applied to the point of contact during collision with the circular aggregate. This effectively accounts for the existence of normal and tangential forces between the self-propelled particles and the aggregate. The self-propelled rods are homogeneously distributed with surface fraction σ_B. We consider situations where typically $R_B > a$, as on the Figure above [Fig. 4.3].

Case of straight swimmers. A point P on the perimeter of the circular aggregate can be hit by self-propelled particles with all incoming angles. By symmetry and on average, the resultant of the forces from the collisions in P is normal to the surface. It results that the net torque on the circular aggregate vanishes: $\tau_\infty = 0$. The circular aggregate does not rotate in an active bath of straight swimmers.

Case of swimmers with curved chiral trajectories. We now consider self-propelled rods, whose center of mass follow clockwise curved trajectories (similar reasoning applies for a bath of chiral, counter-clockwise self-propelled particles). Due to the curvature of the trajectories, a wedge of unbalanced collisions appears, with opening angle 2θ [Fig. 4.3], where the angle θ is controlled by the curvature of the trajectory and the steric hindrance of the self-propelled particle: $\theta \sim \ell/R_B$. The deficit of collisions at point P from this region leads to the emergence of a a tangential component of the force in addition to a normal component of the force. Only this tangential component will contribute a torque onto the circular aggregate, so that we do not attempt to evaluate the normal component of the force. The tangential force is estimated to be $\mathbf{F}_{//} \propto 2\theta \cdot F_0\,\mathbf{u}$, where $\mathbf{u}$ is the unit tangent vector to the circle in P. Integrating over the perimeter and in time (over multiple collisions), we estimate the net torque from the active chiral bath $\tau_{R_B} \propto \frac{\ell}{R_B} \cdot F_0 \cdot a^2 \cdot \sigma_B$. In effect, the circular aggregate rotates clockwise in a bath of bacteria with curved clockwise trajectories. The salient feature of this toy model is to show the chiral bacterial baths exerts an active torque onto a circular aggregate, a feature absent from a conventional active baths of straight swimmers.

The scaling of the internal torque we obtain in this simple model is compatible with the scaling observed experimentally on [Fig. 3.2I], with $\mathcal{M} \sim a^2$ for compact shapes and $\rho_B \propto \sigma_B$, by integration of the density in 2D. We however stress that the quantitative description of the rotation of the aggregates in the experiment certainly lies beyond this toy model. The rotation in the experiment is likely the superposition of multiples effects of *(i)* the complex shape of the aggregates, which be locally symmetric/asymmetric or even chiral, *(ii)* the details of the microscopic transmission of forces between the bacteria and the walls, notably friction with the wall, *(iii)* the forces exerted by the bacteria navigating inside the aggregate, as visible on [Fig.2.5C] and the *(iv)* steric effects of bacteria size or hindering of the motion of flagella due to the walls. The quantitative description of those effects lies beyond the scope of this paper and constitutes further work.

4.2.2 Torque applied by a constant tangential or normal force on each point of the boundary of a 2D object

In the previous toy model, we described how chiral circular trajectories result in an imbalance in collisions at every point along the boundary of a circle, resulting in a net torque on the circle. Remarkably, the tangential force from collisions $\mathbf{F}_{//} \propto 2\theta \cdot F_0\,\mathbf{u}$ is constant along the perimeter of the circular aggregate. The normal force is similarly constant along the perimeter of the circular aggregate. Following, we aim to extend our results and investigate the effect of **constant** tangential or normal forces applied on each point of of the boundary onto the rotation of an 2D aggregate of arbitrary shape. We first derive the implications of those (strong) assumptions, before discussing their relevance in light of our experiments.

We place the center of mass of the object at the origin. The boundary is defined by the curve $\mathcal{C}$, oriented counter-clockwise, parameterized by $x = x(t)$ and $y = y(t)$ for $a \leq t \leq b$, such that

$$\mathbf{r}(t) = x(t)\mathbf{i} + y(t)\mathbf{j}$$

where **i**, **j** and **k** are fixed unitary vectors in cartesian coordinates. The force per unit length can be decomposed into a component normal to the boundary, as well as and a tangential component parallel to the boundary. We consider here only the case of **constant** normal or **constant** tangential forces. We start by analyzing the component acting parallel to the boundary.

Force parallel to the boundary

We consider the case where at each point along the boundary, a constant force per unit length is applied parallel to the boundary. We note that the line element $d\mathbf{r}$ is oriented parallel to the curve at every point along the curve $\mathcal{C}$. Thus, we can write the infinitesimal force (f_p) applied parallel to the object at each point along the boundary as

$$f_p = \beta(d\mathbf{r}) = \beta(dx\mathbf{i} + dy\mathbf{j})$$

Where β is a constant of units force per unit length. The net force applied to the object (F_p) is written as an integral of the infinitesimal force over the curve $\mathcal{C}$.

$$F_p = \oint_{\mathcal{C}} f_p = \beta \oint_{\mathcal{C}} dx\mathbf{i} + dy\mathbf{j}$$

The net force F_p is zero, as the curve $\mathcal{C}$ is a closed loop. The net torque (T_p) applied is given by $r \times f_p$ integrated over the curve $\mathcal{C}$

$$T_p = \oint_C r \times f_p = \beta \oint_C (x\mathbf{i} + y\mathbf{j}) \times (dx\mathbf{i} + dy\mathbf{j})$$

We recognize that the torque only acts in the **k** direction.

$$T_p = (\beta \oint_C xdy - ydx)\mathbf{k}$$

And the magnitude of the torque (T_p) takes the form of a line integral. Defining the vector field $G = -y\mathbf{i} + x\mathbf{j}$, we can re-arrange the integral to take the form

$$T_p = \beta \oint_C G \cdot d\mathbf{r}$$

Applying Stokes' theorem, the line integral for T_p can be related to an integral over the surface $\mathcal{S}$ whose boundary is $\mathcal{C}$. We note that the curve $\mathcal{C}$ is oriented counter clockwise in the $(\mathbf{i}, \mathbf{j})$ plane, such that the surface $\mathcal{S}$ is oriented in the direction **k**.

$$T_p = \beta \iint_{\mathcal{S}} (\text{curl } G) \cdot \mathbf{k} \, dA$$

Reminded that the vector field $G = -y\mathbf{i} + x\mathbf{j}$, we find that curl $G = 2\mathbf{k}$. Thus, the surface integral for T_p is written as

$$T_p = 2\beta \iint_{\mathcal{S}} dA \tag{4.1}$$

Here, we show that a constant tangential force applied at each point of the boundary of a 2D object produces a net torque that is proportional to the surface area $\mathcal{A}$, irrespective of the shape of the object! In addition, because, we expect the prefactor β to be proportional to the density of self-propelled particles, this result shows an active torque proportional $\propto \rho \cdot \mathcal{M}$ as observed experimentally [Fig. 3.2I], since area, $\mathcal{A}$, and mass $\mathcal{M}$ of an aggregate are proportional to each other.

Force normal to the boundary

We note that the line element $d\mathbf{r} \times \mathbf{k}$ is oriented normal to the curve at every point along the curve $\mathcal{C}$. Thus, we can write the infinitesimal force (f_n) applied normal to the object at each point along the boundary as

$$f_n = \alpha(d\mathbf{r} \times \mathbf{k}) = \alpha(dy\mathbf{i} - dx\mathbf{j})$$

Where α is a constant of units force per unit length. The net force (F_n) applied to the object is written as an integral of the infinitesimal force over the curve $\mathcal{C}$

$$F_n = \oint_{\mathcal{C}} f_n = \alpha \oint_{\mathcal{C}} dy\mathbf{i} - dx\mathbf{j}$$

We note that the net force F_n is zero, as the curve $\mathcal{C}$ is a closed loop. The net torque (T_n) applied is given by $r \times f_n$ integrated over the curve $\mathcal{C}$.

$$T_n = \oint_{\mathcal{C}} r \times f_n = \alpha \oint_{\mathcal{C}} (x\mathbf{i} + y\mathbf{j}) \times (dy\mathbf{i} - dx\mathbf{j})$$

We find that the torque only acts in the $\mathbf{k}$ direction.

$$T_n = (-\alpha \oint_{\mathcal{C}} xdx + ydy)\mathbf{k}$$

And the magnitude of the torque (T_n) takes the form of a line integral. Defining the vector field $H = x\mathbf{i} + y\mathbf{j}$, we can re-arrange the integral to take the form

$$T_n = -\alpha \oint_{\mathcal{C}} H \cdot d\mathbf{r}$$

We note that H is a conservative vector field. It follows that we can define the potential $\mathcal{Q}(x,y) = \frac{x^2}{2} + \frac{y^2}{2}$ in the region $\mathcal{S}$, such that

$$\nabla Q = H$$

Since the curve $\mathcal{C}$ is a closed loop, we find $T_n = 0$. A constant normal force applied at every point on the boundary of a 2D object produces zero net torque.

Discussion

In a simple toy model (Secton 4.2.1), we showed that chiral circular trajectories lead to an imbalance in collisions at every point along the boundary of a circular aggregate. It induced constant normal and tangential forces at every point along the boundary. We then investigated the effect of constant normal and tangential forces at every point along the boundary for 2D solid objects of arbitrary shapes. We showed that, as long as the parallel component is non zero, it results in a net torque proportional to the density of active particles and the surface area. Specifically, these results apply to any 2D object, regardless of its shape or symmetry. In contrast, we showed that normal forces applied constantly at every point of the boundary do not contribute any active torque onto an aggregate.

While the aforementioned assumptions of constant normal or tangential forces are strong, it is remarkable that they robustly produce the scaling observed in the experiment for the active torque for aggregates of arbitrary shapes and over a wide range of size [Fig. 3.2I]. An important feature of the experiment along this line, is that bacteria navigate across aggregates [Fig. 2.5C], avoiding the accumulation of bacteria in wedges that are central to the rotation of asymmetric gears [40, 41]. This could enable constant normal forces along the boundary of the aggregate, as suggested by the experimental scaling and the above derivation. Validation of this model requires further experiments, as described in Chapter 6, which lie beyond the scope of the work presented in this thesis.

4.3 Aggregation in the chiral active bath

In experiments [Fig. 3.2D-I], we observe a persistent clockwise rotation of aggregates. The following section expands upon the effects of persistent rotation (spin) on the the aggregate mass distribution (4.3.1) and the aggregate growth (4.3.2). These observations indicate that aggregation in the active bath represents a significant departure from the conventional RLCA and DLCA aggregation models.

The Smoluchoswki coagulation equation is a general master describing particle aggregation processes. Theory [52], simulations [53], and experiments [54] show that solutions to the Smoluchoswki equation, where aggregates move via diffusion and aggregate via merging and fragmentation events, lead to a universal log-normal mass distribution. This log normal distribution characterizes well our experiments for aggregation in the thermal bath [Fig. 2.2]. For aggregates in the active bath, we observe significant deviations from the log-normal distribution [Fig. 3.3B, G]; we intuit that these differences arise from aggregate spin, which modifies the laws governing aggregation.

In addition, we observe that aggregates in the active bath grow much faster than aggregates in the thermal bath [Fig. 3.1B]. This is to be expected, as aggregates in the active bath experience increased effective diffusion [Fig. 3.2C], and also spin [Fig. 3.2I]. We quantify the effects of increased diffusion and spin on aggregate growth through a mean-field growth model, and compare the model to experimental results. Our results suggest that spin makes a significant contribution to the growth rate of aggregates in the active bath.

4.3.1 Smoluchowski coagulation equation: Theory

In thermal (passive) systems of aggregation the growth dynamics of aggregates can be typically described by the Smoluchowski coagulation equation [96], which is a kinetic master equation for the formation and fragmentation probability of an aggregate or particle over time:

$$\partial_t \rho(\nu,t) = \tfrac{1}{2}\int_0^{\nu} \beta(\nu',\nu-\nu')\rho(\nu',t)\rho(\nu-\nu',t)d\nu' - \int_0^{\infty} \beta(\nu,\nu')\rho(\nu,t)\rho(\nu',t)d\nu'$$

where $\rho(\nu,t)$ denotes the size distribution function of aggregates of size (i.e. mass) ν at time t. The key quantity that determines the kinetics of aggregate sizes is then given by the collision rate $\beta(\nu_i,\nu_j)$ for the merging of two aggregates with masses ν_i and ν_j, which depends generically on the collision cross-sectional area and aggregate diffusivity [52]:

$$\beta(\nu_i,\nu_j) \propto (R_i+R_j)(D_i+D_j)\,,$$

where R_i and D_i are the radius and diffusion coefficient of the i-th aggregate, respectively. **For passive aggregation processes, such as in Brownian coagulation, the aggregate mass distribution calculated from the Smoluchowski equation attains a self-preserving, scale-invariant form, which is well-described by a log-normal distribution** [52] for the normalized aggregate mass $x \equiv m/\langle m\rangle$:

$$\rho(x) = \frac{1}{\sigma x\sqrt{2\pi}}\exp\left(-\frac{(\ln x-\mu)^2}{2\sigma^2}\right) \tag{4.2}$$

with mean μ and standard deviation σ. Interestingly, this scaling solution appears to be a universal feature in systems dominated by merging and fragmentation events, as it has been shown to describe the evolution of precursor cells and their progeny during tissue development [54], a biological process that is evidently far from equilibrium.

We find that, both in experiments and simulations, the size distribution of colloidal aggregates in the absence of the bacterial bath is remarkably well-described by a log-normal distribution [Figs. 3.3B,3.3G, black line]. Additionally, the distribution remains conserved over time [Figs. 2.1A] and depletant concentration [Figs. 2.1B]. In contrast, we observe significant deviations from this universal scaling for the active bath, where increasing activity leads to the emergence of notable tails in the distribution [Figs. 3.3B,3.3G, colored lines]. We note that even in thermal aggregation and fragmentation processes, the log-normal shape of the aggregate size distribution can only be obtained by numerically evaluating the Smoluchowski rate equation with suitable collision kernels and analytically by simplifying approximations [52]. However, for the active bath, a notable deviation from this log-normal form should be at least theoretically expected because the collision rate $\beta(v_i, v_j)$ of two aggregates is now not only controlled by the diffusion coefficient and collision diameter of the aggregates, but also by their active rotation, which effectively increases their cross-sectional area and thus leads to an increased probability for merging events. This effect, arising from the active rotation of aggregates, can be described by modifying the effective radius R or diffusion coefficient D of a aggregate, which we address below to describe the mean aggregate mass evolution over time (see section: 4.3.2). The spinning kinetics induced by bacterial density thus provides a key microscopic departure from equilibrium behavior that is reflected in the global statistics of aggregate growth.

4.3.2 Aggregate growth model

Here we provide simple dimensional arguments to estimate the dynamics of the mean aggregate mass for both the thermal and active systems. First we start by considering the thermal case and note that the rate of change of the mean aggregate mass M should generically follow

$$\frac{dM}{dt} \propto M * D * C \tag{4.3}$$

where we assume the collision rate of two aggregates to be proportional to the density of aggregates C times their diffusivity D. We can now re-write the density of aggregates as

$$C = \frac{m\phi}{Ma^2}$$

where m and a are the mass and area of a single colloid, respectively, and $\phi \equiv n_c a^2/L^2$ is the surface fraction of colloids with the number of colloids n_c and the system size L. With the Stokes-Einstein relation for the diffusion coefficient of a single aggregate $D \propto k_B T/R_g$, where R_g denotes the radius of gyration, we obtain

$$\frac{dM}{dt} \propto \frac{m\phi}{a^2}\frac{k_B T}{R_g}$$

using the scaling relationship $M/m \propto (R_g/a)^\nu$, where ν denotes the fractal dimension of a typical aggregate, we are able to rewrite the equation in terms of the average mass, M:

$$M^{1/\nu} dM \propto \left(\frac{\phi k_B T m^{(\nu+1)/\nu}}{a^3} \right) dt$$

from which, by integration we obtain:

$$\frac{M}{m} \propto \left(\frac{\phi k_B T}{a^3} t \right)^\alpha$$

with the scaling exponent $\alpha = \frac{\nu}{\nu+1}$. For the thermal case with a fractal dimension of $\nu \simeq 1.4$, this indicates that the average aggregate mass grows as $M \propto t^\alpha$ with $\alpha \simeq 0.58$, in line with the theory and simulations provided by Cerda et al. [24].

We now introduce a simple modification of the rate equation Eq. 4.3 to model aggregation in the active bath. We note that aggregates in the active bath exhibit a persistent rotation with an angular velocity that depends on the bacteria concentration [Fig. 3.2D-F]. The simplest assumption one can make for the growth dynamics of a rotating aggregate is that it would encounter and accumulate additional colloids from the bath due to its active rotation, which then increases its collision rate. At a small time interval dt, an aggregate with angular velocity Ω performs an angular displacement of $\theta = \Omega dt$, and thus sweeps an additional area of $\tilde{A} = \Omega R_g^2 dt$ as a consequence of its active motion. From a dimensional perspective, we can thus introduce an activity-dependent term $\lambda \equiv \Omega R_g^2/D$ which would effectively increase the collision rate in Eq. 4.3. The simplest form of the aggregate mass rate equation could then be given by

$$\frac{dM}{dt} \propto CDM(1+\lambda) = \frac{m\phi}{a^2} \frac{k_B T}{R_g} \left(1 + \frac{\Omega R_g^3}{k_B T} \right) \tag{4.4}$$

Next, we modify Eq. 4.4 to reflect the experimentally measured increase in effective diffusion and angular velocity with bacteria concentration. First, we introduce an effective diffusion coefficient which increases with the bacteria concentration, in line with Fig. 3.2C.

$$D_{eff} \propto \frac{k_B T}{R_g}(1+7\rho_B/\rho^*)$$

Additionally, we modify the angular velocity to reflect the experimentally obtained scaling in Fig. 3.2I.

$$\Omega \propto \frac{\rho_B}{\rho^*} M^{\frac{\nu-3}{\nu}}$$

Thus, we obtain the equation determining the rate of growth of an aggregate as a function of the bacteria concentration:

$$\frac{dM}{dt} \propto \mathcal{A}(1+7\rho_B/\rho^*)M^{-1/\nu}\left(1+\mathcal{B}M\frac{\rho_B/\rho^*}{1+7\rho_B/\rho^*}\right) \tag{4.5}$$

with the prefactors $\mathcal{A}$ and $\mathcal{B}$ controlling the relative strength of diffusion and angular velocity, respectively.

In Fig. 4.4A, we plot the mean aggregate mass at increasing bacteria concentrations for the 4-hour aggregation experiments. The experimental data shows a rapid increase in growth rate at low and intermediate bacteria concentrations. At the highest bacteria concentrations, however, the growth rate saturates, as evidenced by the crossing orange ($\rho_B = 0.5\rho^*$) and red ($\rho_B = \rho^*$) curves. Our simulations show a similar saturation in aggregate growth, due to the deformation and compaction of spinning aggregates [Fig. 3.4C, 3.4D]. This saturation is not captured by the present aggregation model, built upon collisions of objects. In the present model, rotation and collision rates increase with increasing bacteria concentration, leading to monotonic growth of the aggregates.

Next, we numerically integrate Eq. 4.5, and compare the solutions to the experimental data [Fig. 4.4A]. To determine $\mathcal{A}$, we numerically solve Eq. 4.5 using the parameters $\rho_B = 0$, $\nu = 1.4$, and the initial condition that the numerical solution matches the experimental data at the first time step (time = 10 minutes). We fit this numerical solution to the experimental data, and find good agreement for $\mathcal{A} = 1.6$ [Fig. 4.4B - inset]. To model aggregation in the active bath, we keep $\mathcal{A}$ fixed and use the experimentally measured values of ρ_B [Fig. 2.6], and the fractal dimension $\nu(\rho_B)$ [Fig. 5.3].

In Fig. 4.4B, we plot solutions to Eq. 4.5 at increasing bacteria concentrations, using the coefficients $\mathcal{A} = 1.6$ and $\mathcal{B} = 0$. In doing so, we increase diffusion proportional to the experimentally measured value, but keep the angular velocity at zero. By comparing to the experimental data in Fig. 4.4A, we see that this model systematically underestimates the growth rate of aggregates observed in the experiment. In Fig. 4.4C, we add the effect of rotation to the aggregation model, with the coefficient $\mathcal{B} = 0.15$, thus allowing both diffusion and angular velocity to scale with increasing activity of the bath. **We find that the addition of rotation allows the model to predict a growth comparatively closer to the experiment**. Two comments are in order. First, solutions to Eq. 4.5 diverge at long times, an effect of the linear increase in collision rate added from the rotation; this is non-physical, as the effect should eventually saturate at high rotation rates, and represents a limitation of our model. Additionally, we note that the non-linear equation Eq. 4.5 did not allow us to extract a simple relationship between time and activity.

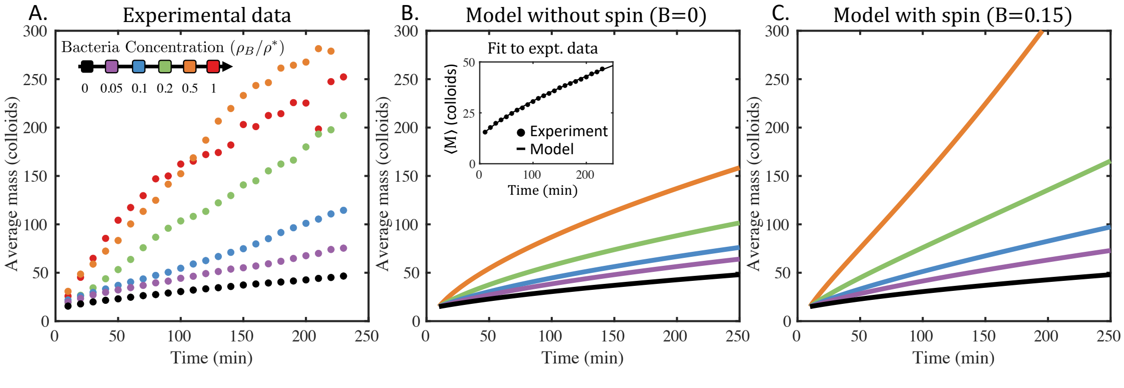

Figure 4.4. **(A)** Average aggregate mass over the 4-hour aggregation experiments. Different colors indicate different bacteria concentrations (see legend). **(B)** Numerical solutions to Eq. 4.5, using the parameters $\mathcal{A} = 1.6$ and $\mathcal{B} = 0$. Different colors represent different bacteria concentrations ρ_B, following the same colorscheme decribed in the legend of Fig S11A. **(B-Inset)** Parameter $\mathcal{A}$ is determined by fitting the experimental data for $\rho_B = 0$ to the numerical solution to Eq. 4.5; we find a good fit for $\mathcal{A} = 1.6$ **(C)** Numerical solutions to Eq. 4.5, using the parameters $\mathcal{A} = 1.6$ and $\mathcal{B} = .15$. Different colors represent different bacteria concentrations ρ_B, following the same colorscheme decribed in the legend of Fig. 4.4A.

Chapter 4, in part, contains material as it may appear in Nature Physics, 2023. Daniel Grober, Ivan Palaia, Mehmet Can Ucar, Edouard Hannezo, Anđela Šarić, Jérémie Palacci. The dissertation author was the primary investigator and author of this paper.

Chapter 5

Technical points of data processing and simulations

In the following Chapter, we discuss the more technical aspects of Chapter 3. The first section discusses data processing techniques used to analyze the morphology of aggregates. The following section includes supplemental text describing the simulations. Finally, we include full descriptions of the supplemental movies described in Chapter 3.

5.1 Technical data processing techniques

5.1.1 Aggregate tracking

To study the dynamics of colloidal aggregates, we develop tracking software in MATLAB. In each frame, we extract the center of mass, surface area, and perimeter of each aggregate from the binary image. Additionally, for aggregates where the major axis is significantly greater than the minor axis, we can reliably track their orientation by taking the angle between the major axis and the horizontal. Aggregates can be linked from one frame to the next by searching the vicinity of their previous center of mass for an aggregate of similar shape and size; when a match cannot be found, we assume a collision has occurred and treat it as a novel particle. In this way, we are able to create a 2D trajectory for each aggregate.

To extract information about the diffusion and rotational diffusion of aggregates, we apply the aggregate tracking software to the videos taken in the short-time dynamics experiments. Using the trajectories obtained from aggregate tracking, we calculate a Mean Squared Displacement (MSD) and Mean Squared Angular Displacement (MSAD) up to $\Delta t = 5s$ using a sliding window. To improve the statistics of the MSD and MSAD, we only consider trajectories longer than 1500 frames. For each particle, a diffusion coefficient, or rotational diffusion coefficient, is extracted from a linear fit between time and MSD, or MSAD [Fig. 3.2A inset, Fig 3.2B inset]. These coefficients are binned by size R_G; the averages and standard deviations of these bins are reported in Fig 3.2A and Fig 3.2B; each bin contains more than 5 aggregates. For each bacteria concentration in Fig 3.2A, we track more than 90 total aggregates; for each bacteria concentration in Fig 3.2B, we track more than 50 total aggregates.

Similarly, we extract information of the angular velocity by tracking the aggregates observed in the long-time dynamics experiments. Angular velocity is obtained through a linear fit between the aggregate orientation and time [Fig 3.2D]. Each point in Fig 3.2I corresponds to a single aggregate.

5.1.2 Aggregate comparison

To compare the morphology of aggregates assembled in the active and thermal baths, the most basic thing would be to look at aggregates at the end of the experiments. Below, we observe aggregates in the active bath at various bacteria concentrations after 4 hours. In the thermal bath, experiments are extended to 40 hours. We observe that aggregates formed in the active bath at the highest bacteria concentrations are largest after 4 hours, and get smaller with decreasing bacteria concentration.

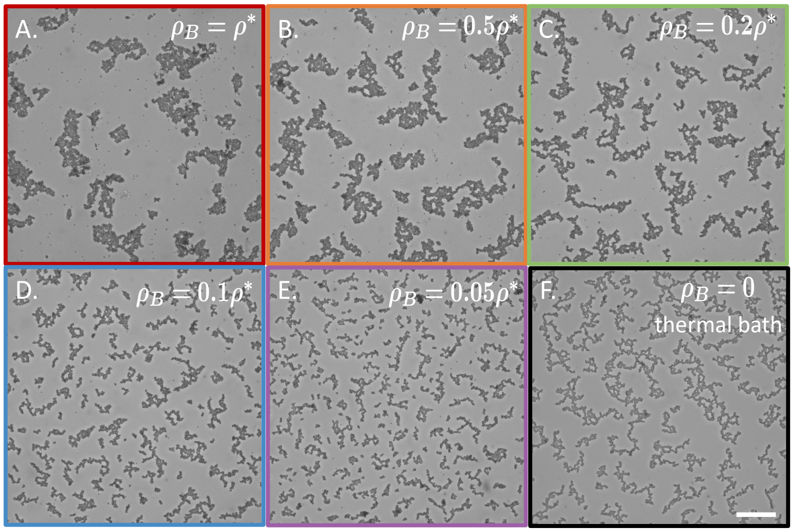

Figure 5.1. **(A-E)** Aggregates formed in the active bath after 4 hours, labeled with the corresponding bacteria concentration. **(F)** Aggregates formed in the thermal bath after 40 hours. The scale bar is 100um. Same scale for all.

5.1.3 Compare aggregates with same average mass

This comparison can be improved upon by finding the frame where the average mass of the aggregates is equivalent. In Fig. 5.2, we compare aggregates formed in the thermal bath ($\rho_B = 0$) after 25 hours with aggregates formed in the highest activity bath ($\rho_B = \rho^*$) after 1.25 hours. In both cases, the average aggregate mass is 150 colloids. We observe aggregates in the thermal bath form ramified, branched structures. Aggregates in the active bath form compact structures.

5.1.4 Fractal dimension in chiral bacterial bath

The qualitative observations made in the previous section can be expanded upon by computing the fractal dimension of the aggregates as a function of time. Following the procedure described in Section 2.1.1, we compute the fractal dimension in each frame at 5 positions along the capillary, every 10 minutes for 4 hours. In Fig. 5.3 we display the average as a function of time; the error bars represent the standard deviation of this measurement across 5 positions. We observe that the fractal dimension reaches a steady state value after about 2 hours. The steady state fractal dimension increases with increasing bacteria concentration.

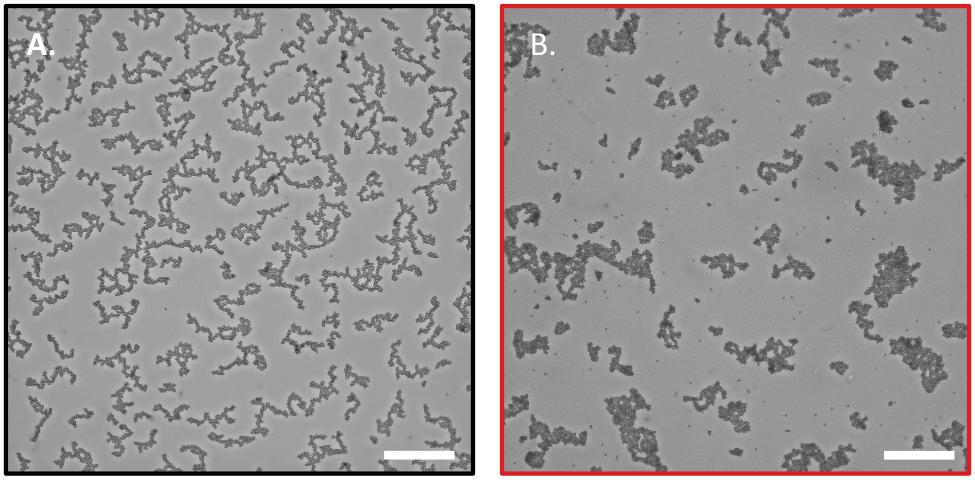

Figure 5.2. **(A)** Aggregates formed in the thermal bath ($\rho_B = 0$) after 25 hours. **(B)** Aggregates formed in the highest activity bath ($\rho_B = \rho^*$) after 1.25 hours. In both cases, the average aggregate mass is 150 colloids and the scale bar indicates 100 µm

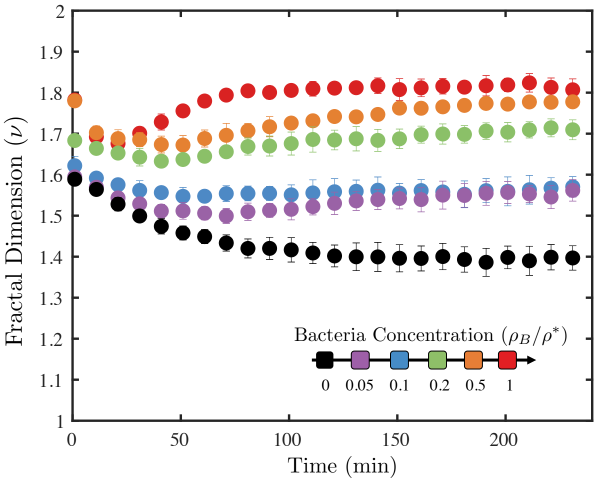

Figure 5.3. Fractal dimension as a function of time, for aggregates formed in various active baths. The bacteria concentrations are: $\rho_B = \rho^*$ (red) , $\rho_B = 0.5\rho^*$ (orange) , $\rho_B = 0.2\rho^*$ (green), $\rho_B = 0.1\rho^*$ (blue), $\rho_B = 0.05\rho^*$ (purple), and $\rho_B = 0$ (black)

5.1.5 Fraction of colloids on the boundary

We further quantify the morphology of the colloidal aggregates by analyzing the fraction of colloids on the boundary. Before we can analyze the fraction of colloids on the boundary of each aggregate, we must estimate the total number of colloids and the number of colloids on the boundary.

The number of colloids on the boundary is estimated from the perimeter of the binary region. The length of the perimeter is calculated from the sum of the Euclidean distances between each pair of neighboring pixels on the boundary of the binary region, including both interior and exterior boundaries. We estimate the number of colloids on the boundary as the total perimeter divided by the colloid diameter. Next, we estimate the total number of colloids to be the number of pixels in the binary region divided by the area of the Wigner-Seitz primitive cell for a hexagonal lattice with nearest neighbor distance equal to the diameter of a colloid. To verify these estimates, we perform a case study on a handful of small aggregates where it is possible to count the number of colloids manually [Fig. 5.4A]. We find good agreement between the estimated value and the exact value for both the number of colloids on the boundary and the total number of colloids in an aggregate [Fig. 5.4B and 5.4C]. The fraction of colloids on the boundary, presented in Fig. 5.5, is the ratio of the estimated number of colloids on the boundary and the estimated total number of colloids.

In Fig. 5.5, we compare the fraction of colloids on the boundary of aggregates assembled in four different active baths, corresponding to $\rho_B = \rho^*, \rho_B = 0.5\rho^*, \rho_B = 0.2\rho^*$, and, $\rho_B = 0$. To maintain consistency, we analyze frames where the average aggregate mass is equal to 150 colloids. We find that the fraction of colloids on the boundary decreases with increasing bacteria concentration.

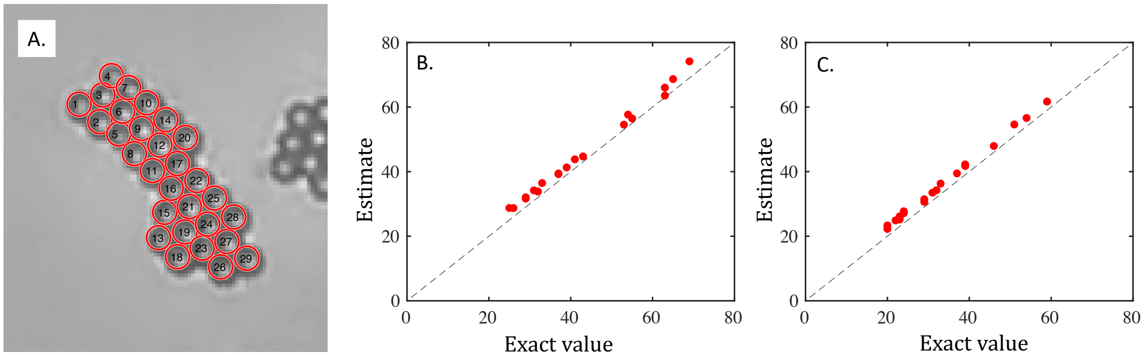

Figure 5.4. (A) Example of an aggregate where each colloid has been identified and labeled. The total number of colloids and number of colloids on the perimeter are counted manually. (B) The number of colloids on the perimeter, estimated from the perimeter of the binary region, compared with the exact value. (C) The total number of colloids in a cluster, estimated from the area of the binary region, compared with the exact value.

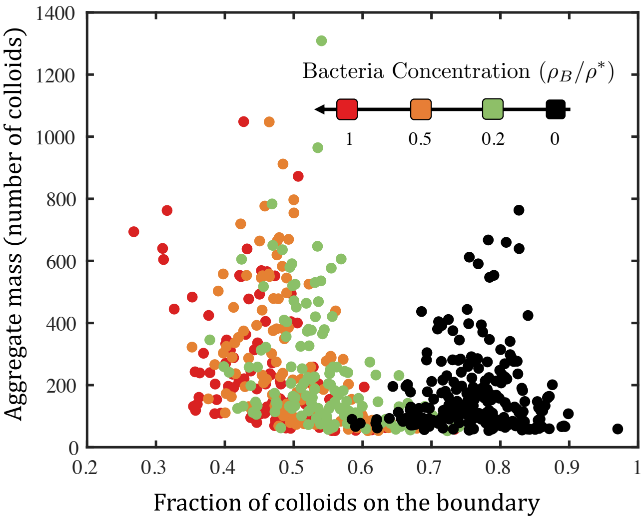

Figure 5.5. Fraction of colloids on the boundary for aggregates formed in various bacterial baths, estimated using the perimeter (interior and exterior) and area of the binary region. The bacteria concentrations are: $\rho_B = \rho^*$ (red) , $\rho_B = 0.5\rho^*$ (orange) , $\rho_B = 0.2\rho^*$ (green), and $\rho_B = 0$ (black).

5.1.6 Number fluctuations

Number fluctuations are calculated by dividing the binarized image into as many independent boxes of area n as possible. We define N to be the sum of the pixels values (0 or 1) within a box of size n. For each box size, we calculate an average $\langle N \rangle$ and the variance $\sigma^2(N)$. In Fig. 3.6C and Fig. 3.6G, we display $\sigma^2(N)/\langle N \rangle$ as a function of $\langle N \rangle$. As the size of the box increases (i.e. for large $\langle N \rangle$), the number of realizations decreases; this is reflected in the error bars in Fig. 3.6C and Fig. 3.6G.

5.2 Simulation details

5.2.1 Computational model

In our computational model, colloids are modeled as two-dimensional particles, similarly to [97]. They interact through a sum of a repulsive interaction, enforcing volume exclusion, and an attractive interaction, representing the depletion force from experiments. The repulsive interaction is obtained through a Weeks-Chandler-Anderson potential (first line in the equation below), while attraction is obtained by a simple cosine-squared potential (second line):

$$U_\mathrm{c}(R) = \begin{cases} \varepsilon_\mathrm{c}\left[\left(\frac{\sigma}{R}\right)^{12} - 2\left(\frac{\sigma}{R}\right)^{6}\right] & \text{if } R < \sigma \\ -\varepsilon_\mathrm{c}\cos^2\left(\frac{\pi(R-\sigma)}{2r_\mathrm{a}}\right) & \text{if } \sigma < R < \sigma + r_\mathrm{a} \\ 0 & \text{if } R \geq \sigma + r_\mathrm{a} \end{cases} \cdot \tag{5.1}$$

Here, ε_c is the attraction strength, σ is the particle diameter, R is the distance between the centers of the two particles, and r_a is the range of attraction. We choose $\varepsilon_\mathrm{c} = 20\,k_\mathrm{B}T$ and $r_\mathrm{a} = 0.15\,\sigma$: these values correspond to a slightly softer potential than the one estimated for experiments, but, while still representing a strong short-range interaction and leaving the physics unchanged, they make simulations much more efficient and allow to simulate longer times.

To be able to define an angular velocity for the particles, and for the particles to be able to exchange angular momentum, we introduce some friction along the surface of the particles (see for instance [79]). We do so by coating each particle with 5 patches, positioned at distance $0.5\,\sigma$ from the particle center and equally spaced on the circumference (see Fig. S13). The number of patches, 5, was chosen so as to avoid any fictitious source of crystalline symmetry (namely, triangular symmetry with 3 patches, square with 4, or hexagonal with 6). Friction takes the form of a patch-patch interaction, that we chose to be mildly repulsive and of cosine-squared shape:

$$U_{\mathrm{p}}(r) = \begin{cases} \varepsilon_{\mathrm{p}} \cos^2\left(\dfrac{\pi}{2}\dfrac{r}{r_{\mathrm{p}}}\right) & \text{if } r < r_{\mathrm{p}} \\ 0 & \text{if } r \geq r_{\mathrm{p}} \end{cases} . \tag{5.2}$$

Here, $\varepsilon_{\mathrm{p}} = 10\,k_{\mathrm{B}}T$ is the patch-patch repulsion strength, r is the distance between two patches, and $r_{\mathrm{p}} = r_{\mathrm{a}} = 0.15\,\sigma$ is the patch-patch interaction range. Note that when two patches superimpose, the interaction energy between two colloids can stay negative as $\varepsilon_{\mathrm{c}} \gg \varepsilon_{\mathrm{p}}$. Patches move rigidly with the colloid they are attached to. This is ensured, at each time step, by summing the the forces acting on the central particle and on the 5 patches of the rigid body to obtain a force acting on their center of mass and a torque relative to their center of mass.

If the whole colloid has mass m, the central particle has mass $0.6\,m$ and each of the 5 patches has mass $0.08\,m$. This makes the moment of inertia of the colloid equal to that of a sphere, namely $\frac{2}{5}m(\frac{\sigma}{2})^2$.

Colloids are made spin by applying to each of them independently a torque of magnitude τ, between 0 and $15\,k_{\mathrm{B}}T$. The torque results from a pair of forces of constant magnitude $f = \tau/(0.5\,\sigma)$; one applied to the center of the colloid and one to one of the patches, as shown in Fig. 5.6A. Fig. 5.6B shows all the forces applied to two colloids at contact (excluding thermal noise, discussed below).

5.2.2 Simulation details

At the beginning of each simulation, particles are positioned at random sites of a square lattice, defined such that the surface density of colloids is the desired one. The initial orientation of particles is also randomized.

Two-dimensional molecular dynamics simulations are run in LAMMPS [98] and visualised with OVITO [99]. A velocity-Verlet integrator is coupled with a Langevin thermostat, mimicking an implicit solvent, so that the system is effectively in the NVT ensemble. The

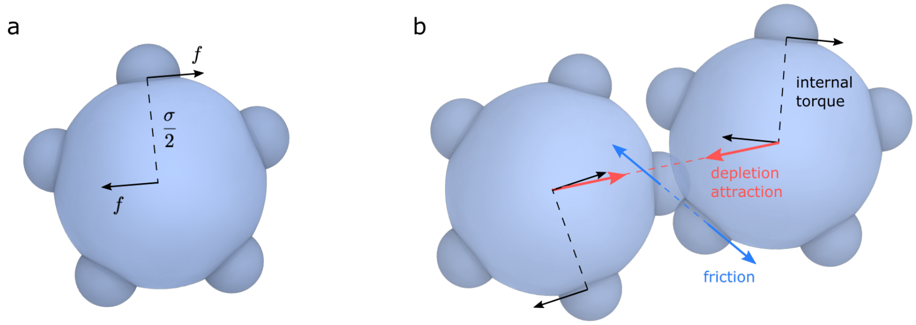

Figure 5.6. **(a)** Sketch of a colloid within our computational model. The 5 patches are rigidly attached to the central body. Their size represents the repulsion range $r_p = 0.15\,\sigma$. In black, the forces responsible for the active torque. **(b)** Two colloids interacting through central interactions (Eq. 3, in red) and patch-patch friction (Eq. 4, in blue). Those eventually result in an almost-rigid rotation of the two-body complex about their center of mass.

time step chosen for the integration of the 2D equations of motion is $\tau_s = 0.008\,\tau_0$, where $\tau_0 = \sqrt{m\sigma^2/(k_B T)}$ is the simulation unit of time. The Langevin thermostat has a friction coefficient $\gamma = 0.08\,m/\tau_0$, meaning that the momentum of a particle relaxes on a scale of the order of 10 time steps. Such fast relaxation brings simulations close to the fully Brownian regime and favors computational stability.

Simulations of folding aggregates (Figs. 3.3D, 3.3E, 3.3F, 3.3G, 3.4B, 3.4C, 3.4E, 3.4F, 3.5A, 3.4B and Movies S3-S6) containing $N = 10000$ colloids were run in a square box with periodic boundary conditions, applied along both Cartesian directions. For surface density $\rho = 0.20\,\sigma^{-2}$, corresponding to a packing fraction $\phi = \rho \cdot \pi(\sigma/2)^2 \simeq 0.16$, 16 realizations per torque value, differing by the random number generator seed, were run for $5 \cdot 10^6$ time steps τ_s. Fig. 3.3D and 3.3E are screenshots taken at times $8 \cdot 10^3$ and $1 \cdot 10^5\,\tau_s$. Figs. 3.3F and 3.3G refer to time $3 \cdot 10^4\,\tau_s$, chosen so as to match approximately the sizes of the aggregates seen in the experimental time range. The folding dynamics is best described by Movies S5 and S6 and by Fig. 5.7. The clusters for Fig. 3.5B were extracted from all the 16 mentioned realizations, at the end of the simulation time; at least 40 clusters per torque value were analyzed, as detailed in the section ”Porosity” below.

Longer simulations were needed to fill the phase diagram of Fig. 3.5A, to ensure that at long times aggregates did not aggregate into percolating structures or, vice versa, that percolated structures did not break down into isolated aggregates: for each value of packing fraction shown (corresponding to density 0.10, 0.15, 0.20, 0.25, 0.40, 0.50 and 0.60 σ^{-2}), 2 different realizations were run for times between 2 and $9 \cdot 10^7\, \tau_s$ (the largest times being needed for low densities or when close to the transition).

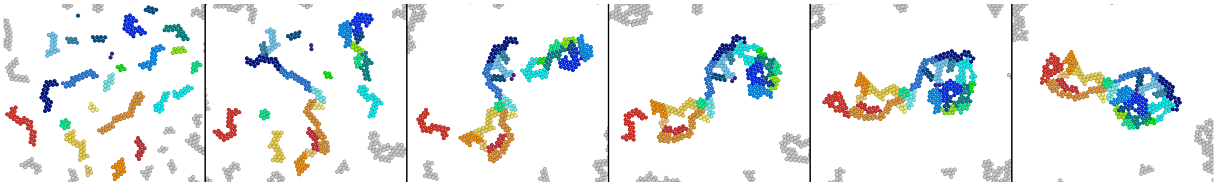

Figure 5.7. Aggregation and folding of an aggregate in simulations, with an internal torque of $10\, k_{\mathrm{B}}T$. Snapshots are taken at equally spaced times between 1 and $6 \cdot 10^4$ time steps τ_s.

Simulations of non-folding aggregates (Figs. 3.4D, 3.4G, 3.4H) were performed running a clustering algorithm every 100 time steps and freezing aggregates, so that once a new particle binds it moves rigidly with the rest of the aggregate. The cutoff distance for the clustering algorithm was $R = \sigma + r_{\mathrm{a}} = 1.15\, \sigma$, corresponding to the interaction range. Within our setup, this procedure was incompatible with periodic boundary conditions in LAMMPS. As a consequence, simulations were run in a box delimited by an impenetrable wall, modeled by a purely-repulsive 6-12 Lennard-Jones interaction, with parameters $20\, k_{\mathrm{B}}T$ and $1\, \sigma$, cut and shifted at its minimum. The number of colloids was however increased to $N = 100000$ to reduce the effect of hard boundaries, which was checked for with the aid of additional simulations with $N = 20000$ only, as shown in Fig. **??**. In addition, data was discarded when the mass of the largest aggregate went beyond 10% of the total mass in the system.

Finally, inhibiting folding necessarily means forbidding particles from rolling on each other upon binding, akin to velcro-coated colloids. This makes the branches of the aggregate look thinner (1 colloid thick) than in the folding case (2 colloid thick), as shown by a comparison between Figs. 3.4G and 3.4E. To correct for the fact that comparable structures are now formed with only half of the mass, surface density was reduced to $\rho = 0.10\, \sigma^{-2}$.

Stress-strain tests (Fig. 3.5C and Movies S7, S8) were run on gelled configuration taken from folding-aggregates simulations at density $\rho = 0.40\,\sigma^{-2}$ (i.e. $\phi = 0.31$), $N = 10000$ and time $1 \cdot 10^7\,\tau_s$. At such value of density, the system is in the gel phase for a wide range of activities, allowing us to compare gels prepared in very different conditions ($\tau = 0$, 1 and $3\,k_\mathrm{B}T$). The initial box size is $L_x = L_y = \sqrt{N/\rho} \simeq 158\,\sigma$. We stretch or compress it by $2\,\sigma$ at a time, in $10^5\,\tau_s$, then let the system equilibrate for $3 \cdot 10^5\,\tau_s$, and then average the measured stress tensor for $1 \cdot 10^5\,\tau_s$. We repeat this for 20 iterations, until a final strain of $40\,\sigma$ (i.e. 24%). For each value of internal torque used to prepare the initial gels, we use 3 different gel networks, deformed both along x and y, with 4 different seeds, so that each point shown in Fig. 5C is an average of 24 measures. The deformation runs are performed at no activity.

Data analysis

We run a **cluster analysis** and compute **gyration radii** through OVITO [99]. Two colloidal particles are considered in the same aggregate if their centers are within attraction range ($R < \sigma + r_\mathrm{a} = 1.15\,\sigma$).

Fractal dimension

The **fractal dimension** ν is computed by fitting masses M and gyration radii R_g to the scaling law $M \sim R_\mathrm{g}^\nu$, as shown in Fig. 3F. When computing R_g, we assume colloidal particles to be point-like, with (unit) mass concentrated at their center. For the inset of Fig. 3.5A, we compute ν from the last 4 time frames of the simulations when the phase is cluster-like, and from the last 4 time frames before percolation when the phase is gel-like. We then fit the boundary between the two phases in the (ν, ϕ) space to the curve $\nu = 2 + \alpha \log(\phi)$ and find $\alpha \simeq 0.29$, as described in the main text.

Porosity

Porosity of a material is defined as the area of the holes divided by the total area (area of solid material plus area of holes). We calculate the total area of an aggregate by applying the flood-fill operation to a binarized image of the aggregate; total area is the number of pixels in the binary region after the flood - fill operation. Area of the holes is calculated as the difference between total area and area of the binarized image.

5.3 Description of movies

Movie S1: (Experiment) Comparison of aggregation in thermal versus active baths. Sticky colloids aggregate in either a thermal (ρ_B=0) or active bath of swimming *E. coli* ($\rho_B = 0.5\rho^*$) - all other parameters being equal (same concentration of colloids, strength of attraction by depletion, objective and speed of acquisition). The field of view in each video is 650 x 650 µm. The dynamics appear much faster in the active bath than the thermal bath, and the morphology of the aggregates differ. Real time of the movie is 4h.

Movie S2: (Experiment) Persistent clockwise rotation of aggregates in the active bath. An accelerated video of sticky colloids in the active bath of swimming *E. coli* ($\rho_B = \rho^*$) , which highlights the persistent clockwise motion of the aggregates. Real time of the movie is 2h.

Movie S3: (Simulation) Conventional aggregation in a thermal bath. Simulated aggregation of colloids with no internal activity (the internal torque for each particle is set to $0\,k_\mathrm{B}T$). The playback speed increases twice during the movie, at times 10000 and 50000, in order to capture both the formation of small aggregates at short times and the formation of large structures and gelification, occurring on long time scales. The time of each frame is indicated in the top right corner. Packing fraction $\Phi = 0.16$.

Movie S4: (Simulation) Aggregation at low activity. The internal torque for each particle is set to $1\,k_\mathrm{B}T$. Rotation and partial folding of the aggregates arise, resulting in faster and morphologically different aggregation, compared to the thermal case. The system percolates and forms a space-spanning network at large times. The playback speed increases twice during the movie, at times 10000 and 50000, in order to capture both the formation of small aggregates at short times and the formation of large structures and gelification, occurring on long time scales. The time of each frame is indicated in the top right corner. Packing fraction $\Phi = 0.16$.

Movie S5: (Simulation) Aggregation at high activity. The internal torque for each particle is set to $10\,k_\mathrm{B}T$. Rotation and folding of the aggregates arise, resulting in faster and morphologically different aggregation, compared to the thermal case. The system does not percolate and the gel phase is replaced by compact clusters. The playback speed increases twice during the movie, at times 10000 and 50000, in order to capture both the formation of small aggregates at short times and the dynamics on long time scales. The time of each frame is indicated in the top right corner. Packing fraction $\Phi = 0.16$.

Movie S6: (Simulation) Zoomed in view of aggregation and folding at high activity. A subsection of the simulation window, focusing on the non-conventional aggregation of particles; the rotation and folding leads to the formation of a compact cluster (the internal torque for each particle is set to $10\,k_\mathrm{B}T$). The playback speed is constant, and the time of each frame is indicated in the top right corner. Packing fraction $\Phi = 0.16$.

Movie S7 (Simulation) Mechanical test of a gel assembled in thermal conditions. The gel was previously assembled with the internal torque for each particle is set to $0\,k_\mathrm{B}T$, [see SI], and the internal torque remains at $0\,k_\mathrm{B}T$ during the stretching experiment. The strain increases with time, and the exact value is indicated in the top right. The gel exhibits an elastic response in the considered regime of strain [see Main Text].

Movie S8 (Simulation) Mechanical test of a gel assembled in active conditions. The gel is previously assembled in active conditions (the internal torque for each particle is set to $3\,k_\mathrm{B}T$), and the internal torque is set to $0\,k_\mathrm{B}T$ during the stretching experiment. The strain increases with time, and the exact value is indicated in the top right. The aggregation in active conditions results in a gel with unconventional structure, as compared with the gel assembled in thermal conditions (Movie S7); this results in a non-linear mechanical response, akin to a mechanical diode.

Chapter 5, in part, contains material as it may appear in Nature Physics, 2023. Daniel Grober, Ivan Palaia, Mehmet Can Ucar, Edouard Hannezo, Anđela Šarić, Jérémie Palacci. The dissertation author was the primary investigator and author of this paper.

Chapter 6

Outlooks and Perspective

In the following chapter, we summarize the main findings of this thesis, and reflect upon where we stand with respect to the initial vision of this work. We conclude this thesis by proposing three experiments which constitute future directions for the project.

In Chapter 3, we showed that an active bath of motile *E. coli* directs the assembly sticky colloids into structures which are not possible with conventional assembly in a thermal bath. Through the assistance of simulations, we showed that the persistent clockwise rotation of aggregates is the salient feature that drives their non-conventional aggregation. Crucially, Fig. 3.5A establishes the activity of the bath as a lever of control over the phase diagram of colloidal aggregates. This constitutes a proof of concept of the initial vision of this thesis: active matter is capable of re-shaping the structure of soft materials from within. We view this work as an important first step, although more experiments are needed to develop a material with dynamic material properties that are tuned by active matter from within.

Chapter 4 discusses further the interactions between colloidal aggregates and motile *E. coli*, focusing on a mechanism to describe the observed persistent rotation of aggregates. Through additional experiments on an inverted droplet, which reverses the chirality of the *E. coli* trajectory, we determined that the rotation of aggregates is correlated with the direction of the *E. coli* trajectories [Fig. 4.1]. Experiments utilizing GFP fluorescent *E. coli* show that the bacterium collide with the aggregate, and then swim through [Fig. 2.5C]. Based on these observations, we propose a collision based model where the chirality of the swimmer trajectories leads to an imbalance in collisions along the perimeter, resulting in a force acting parallel to the perimeter (see: Section 4.2.1). For a constant force per unit length applied along the perimeter of the aggregate, the resulting applied torque is proportional to the surface area of the aggregate, an important feature of the experimental measurements [Fig. 3.2I]. Further experiments to unambiguously test the validity this model are outlined in Section 6.1.

From the outset, this thesis envisions leveraging active matter to sculpt the structure of soft materials from within. Through experimental work we have proved that this vision is possible, and laid the groundwork for the development of a new class of materials powered by active matter. During the course of this research, new questions and opportunities have arisen which need to be developed through further experimentation. Section 6.1, outlines future experiments to determine a physical mechanism for the observed persistent clockwise rotation of aggregates. Section 6.2 outlines the use of light-powered *E. coli* to create a spatially (and temporally) heterogeneous active bath and its application to create novel 2D colloidal gels. Section 6.3 proposes to create a spatially and temporally heterogeneous active bath using a microfluidic device to vary the concentration of L-serine in the suspension.

6.1 Mechanism of aggregate rotation

Chapter 4 proposes a model for the persistent clockwise rotation of aggregates, as observed in experiments. The proposed model states that the rotation arises from a force applied along the perimeter of each aggregate, originating from collisions between the *E. coli* and aggregates. This model faithfully accounts for many of the salient features of the experimental observations, namely the scaling that the applied torque is proportional to the concentration of bacteria times the surface area of the aggregate [Fig. 3.2I]. Notably, this model neglects the contribution of *E. coli* as they swim through the aggregate. The question of whether the applied torque arises from collisions with the perimeter of the aggregate, or while *E. coli* swim inside the aggregate, remains unanswered. Further experiments are required to validate this toy model, and unambiguously determine a physical mechanism for the rotation of aggregates.

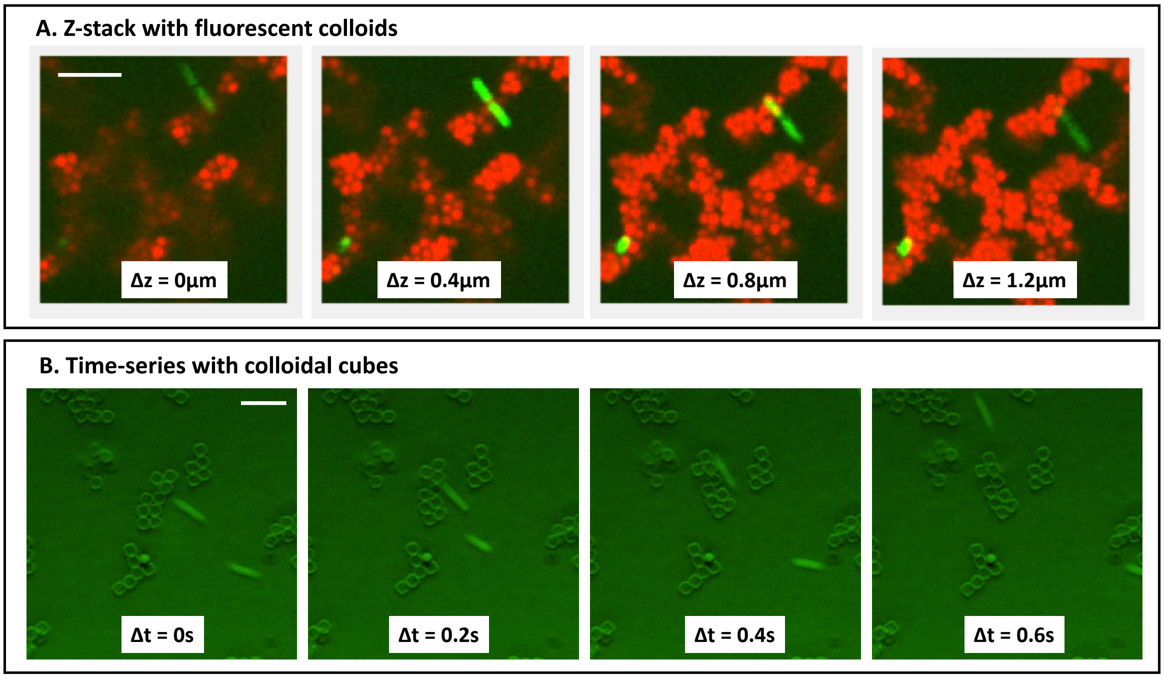

Figure 6.1. **(A)** Z-stack of GFP labeled *E. coli* swimming through aggregates of polystyrene colloids. The *E. coli* swim between the colloids and the glass substrate. *(B)* Preliminary experiments studying aggregation of cubic colloids in a bacterial bath. The *E. coli* cannot penetrate into the aggregate of colloidal cubes, but scatter off the exterior.

As evidenced by Fig. 2.5C, the *E. coli* swim through the colloidal aggregates. Preliminary experiments with fluorescent polystyrene colloids [Fig. 6.1A] indicate that the *E. coli* are between the glass substrate and the layer of colloids. These results are in line with [66], who find that *E. coli* can navigate a crystal of 10μm colloids, swimming in straight trajectories through the space between the glass coverslip and the spherical colloids. To separate the contribution of the torque from bacteria colliding with the exterior, as discussed in the toy model, from the torque of bacteria while penetrating the interior of the aggregate, we propose experiments which inhibit *E. coli* from entering the aggregate.

One method to inhibit *E. coli* from entering the aggregate is to use colloidal cubes, thus minimizing the empty space between the spheres and the substrate. Fig. 6.1B displays preliminary experiments using aggregates of 1μm cubic colloids. The time-series shows an incident *E. coli* colliding with a small aggregate of cubes; the kinetics appear much different from aggregates of 2µm spheres, as the bacterium scatters off the perimeter aggregate rather than penetrate inside. Further experimental design is required to grow aggregates large enough such that their dynamics can be compared with the aggregates in [Fig. 3.2I].

Another method to inhibit *E. coli* from entering the object would be to 3D print a solid, micron-scale object. One example would be a cylinder of radius 50 µm and height 5 µm with a small defect such that the rotation can be tracked. Another interesting shape is a hollow cylinder of similar size, such that we are sure there are no *E. coli* swimming above or below the interior of the object. Such microprinted object can be achieved using the UpNano 3D printer, recently acquired by IST Austria. A 3D printed object would allow us to track the rotation for long periods of time, as the object cannot deform or change shape - a persistent issue with tracking colloidal aggregates. Previous work [40, 41] showed that 3D printed objects with a ratcheted exterior rotate in an active bath of *E. coli* bacteria. Di Leonardo et al. noted that on a solid - liquid interface, all geared objects (symmetric or asymmetric) rotate with a clockwise rotation, and postulated that the mechanism had to do with the bacteria's clockwise trajectories [40]. The proposed experiments would could build upon their findings, and could elucidate a new mechanism of rotation for objects in a chiral active bath.

6.2 Spatio-temporal control of active bath using green light powered bacteria

Chapter 3 established the activity of the bath as a lever of control over the phase diagram of aggregation. All of the experiments presented thus far take place at constant *E. coli* concentration and swimming speed. In future work, we want to dynamically vary the activity of the bath (by modulating the speed of the *E. coli*), in both space and time. The following section envisions the use of green-light powered bacteria to achieve this goal.

Previous work [44, 43] has successfully made green-light powered *E. coli* by genetically modifying cells to express Proteorhodopsin (PR). PR is a light mediated ion channel which opens and accepts H^+ into the cell in the presence of green light. Recall that the the *E. coli* flagella is powered by the protomotive force, pumping H^+ out of the cell and across the charged cell membrane. This process requires an electron acceptor inside the cell - in the absence of external nutrients, cells typically use O_2 [27]. In anerobic conditions (without O_2), cells require an alternative electron acceptor for the flagellar motor to function properly (typically these are biproducts from metabolizing external nutrients, such as glucose). In the presence of green light, Proteorhodopsin enables the flagellar motor to function in anerobic conditions.

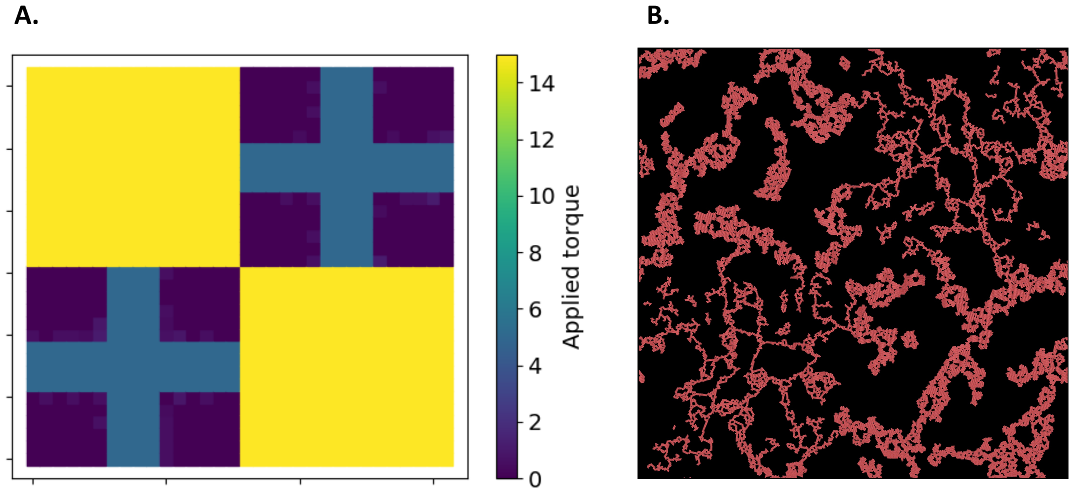

Figure 6.2. **(A)** Inhomogenous checkerboard activity pattern. **(B)** Colloidal gel assembled in the checkerboard activity pattern described in A. Regions assembled in high activity are dense. The dense regions are sewn together by branched structures assembled at lower activities.

We envision combining a pattern of green light and green-light powered bacteria to create a spatially and temporally heterogeneous active bath. We will leverage this technique to grow a 2D colloidal gel, where certain sections of the gel are aggregated thermal baths (passive), while other are aggregated in active baths where the activity is modulated in space and time. In sections where the light is strong, colloids will aggregate via the chiral aggregation mechanism described in Chapter 3, forming compact structures. Meanwhile, other parts can be formed via thermal aggregation, forming branched space spanning networks.

To test this idea, we leveraged the simulations of sticky rotors presented in Chapter 3, which previously showed consistent agreement our experiments. Preliminary simulations by Lucas Floquet and Ivan Palaia using a checkerboard pattern of activity [Fig. 6.2A] show promising results. The gel contains highly dense regions, where colloids are assembled at high activity; the dense regions are sewn together by branched structures assembled at lower activities [Fig. 6.2B]. The resulting structure is highly heterogeneous, and we expect it to exhibit novel material properties.

6.3 Spatio-temporal control of active bath by varying L-serine concentration

This section envisions the use of a microfluidic device to dynamically vary the concentration of L-serine in the active bath. Preliminary experiments show the addition of 1mM L-serine, rather than Glucose, causes *E. coli* to swim for approximately 45 minutes and then abruptly stop swimming [Fig. 6.3A]. In effect, this creates a chemical “on” and “off” switch for the activity of the bath.

We perform aggregation experiments at low binding (0.8 g/L PEO, $\Delta E \sim 18 k_{\mathrm{B}} T$), in a bacterial bath with 1mM L-serine. Under these conditions, we observe that aggregation is inhibited while the activity is on, with small aggregates dynamically forming and fracturing [Fig. 6.3B,C,D]. After the activity is turned off, large aggregates begin to grow [Fig. 6.3B,E,F]. Future experiments will integrate a microfluidic device and semi-permeable membrane, such that the concentration of L-serine can be varied in time (cycling high and low *E. coli* swim speed), and also in space using a gradient of concentration.

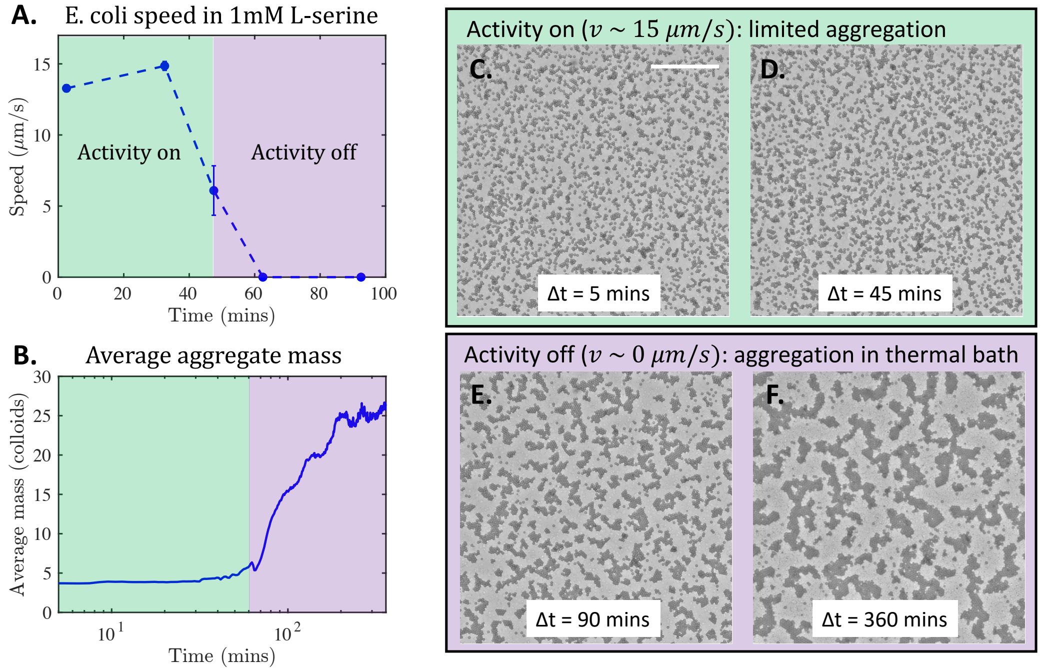

Figure 6.3. **(A)**. E. coli speed versus time with 1mM L-serine. We observe that the E. coli are motile for about 45 minutes, and then stop swimming. **(B)** Average mass as a function of time, for aggregates in a bacterial bath with 1mM L-serine and .8g/L PEO. At this low depletant concentration, we observe that the active bath is strong enough to inhibit binding, as evidenced by the limited aggregation during the first 45 minutes of experiment. After 45 minutes, the E. coli stop swimming (A), and the average aggregate mass slowly increases. **(C)** Snapshot of aggregates after 5 minutes. Scale bar 200um. **(D)**. Snapshot of aggregates after 45 minutes. Aggregates are comparable size to C. **(E)** Aggregates after 90 minutes. **(F)**. Aggregates after 6 hours. Same scale for C-F.

6.4 3D colloidal gel with dynamic material properties

The holy grail would be to develop a 3D colloidal gel with dynamic properties, powered by active matter. The previous two sections outlined different experimental methods to dynamically vary the speed of *E. coli*, modulating the energy injected into the soft material through the active bath.

The experiments presented in Fig. 6.3 are a proof of concept that, at low binding energy, the active bath is capable of breaking apart colloidal aggregates. We envision a 3D colloidal gel in a dynamic *E. coli* suspension; at the flip of a switch, the gel structure can be ruptured and reorganized, triggering a solid to liquid phase transition. Cycles of high and low *E. coli* speed will allow the structure to break apart and then reform, thus repairing defects in the material. Ancient Romans introduced lime into their concrete to create a material which would heal its cracks and therefore remain durable over thousands of years [100]. We hope to develop a colloidal gel with similar self healing properties.

Chapter 7

Appendix - derivations

The goal of the following chapter is to summarize the interactions between colloidal particles, relevant to understanding the experimental system. The chapter is broken up into four sections: Van Der Walls, Electrostatics, DLVO theory, and Depletion. This Chapter draw heavily from three textbooks: Robert J Hunter *Foundations of Colloid Science* [12], John C Berg, *Introduction to Interfaces and Colloids: The Bridge to Nanoscience* [14], and Tharwat F. Tadros, *Interacial Phenomena and Colloid Stability: Basic Principles* [13]. These topics are covered in greater detail within these books, and this chapter represents a synthesis of what I consider to be the most important pieces, relevant to understanding the experimental system. Whenever possible, I will include citations to the relevant chapters, for future readers.

7.1 Derjaguin approximation

Before we begin, we review the Derjaguin approximation. This technique is used to translate between planar geometry to spherical geometry - for many of the derivations, we will first derive the energy between planes (the math is typically easier), and then apply the Derjaguin approximation to get the energy between spheres (colloids are typically spheres!)

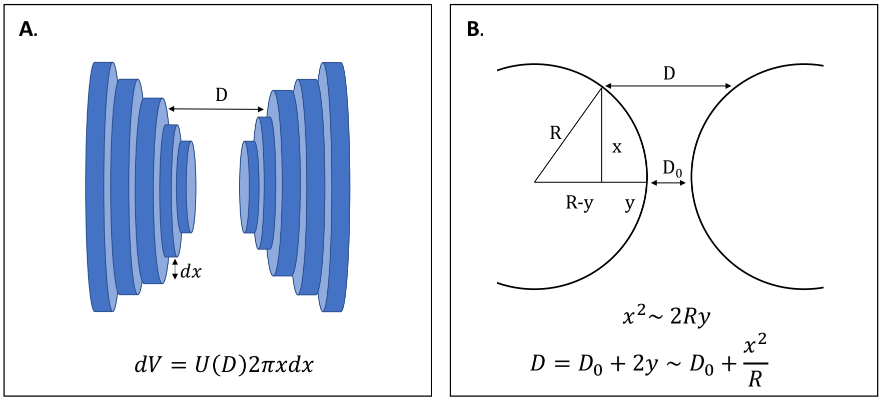

Figure 7.1. Derjaguin approximation (A) The starting point is to approximate a sphere as a series of flat, parallel facing disks of radius (x). **(B)** The distance between the disks (D) can be approximated as a function of the radius of the disks (x).

The starting point is to approximate a sphere as a series of flat, parallel facing disks, as depicted in Fig. 7.1A. We take $U(D)$ to be the interaction energy per unit area between two planes; thus, the interaction energy between each disk is given by $dV = U(D)2\pi x dx$ for a disk of radius x and thickness dx. The total energy between the spheres (V) is given by integrating dV.

$$V = \int U(D)2\pi x dx \tag{7.1}$$

In the following step, we approximate the distance between disks (D) as a function of the radius of the disk (x). Thus is visualized in Fig. 7.1B for two spheres of radius R; the important step is to write $R^2 = (R-y)^2 + x^2$, and recognize that y^2 is small. We arrive at:

$$D \sim D_0 + \frac{x^2}{R} \tag{7.2}$$

such that

$$dD \sim \frac{2}{R} x dx \tag{7.3}$$

we substitute this into the previous integral, and obtain the Derjaguin approximation:

$$V^{sphere}(D_0) = \pi R \int_{D_0}^{\infty} U^{plane}(D) dD \tag{7.4}$$

A few comments are in order. First, the bounds of the integral ($D_0 < D < \infty$) are only relevant if $U(D)$ recays rapidly with D. Second, geometrical approximation requires that the distance between the spheres D_0 be much less than the radius of the spheres R. As we will see in the following sections, these are reasonable approximations for both Van der Waals and double layer repulsive potential.

Throughout the following chapter, I will use V for a potential energy, U for potential energy per unit area, and Ψ for electric potential. Van der Walls potentials are V_A, since they are generally attractive. Double layer potentials are V_R, since they are generally repulsive.

7.2 Depletion interaction

The depletion interaction is entropic in origin; an effective attractive potential between the colloids arises from maximizing the entropy (available volume) of the depletants. For clarity, we begin by repeating the qualitative description given in Chapter 1, along with Fig. 1.3.

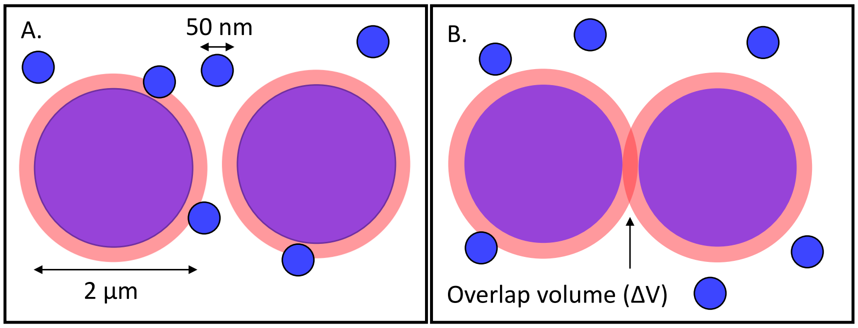

Figure 7.2. Depletion interaction (A) Colloids (purple), and depletants (blue) in solution. Surrounding each colloids is an excluded region (red), where the center of the depletant cannot enter. **(B)** Forcing the colloids together causes part of the excluded region to overlap. This maximizes the available space for the depletants. Since the depletants vastly outnumber the colloids, this maximizes the entropy of the system.

A qualitative description of the depletion interaction begins by recognizing that, surrounding each colloid (purple circles, Fig. 7.2A), there is an excluded region (red region, Fig. 7.2A) where the center of mass of the depletants (blue circles, Fig. 7.2A) cannot enter. By forcing the colloids together, part of this excluded region overlaps; this results in more available space for the depletants [Fig. 7.2B], maximizing their entropy. The depletants vastly outnumber the colloids; thus, forcing the colloids together maximizes the entropy of the system. For a closed system in thermal equilibrium, $F = U - TS$, with F the free energy, U the internal energy, T the temperature and S the entropy. For hard spheres, $U = 0$ outside of contact. Thus, maximizing the entropy of the system (S) minimizes the free energy (F).

7.2.1 Derivation of attractive potential

Starting with the partition function for an ideal gas (i.e. non-interacting depletants), we derive the change in free energy from adding a volume ΔV. The partition function Z for an ideal gas of N particles at given volume V given as

$$Z = \frac{V^N}{N!\lambda^{3N}} \tag{7.5}$$

With the free energy F given by

$$F = -k_{\mathrm{B}}T\ln(Z) = k_{\mathrm{B}}T\left(\ln(N!\lambda^{3N}) - \ln(V^N)\right) \tag{7.6}$$

Consider the case where a volume ΔV is added to the ideal gas. The partition function becomes

$$Z = \frac{(V+\Delta V)^N}{N!\lambda^{3N}} \tag{7.7}$$

with free energy

$$F = -k_{\mathrm{B}}T\ln(Z) = k_{\mathrm{B}}T\left(\ln(N!\lambda^{3N}) - \ln(V+\Delta V)^N\right) \tag{7.8}$$

we rearrange the term on the right such that

$$\ln(V+\Delta V)^N = N\ln(V\left(1+\frac{\Delta V}{V}\right)) \tag{7.9}$$

now we apply the log rule $\ln(AB) = \ln(A) + \ln(B)$ such that

$$N\ln(V\left(1+\frac{\Delta V}{V}\right)) = N\ln(V) + N\ln(1+\frac{\Delta V}{V}) \tag{7.10}$$

when ΔV is small compared to V, we can apply the taylor expansion ($\ln(1+x) \sim x$ for $x << 1$). Thus, we find

$$N\ln(V\left(1+\frac{\Delta V}{V}\right)) \sim N\ln(V) + \frac{N\Delta V}{V} \tag{7.11}$$

Thus, the free energy for an ideal gas of of volume $V+\Delta V$ is given as

$$F = k_{\mathrm{B}}T\left(\ln(N!\lambda^{3N}) - \ln(V^{N})\right) - k_{\mathrm{B}}T\frac{N\Delta V}{V} \tag{7.12}$$

We find the change in energy ($\Delta F = F(V+\Delta V) - F(V)$) from adding a volume ΔV is given by

$$\Delta F = -k_{\mathrm{B}}Tn_{p}\Delta V \tag{7.13}$$

for $n_p = N/V$, the number density of particles (depletants) in the system. The next step is to derive the size of the overlap volume ΔV, specific to the geometry of two spheres.

7.2.2 Overlap volume for two spheres using Derjaguin approximation

Borrowing from the previous section, we recognize that the radius of the spherical cap (labeled x, Fig. 7.3) to be $x \sim \sqrt{2Ra}$. We approximate the overlap volume as a cylinder of radius $x \sim \sqrt{2Ra}$ and height a. This leads to an overlap volume $\Delta V \sim 2\pi Ra^2$. The interaction energy between the colloids is given as:

$$\Delta E = -2\pi k_{\mathrm{B}}Tn_{p}a^{2}R \tag{7.14}$$

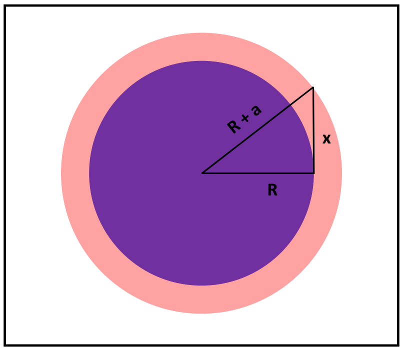

Figure 7.3. We estimate the radius of the spherical cap using the Derjaguin approximation. The radius (x) the spherical cap is $x \sim \sqrt{2Ra}$.

An more in depth derivation, using the exact volume of the cap, can be found in [18]. They find the energy, as a function of h, the distance between the colloids, to be

$$\Delta E = -2\pi k_{\mathrm{B}} T n_p a^2 R (1 - \frac{h}{2r})^2 \tag{7.15}$$

Taking the limit $h = 0$ (i.e. assuming the spheres are in contact), we recover Eq 7.14.

7.3 DLVO Theory

7.3.1 Van der Waals

Van der Waals interactions arise from interactions between dipoles; these can be both permanent dipoles or fluctuations in electron density. Polar, nonpolar, charged and uncharged molecules can all experience Van der Waals interactions. The interactions are generally considered ”weak” forces, compared to Hydrogen bonding or covalent bonding. Nevertheless, they play an important role in the forces between colloidal particles [13].

Short Range Van der Waals

The Van der Waals potential between two dipoles decays rapidly with distance (r)

$$V_A^{dipole}(r) \sim r^{-6} \tag{7.16}$$

A qualitative description picture for this begins by remembering that the electric field ($\mathbf{E}$) from a dipole, with dipole moment $\mathbf{p}$, can be approximated as

$$\mathbf{E} \sim \frac{\mathbf{p}}{r^3} \tag{7.17}$$

The potential energy (V) of a dipole interacting with an electric field is given by

$$V = -\mathbf{p} \cdot \mathbf{E} \tag{7.18}$$

such that the energy is minimized when the dipole points in the direction of the electric field. This result can be derived by integrating the torque ($\tau = \mathbf{p} \times \mathbf{E}$) applied to the dipole by an electric field, such that $V = \int \tau d\Theta$. The dipole tends to align with an electric field, such that the direction of the moment is aligned with the applied field; we can define a susceptibility (α) of the dipole, such that

$$\langle \mathbf{p} \rangle = \alpha \mathbf{E} \tag{7.19}$$

For the case of two dipole interacting with each other, we define the electric field of the first dipole as

$$\mathbf{E_1} \sim \frac{\mathbf{p_1}}{r^3} \tag{7.20}$$

This external field can be used to compute the dipole moment of the second dipole, such that

$$\langle \mathbf{p_2} \rangle \sim \alpha_2 \mathbf{E_1} \sim \frac{\alpha_2 \mathbf{p_1}}{r^3} \tag{7.21}$$

Thus, the potential energy between dipoles 1 (with electric field E_1) and dipole two (with dipole moment p_2) is given as

$$V_A^{dipole}(r) = -\mathbf{p_2} \cdot \mathbf{E_1} \sim r^{-6} \tag{7.22}$$

A more exact treatment of this can be found in Hunter, section 11.2 [12]. For our purposes, the scaling $V_{dipole}(r) \sim r^{-6}$ is sufficient. The potential decays rapidly with distance - hence, Van der Waals between two dipoles are sometimes referred to as ”short range” Van der Waals.

Long range Van der Waals

For two macroscopic bodies, the Van der Waals potential is integrated over the volume of each body; for two planes, separated by a distance r, this results in a potential $V_D(r) \sim r^{-}2$. This potential decays much slower than the potential for two dipoles. Hence, these are called ”long range” Van der Waals.

The following derivation is adapted from Berg Chapter 2.2 [14]. A similar derivation is given in Hunter Chapter 11.3 [12]. Consider a test dipole, located a vertical distance $z = D$ from an infinite plane. The plane contains a density of dipoles ρ, such that ring within the plane (of radius x, height dz and thickness dx) contains $2\pi\rho x dx dz$ number of dipoles.

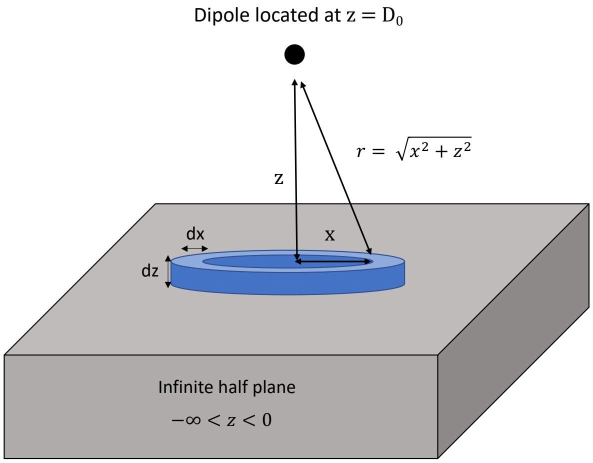

Figure 7.4. Long range Van der Waals Consider a test dipole, located a vertical distance $z = D_0$ from an infinite plane. The plane contains a density of dipoles ρ, such that ring within the plane (of radius x, height dz and thickness dx) contains $2\pi\rho x dx dz$ number of dipoles. The distance from the test dipole to the ring within the infinite plane is $r^2 = x^2 + z^2$.

Following the previous section, the potential between a pair of dipoles is written as

$$V_A^{dipole}(r) = -\frac{B}{r^6} \tag{7.23}$$

The energy between the test dipole and the half plane (V_A^{dip-hp}) is the sum of the interactions between the test dipole and each individual dipole in the half plane. It follows that the potential between the test dipole and the half plane can be written as

$$V_A^{dip-hp} = -B2\pi\rho \int_{D_0}^{\infty} \int_0^{\infty} \frac{x}{r^6} dxdz \tag{7.24}$$

Recognizing that $r^2 = x^2 + z^2$, this is re-written as

$$V_{dip-hp} = -B2\pi\rho \int_{D_0}^{\infty} \int_0^{\infty} \frac{x}{(x^2+z^2)^3} dxdz \tag{7.25}$$

Evaluating the first integral over x, we find

$$V_{dip-hp} = -\frac{\pi}{2} B\rho \int_{D_0}^{\infty} \frac{1}{z^4} dz \tag{7.26}$$

Evaluating the second integral of z, where the minimum vertical distance between the test dipole and the half plane is D_0, we find

$$V_A^{dip-hp} = -\frac{\pi B\rho}{6D_0^3} \tag{7.27}$$

This can be expanded to two half planes, separated by a distance D_0. In each slice of the upper half plane (of thickness dD and unit area), there are ρdD number of dipoles. Thus, the potential between a unit area of the upper half plane and the lower half plane, is:

$$U_A^{hp} = -\frac{\pi B\rho^2}{6} \int_{D_0}^{\infty} \frac{dD}{D^3} = -\frac{\pi B\rho^2}{12D_0^2} \tag{7.28}$$

We notice that the Van der Waals potential decays much slower between two macroscopic, with $U \sim D_0^{-2}$. A more through discussion of this can be found in Hunter Chapter 11.3-11.6.

For two planes separated by a distance D_0, the Van der Waals potential energy per unit area is given by (Hunter, 11.6.26)

$$U_A^{plane}(D_0) = -\frac{A_{ijk}}{12\pi D_0^2} \tag{7.29}$$

where A_{ijk} is the Hamaker constant, a material property which describes the interaction of plane i with plane j in media k. This can be modified for the case of two spheres of radius R using Deryaguin's approximation

$$V^{sphere}(D_0) = \pi R \int_{D_0}^{\infty} U^{plane}(x)dx \tag{7.30}$$

such that the potential between two spheres of radius R, separated by a distance D_0, is

$$V_A^{sphere}(D_0) = -\frac{A_{ijk}R}{12\pi D_0} \tag{7.31}$$

We notice that the Van der Waals potential between two spheres decays even slower than the potential between two plates. Typical values for the Hamaker constant of various materials in water are between 10^{-21} J and 10^{-20} J [14, 13] .

7.3.2 Electrostatics

Most colloids, when dispersed in water, develop a charge at the surface. It follows that Electrostatics play a key role in the interactions between colloids.

Colloids in Water

Most colloids, when dispersed in aqueous media, develop a charge at the surface. We will describe in detail the case of Silica colloids, as many examples can be found in the literature. The case for TPM colloids (as used in the experiments in this thesis) is expected to be quite similar, and is discussed at the end of this section. The following derivation is adapted from Berg Chapter 6.3; A more in depth discussion of the charge on the surface of silica can be found in [ref: Charge on Glass and Silica, Grier].

In the case of Silica colloids suspended in water, the charge at the surface is generally negative, due to the dissociation of a hydrogen.

$$\mathrm{SiOH} \leftrightharpoons \mathrm{SiO^-} + \mathrm{H^+} \tag{7.32}$$

The total number of sites on the surface remains fixed

$$N_s = [\mathrm{SiOH}] + [\mathrm{SiO^-}] \tag{7.33}$$

while the surface charge is proportional to the concentration of $\mathrm{SiO^-}$ groups on the surface.

$$\sigma_0 = -e[\mathrm{SiO^-}] \tag{7.34}$$

The equilibrium concentration of $\mathrm{SiO^-}$ is determined by the relevant mass action law and equilibrium constant K

$$\frac{[\mathrm{H^+}][\mathrm{SiO^-}]}{[\mathrm{SiOH}]} = K \tag{7.35}$$

The concentration of free hydrogen at the surface can be further expanded upon. It is expected to be in chemical equilibrium with free hydrogen in the bulk, which can be measured through the pH.

$$\mu_{H+} = k_B T \ln([\mathrm{H^+}]_b) = k_B T \ln([\mathrm{H^+}]_s) + e\Psi_0 \tag{7.36}$$

with $[\mathrm{H^+}]_b$ the bulk concentration of free hydrogen and $[\mathrm{H^+}]_s$ the concentration at the surface, and Ψ_0 the potential at the surface. The concentration of free hydrogen at the surface is given by the Boltzmann distribution:

$$[\mathrm{H^+}]_s = [\mathrm{H^+}]_b \exp(-\beta e \Psi_0) \tag{7.37}$$

To reasonable approximation, equations 7.34, 7.37, and 7.35 can be combined to describe the total charge on the surface.

$$\sigma_0 = \frac{-eN_s}{1 + \frac{[\mathrm{H}^+]}{K}\exp(-\beta e \Psi_0)} \tag{7.38}$$

We note that a more in accurate discussion of the charge of glass at the surface can be found in [11]. Nevertheless, equation 7.38 leads to a useful approximate description of the surface charge. At extremely high concentration of H^+ (low pH), the charge goes to zero. Meanwhile, in extremely basic conditions, the surface is entirely de-protonated and the charge is maximally negative. In this way, H^+ can be thought of as a potential determining ion. For metal oxides, Polystyrene latex beads, and many proteins, the pH will determine the surface potential, as discussed in Hunter Chapter 1.6 [12]. Colloids made of TPM polymer also carry a negative surface potential [9], likely due to the de-protonation of a silanol moitey [10].

Ions density in solution

As previously discussed, the surface of a colloid typically becomes charged when suspended in water. This creates an electric potential surrounding the colloid. In the following section, we will describe the interactions between this electric potential and the ions in the surrounding media.

Consider the case of a colloid with negative charge. When the surrounding media contains ions (positively, or negatively charged), the electric potential from the colloid will either attract or repel the surrounding ions, creating an inhomogenous distribution of charges in the surrounding media ($\rho(r)$). Via Poisson's Equation $\left(\nabla^2\Psi(r) = \frac{-\rho(r)}{\varepsilon}\right)$, the distribution of ions in the surrounding media determines the total electric potential in the region ($\Psi(r)$).

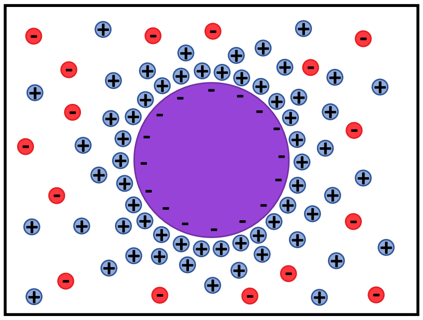

Figure 7.5. Diffuse double layer of ions Near the charged surface, a diffuse layer of oppositely charged ions forms. The resulting ion cloud screens the electric potential from the charged colloid.

As described in Fig. 7.5, a layer of oppositely charged ions develops around the charged colloids, termed the diffuse double layer. The ions near the charged surface are assumed to be in chemical equilibrium with the ions in the bulk, having their chemical potential (μ) modified by the electric potential. The concentration of ion of species i ($n_i(r)$) can be written as a Boltzmann distribution; the concentration depends linearly on the bulk concentration of ions (n_i^0), and exponentially on electric potential ($\Psi(r)$)

$$\mu_i = k_B T \ln(n_i^0) = k_B T \ln(n_i(r)) + e z_i \Psi(r) \tag{7.39}$$

$$n_i(r) = n_i^0 \exp\left(-\beta z_i e \Psi(r)\right) \tag{7.40}$$

Thus, the density of charge in solution is given by the charge per electron (e), times the valency per ion (z_i) times the concentration of ions ($n_i(r)$).

$$\rho(r) = \sum_i e z_i n_i = \sum_i e z_i n_i^0 \exp\left(-\beta z_i e \Psi(r)\right) \tag{7.41}$$

where n_i^0 gives the bulk concentration of ions of species i. This makes some assumptions about the ions, primarily that they do not interact with each other; rather, it is assumed that ions are primarily interacting with the charged surface. Now that we have the density of charges, we can invoke Poisson's Equation, to solve for the potential.

$$\nabla^2\Psi(r) = \frac{-\rho(r)}{\varepsilon} \tag{7.42}$$

$$\nabla^2\Psi(r) = \frac{-1}{\varepsilon}\sum_i n_i^0 z_i e \exp\left(-\beta z_i e\Psi(r)\right) \tag{7.43}$$

This is known as the Poisson-Bolzmann equation. In general, this equation is very difficult to solve in its full form, but assumptions can be made to find simple solutions. In the following sections, I will discuss some of the relevant approximate solutions. A more detailed look into this can be found in many of the standard textbooks, including Hunter Chapter 7 [12], Berg Chapter 6.B [14] and Tadros Chapter 2 [13].

Debye-Hückel approximation

Assuming that the electrical potential is much smaller than the Thermal energy (ie: $|z_i e\Psi \ll k_B T|$), one can expand the exponential in Eq. 7.43 using the Taylor expansion ($\exp(\varepsilon) \simeq 1+\varepsilon$). This is the Debye-Hückel (DH) approximation:

$$\frac{-1}{\varepsilon}\sum_i n_i^0 z_i e \exp\left(-\beta z_i e\Psi(r)\right) \simeq \frac{-1}{\varepsilon}\sum_i n_i^0 z_i e + \frac{1}{\varepsilon}\sum_i \frac{n_i^0 z_i^2 e^2\Psi}{k_B T} \tag{7.44}$$

The first order terms cancel out, since the bulk must be charge neutral. Thus, the Poisson Bolzmann equation is simplified to

$$\nabla^2\Psi = \kappa^2\Psi \tag{7.45}$$

$$\kappa^2 = \frac{e^2\sum_i n_i^0 z_i^2}{\varepsilon k_B T} \tag{7.46}$$

κ^{-1}, also known as the Debye Length (λ_D), sets the relevant length sale for the Electrostatic forces, and the diffuse double layer of ions surrounding the charged colloid. It is often interpreted as the "screening length" since at distances greater than the Debye length, the potential is effectively screened by the surrounding ions [14]. The Debye length is dependent on the ion concentration; a good number to remember is the Debye length in 1mM NaCl solution is about 10nm.

$$\lambda_D(\mathrm{nm}) \sim \frac{10}{\sqrt{c}} \tag{7.47}$$

for c the ionic strength, in units of mM.

Finally, it is worth noting that this solution is only derived in the limit of $|z_i e\Psi \ll k_B T|$. For a monovalent ion ($z_i = \pm 1$), this means $|\Psi| \ll 25\mathrm{mV}$. Through experimental measurements of the zeta potential [9] [16], we know that this is often not the case, with typical values between -10 mV and -50 mV. For now, we will stay within the DH approximation, and solve for the potential. Later, we will study the full solution to the Poisson - Boltzmann equation (see: Section 7.3.2, and 7.3.2), and compare the solutions of the DH approximation to confirm its validity.

Solutions to DH equation

Eq. 7.45 can be solved near a plane with relative ease. The general solution being:

$$\Psi = A\exp(-\kappa r) + B\exp(\kappa r) \tag{7.48}$$

For r, the distance from surface. Invoking that the potential decays to zero at infinity requires $B = 0$. To solve for A, there are two relevant boundary conditions.

Constant surface potential First, one could specify the condition $\Psi(r = 0) = \Psi_0$

$$\Psi = \Psi_0 \exp(-\kappa r) \tag{7.49}$$

Additionally, one could specify that the potential at some point ($x = \delta$) in the diffuse layer is held constant ($\Psi(\delta) = \Psi_\delta$). This comes from a more robust description of the diffuse double layer (Stern Model, see Berg 6.6 [14]), which makes a a distinction between charges that are specifically absorbed at the surface, and charges that are freely diffusing.

$$\Psi = \Psi_\delta \exp\left(-\kappa(r-\delta)\right) \tag{7.50}$$

Constant surface charge Considering our understanding of the charge accumulated on the surface of Silica coming from a chemical equilibrium with the surrounding free hydrogen, it is also important to discuss the boundary condition where surface charge (σ_0) is held constant, rather than potential. The boundary condition at the surface (r=0) thus reads:

$$\left(\frac{\partial \Psi}{\partial r}\right)_{r=0} = -\frac{\sigma_0}{\varepsilon} \tag{7.51}$$

and the potential distribution

$$\Psi(r) = \frac{\sigma_0}{\varepsilon\kappa}\exp(-\kappa r) \tag{7.52}$$

As discussed in the previous section (see Eq. 7.38), the charge at the surface of Silica depends not only on the concentration of free hydrogen, but also the surface potential. Thus, neither the constant potential nor constant charge solutions should be treated as exact, rather upper and lower limits for the solution. A more in depth discussion of how to treat these boundary conditions can be found in Berg Chapter 6.3 [14], along with an example using the Carboxylic Acid (-COOH) functional group.

Full Solution to Poisson- Boltzmann Equation

It is possible to derive a full solution for the Poisson-Bolzmann equation for a symmetric 1:1 electrolyte (ie: $z_1 = +1$ and $z_2 = -1$) near the surface of a plane. A partial derivation can be found in Hunter chapter 7.3 [12], with many steps left as exercises for the reader. A full derivation can be found below:

We start with the Poisson-Boltzmann equation (Eq. 7.43)

$$\nabla^2\Psi(r) = \frac{-1}{\varepsilon}\sum_i n_i^0 z_i e \exp\left(-\beta z_i e \Psi(r)\right) \tag{7.53}$$

In the case of a symmetric 1:1 electrolyte, the summation on the right side of the Poisson-Boltzmann equation can be written as:

$$\frac{\partial^2\Psi}{\partial r^2} = \frac{n^0 e}{\varepsilon}(\exp(\beta e\Psi) - \exp(-\beta e\Psi) \tag{7.54}$$

Through the definition of hyperbolic sin function (i.e. $2\sinh(x) = e^x - e^{-x}$), this becomes

$$\frac{\partial^2\Psi}{\partial r^2} = \frac{2n^0 e}{\varepsilon}\sinh(\beta e\Psi) \tag{7.55}$$

Which can be integrated by multiplying both sides by $2\frac{\partial\Psi}{\partial x}$, such that

$$2\frac{\partial\Psi}{\partial r}\frac{\partial^2\Psi}{\partial r^2} = 2\frac{\partial\Psi}{\partial r}\frac{2n^0 e}{\varepsilon}\sinh(\beta e\Psi) \tag{7.56}$$

and recognizing the left hand side to be the $\frac{\partial}{\partial r}(\frac{\partial\Psi}{\partial r})^2$. The right hand side is integrated, using the boundary condition that $\frac{\partial\Psi}{\partial r} = 0$ when $\Psi = 0$. Thus we arrive at

$$(\frac{\partial\Psi}{\partial r})^2 = \frac{4n^0 e}{\varepsilon}(\cosh(\beta e\Psi) - 1) \tag{7.57}$$

This is simplified with two subsitutions. First, the half angle rule for hyperbolic cosh (ie: $\cosh(p) = 2\sinh^2(p/2) + 1$). Second, using the definition of the Debye Length (Eq. 7.45), n^0/ε is replaced with $\kappa^2/2\beta e^2$. Thus:

$$\frac{\partial\Psi}{\partial r} = \frac{-2\kappa}{\beta e}\sinh(\frac{\beta e\Psi}{2}) \tag{7.58}$$

The $(-)$ sign is chosen when taking the square root, such that $\frac{\partial\Psi}{\partial x} < 0$ when $\Psi > 0$. Using the double angle rule for hyperbolic sine function (ie: $\sinh(p) = 2\sinh(p/2)\cosh(p/2)$), the equation becomes:

$$\frac{\partial \Psi}{\partial r} = \frac{-4\kappa}{\beta e} \sinh(\frac{\beta e \Psi}{4}) \cosh(\frac{\beta e \Psi}{4}) \tag{7.59}$$

Multiplying both sides by $\mathrm{sech}^2(\frac{\beta e \Psi}{4}) = 1/\cosh^2(\frac{\beta e \Psi}{4})$ and recognizing $\frac{\partial}{\partial x} \tanh p = \mathrm{sech}^2 p \frac{\partial p}{\partial x}$ leads to the following equation:

$$\frac{\partial \tanh(\frac{\beta e \Psi}{4})}{\tanh(\frac{\beta e \Psi}{4})} = -\kappa \partial r \tag{7.60}$$

Finally, we recognize that this is differential equation takes the form

$$\frac{\partial y}{y} = \partial x \tag{7.61}$$

which can be integrated (with conditions $y(x_0) = y_0$), to obtain

$$\log(y/y_0) = x - x_0 \tag{7.62}$$

Integrating from point in the diffuse layer, with conditions $\Psi(d) = \Psi_d$, gives the full solution:

$$\tanh(\beta e \Psi/4) = \tanh(\beta e \Psi_d/4) \exp(-\kappa(r-d)) \tag{7.63}$$

A few words are in order. First, notice that when both Ψ and Ψ_d are small compared to $4k_BT/e$ (about 100mV at room temperature), you recover the solution to the Debye-Huckle model with a constant potential (using the expansion $\tanh(\varepsilon) \sim \varepsilon$).

Additionally, if only Ψ is small, but Ψ_d is not (for example, far away from the charged surface), then the solution can be approximated as:

$$\Psi = Z \exp(-\kappa(r-d)) \ ; \ Z = \frac{4k_BT}{e} \tanh(\beta e \Psi_d/4) \tag{7.64}$$

Now, we have three solutions for the the Poisson Boltzmann equation near a plane (considering the case of constant surface potential). In the following section, I will do my best to compare the solutions.

Comparison of relevant approximations

We have identified three equations for the Electric potential near a plane, each using different approximations. In each case, the boundary condition is that the potential at a position within the double layer is held constant, such that $\Psi(\delta) = \Psi_\delta$ (For the case of a constant surface potential, one can take $\delta = 0$) For review, they are listed below:

(1) Debye-Hückel Approximation The DH approximation stems from stating that the electrical potential is much smaller than the Thermal energy (ie: $|z_i e\Psi \ll k_B T|$) . The relevant equation is given by Eq. 7.50 :

$$\Psi(r) = \Psi_\delta \exp\left(-\kappa(r-\delta)\right) \tag{7.65}$$

(2) Full solution to the Poisson-Boltzmann Equation The Poisson-Boltzmann equation can be solved in full for the case of symmetric 1:1 ions. This is gives Eq. 7.63:

$$\tanh(\beta e\Psi/4) = \tanh(\beta e\Psi_d/4)\exp(-\kappa(r-d)) \tag{7.66}$$

(3) Full solution to the Poisson-Boltzmann Equation, far away form the surface Eq. 7.63 can be simplified in the case that you are far away from the surface (i.e. Ψ is small, but Ψ_d is not). This yields Eq. 7.64:

$$\Psi = Z\exp(-\kappa(r-d)) \;\; ; \;\; Z = \frac{4k_B T}{e}\tanh(\beta e\Psi_d/4) \tag{7.67}$$

I find the most intuitive way to understand the differences between these three solutions is to plot them against each other (as seen in Fig. 7.6). We find that for $\Psi_d \leq$ 50mV, all three solutions are comparable. For large values of Ψ_d , Equation Eq. 7.63 tends to underestimate the potential (especially true for small $r-\delta$), while the DH approximation tends to overestimate.

Experimental measurements of the zeta potential of TPM polymer colloids typically range between -10 mV and -50 mV [16] [9]. This validates our use of the DH approximation.

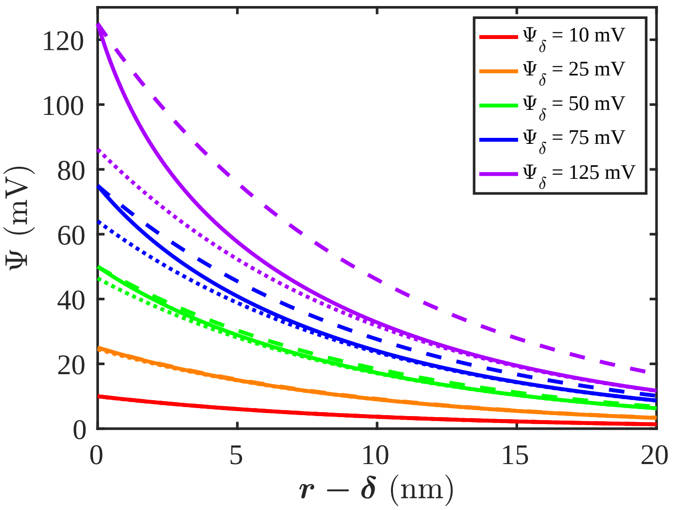

Figure 7.6. Solutions to the Poisson-Boltzmann equation The full solution to the Poisson-Boltzmann equation (Eq. 7.63) is plotted as solid lines. An approximation to the full solution, valid far from the surface, (Eq. 7.64) is plotted as a dotted line. The solution using the Debye-Hückel approximation (Eq. 7.50) is dashed lines. All solutions assume a Debye length of 10nm. Different colors represent different surface potentials (see legend).

Double Layer Forces

Having derived the potential near a charged surface in solution with ions, it is now possible to discuss the energetic costs to bring two of these charged surfaces, and their associated ion clouds, near each other - termed **Double layer forces**. Further reading can be found in Berg Chapter 6.C.1 [14], and Hunter Chapter 12 [12].

Roadmap: The following derivation is quite tedious. To avoid getting lost along the way, we include a general guide in the beginning.

1) Each charged plane carries with it a diffuse double layer of ions. When the planes are brought close together, there is a higher concentration of ions between the planes than in the bulk - creating an effective osmotic pressure. We will derive the pressure as a function of the electric potential at the midpoint between the planes Ψ_{mid}

2) Solve the Poisson Bolzmann equation, with the relevant boundary conditions, to obtain Ψ_{mid} as a function of the distance between the plates and the surface potential, Ψ_0

3) Integrate the osmotic pressure, bringing the plates from infinity to a distance D_0. This gives the potential energy per unit area $U_R(D_0)$ between two charged plates.

4) Apply the Derjaguin approximation, to obtain the repulsive potential energy between two spheres V_R

Osmotic pressure from ion cloud

Consider two charged planes, each with an associated ion cloud; the planes are separated by a distance D and each plane has the same surface potential Ψ_0. The standard derivation starts with the osmotic pressure (Π) between two planes. As the planes come together, a high density of ions builds between the two, due to the ion cloud associated with each plane. The osmotic pressure is given as the difference in number density of ions in the region between the planes versus in the bulk. For simplicity, we will restrict to ourselves to a system with a simple 1:1 electrolyte (ie: $z_1 = 1, z_2 = -1$).

$$\Pi(D) = k_BT(n_+(D/2) + n_-(D/2) - 2n_0) \tag{7.68}$$

Where n_0 equal to the bulk concentration of ions, far from the charged surface. The concentration of ions near the plane is further defined using the Boltzmann equation (Eq. 7.40). The potential at the midpoint between the planes is given as Ψ_{mid}. Thus, we have:

$$\Pi(D) = k_BTn_0(\exp(\beta e\Psi_{mid}) + \exp(-\beta e\Psi_{mid}) - 2) \tag{7.69}$$

Using the identity $2\cosh(x) = e^x + e^{-x}$, this can be re-written as:

$$\Pi(D) = 2k_BTn_0(\cosh(\beta e\Psi_{mid}) - 1) \tag{7.70}$$

Applying the DH approximation ($e\Psi_{mid} \ll k_BT$), the cosh term can be expanded using the Taylor expansion (i.e. : $\cosh(x) \simeq 1 + x^2/2$).

$$\Pi(D) = k_BTn_0(\beta e\Psi_{mid})^2 \tag{7.71}$$

Finally, we can simplify the constants in terms of the Debye length $\left(\frac{1}{\kappa^2} = \frac{\varepsilon k_BT}{2n_0e^2}\right)$

$$\Pi(D) = \frac{\kappa^2\varepsilon}{2}\Psi_{mid}^2 \tag{7.72}$$

Now, we have the pressure as a function of the distance between two charged plates, as given by Hunter (12.3.12) [12]. The repulsive potential energy per unit area is given by integrating the pressure, bringing the planes from infinity to a distance of D_0

$$U_R(D_0) = -\int_{\infty}^{D_0} \Pi(D)dD \tag{7.73}$$

Determine the potential at midpoint between spheres Ψ_{mid}

The next step is to determine the potential between the plates, such that we know Ψ_{mid}.

There are a few ways to proceed from here. To good approximation, the potential at the midpoint (Ψ_{mid}) is given by the superposition of the potentials due to each plate - this treatment can be found in Hunter Chapter 12.3.1 [12].

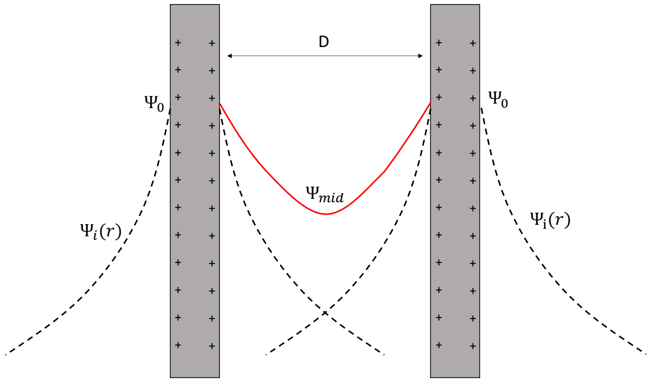

Figure 7.7. Boundary conditions for electric potential between two planes. Graphical representation of the electric potential between two charged plates at distance D. The potential from each plate (Ψ_i) is drawn in black, and the combined potential Ψ in red. The combined potential is assumed to be symmetric, such that at the midway point, $\frac{\partial\Psi}{\partial r} = 0$.

Another approximation would be to solve the Poisson Equation within the DH approximation, with the condition that $\frac{\partial\Psi}{\partial r} = 0$ at the midpoint between the plates ($\Psi(D/2) = \Psi_{mid}$) A graphical representation is given in Fig. 7.7. Considering the previous section, discussing the validity of the DH approximation, I will proceed with the second. This following derivation can be found as Exercises 12.3.5, 12.3.5 and 12.5.1 in Hunter [12].

We begin with Eq. 7.45

$$\nabla^2\Psi = \kappa^2\Psi \tag{7.74}$$

and multiply both sides by $2\dfrac{\partial\Psi}{\partial r}$, such that we have

$$2\frac{\partial\Psi}{\partial r}\frac{\partial^2\Psi}{\partial r^2} = 2\frac{\partial\Psi}{\partial r}\kappa^2\Psi \tag{7.75}$$

We notice that the left side can be re-written as

$$2\frac{\partial\Psi}{\partial r}\frac{\partial^2\Psi}{\partial r^2} = \frac{\partial}{\partial r}\left(\frac{\partial\Psi}{\partial r}\right)^2 \tag{7.76}$$

We insert this into Eq. 7.75, and integrate both sides over r

$$\int \frac{\partial}{\partial r}\left(\frac{\partial\Psi}{\partial r}\right)^2 dr = \int 2\frac{\partial\Psi}{\partial r}\kappa^2\Psi dr \tag{7.77}$$

the left side gives $\left(\frac{\partial\Psi}{\partial r}\right)^2$. The right side yields $\kappa^2\Psi^2 + C$, where C is a constant of integration. Inserting the boundary condition $\frac{\partial\Psi}{\partial r} = 0$ at $\Psi = \Psi_{mid}$, we have

$$\left(\frac{\partial\Psi}{\partial r}\right)^2 = \kappa^2(\Psi^2 - \Psi_{mid}^2) \tag{7.78}$$

leading to

$$\left(\frac{\partial\Psi}{\partial r}\right) = \kappa(\Psi^2 - \Psi_{mid}^2)^{1/2} \tag{7.79}$$

re-arranging terms we have

$$\int_{\Psi_0}^{\Psi_{mid}} \frac{\partial\Psi}{(\Psi^2 - \Psi_{mid}^2)^{1/2}} = \int_0^{D/2} \kappa\partial r \tag{7.80}$$

Here, we ansatz that Ψ takes the form $\Psi = \Psi_{mid}\cosh(W)$, for some function W.

Thus, $\partial\Psi = \Psi_{mid}\sinh(W)\partial W$. The left side can be re-written as:

$$\int \frac{\partial\Psi}{(\Psi^2 - \Psi_{mid}^2)^{1/2}} = \int \frac{\Psi_{mid}\sinh(W)}{(\Psi_{mid}^2\cosh(W)^2 - \Psi_{mid}^2)^{1/2}}\partial W = \int \partial W \tag{7.81}$$

Therefore, Eq. 7.80 yields $W = \kappa D/2$ for $\Psi = \Psi_{mid}\cosh(W)$

Thus, the potential at the midpoint between two charged planes separated by a distance D (with surface potential Ψ_0, within the limits of the DH approximation) is given by

$$\Psi_{mid} = \frac{\Psi_0}{\cosh(\frac{\kappa D}{2})} \tag{7.82}$$

Determine potential energy to bring plates together

In the previous section, we determined that the osmotic pressure from the high density of ions between the plates was given by

$$\Pi(D) = \frac{\kappa^2 \varepsilon}{2} \Psi_{mid}^2 \tag{7.83}$$

additionally, the potential energy per unit area to bring the planes from infinity to a distance of D_0 is given by

$$U_R(D_0) = -\int_{\infty}^{D_0} \Pi(D) dD \tag{7.84}$$

Now we insert our equation for Ψ_{mid} (Eq. 7.82) to solve for the potential energy per unit area

$$U_R(D_0) = -\frac{\kappa^2 \varepsilon \Psi_0^2}{2} \int_{\infty}^{D_0} \cosh\left(\frac{\kappa D}{2}\right)^{-2} dD \tag{7.85}$$

inserting $\cosh(x)^{-1} = \mathrm{sech}(x)$, we have

$$U_R(D_0) = -\frac{\kappa^2 \varepsilon \Psi_0^2}{2} \int_{\infty}^{D_0} \mathrm{sech}\left(\frac{\kappa D}{2}\right)^{2} dD \tag{7.86}$$

which yields

$$U_R(D_0) = -\frac{\kappa^2 \varepsilon \Psi_0^2}{2} \left(\frac{2}{\kappa}\right) \left[\tanh\left(\frac{\kappa D}{2}\right)\right]\Bigg|_{\infty}^{D_0} \tag{7.87}$$

Thus, the repulsive potential energy per unit area for two charged planes at a distance D_0 is given by: (equivalent to Hunter, 12.3.16)

$$U_R^{plane}(D_0) = \kappa \varepsilon \Psi_0^2 \left[1 - \tanh\left(\frac{\kappa D_0}{2}\right)\right] \tag{7.88}$$

Apply Deryaguin's approximation to determine V_R for two spheres

The final piece is to apply Deryaguin's approximation to Eq. 7.88, to determine V_R between two spheres (of radius R). This is exercise 12.5.1 in Hunter [12]; for the interested reader, Chapter 12.5 of Hunter discusses the use of other approximation methods, including the case where the Debye length is of comparable size as the colloid.

Deryaguin's approximation is given by

$$V^{sphere}(D_0) = \pi R \int_{D_0}^{\infty} U^{plane}(x)dx \tag{7.89}$$

For two spheres (with radius R, surface potential Ψ_0, separated by a distance D_0):

$$V_R(D_0) = \pi\kappa\varepsilon R\Psi_0^2 \int_{D_0}^{\infty} \left[1 - \tanh\left(\frac{\kappa x}{2}\right)\right] dx \tag{7.90}$$

we insert the definition of $\tanh(z)$

$$\tanh(z) = \frac{e^z - e^{-z}}{e^z + e^{-z}} \tag{7.91}$$

thus, $1 - \tanh(z)$ can be re-written as

$$1 - \tanh(z) = \frac{e^z + e^{-z} - (e^z - e^{-z})}{e^z + e^{-z}} = \frac{2e^{-z}}{e^z + e^{-z}} = \frac{2e^{-2z}}{1 + e^{-2z}} \tag{7.92}$$

Allowing us to re write the repulsive potential energy as

$$V_R(D_0) = 2\pi\kappa\varepsilon R\Psi_0^2 \int_{D_0}^{\infty} \frac{e^{-\kappa x}}{1 + e^{-\kappa x}} dx \tag{7.93}$$

next, we can say $Y = 1 + e^{-\kappa x}$, such that $\frac{\partial Y}{\partial x} = -\kappa e^{-\kappa x}$. The integral is re-written as

$$V_R(D_0) = -2\pi\varepsilon R\Psi_0^2 \int_{D_0}^{\infty} \frac{dY}{Y} = -2\pi\varepsilon R\Psi_0^2 \left[\ln(1 + e^{-\kappa x})\right]\Big|_{D_0}^{\infty} \tag{7.94}$$

Finally, the repulsive potential energy between two charged spheres at a distance D_0 (as given by

Hunter, 12.5.2) is:

$$V_R^{sphere}(D_0) = 2\pi\varepsilon R\Psi_0^2 \ln(1+e^{-\kappa D_0}) \tag{7.95}$$

After some effort, we are now able to write down the repulsive potential energy between two spheres (V_R^{sphere}, Eq. 7.95). In the previous section on Van der Waals, we have determined the attractive potential energy (V_A^{sphere}, Eq. 7.31). We combine the two in the following section on DLVO theory, analyzing the stability of colloids as a function of the ionic concentration.

7.3.3 DLVO Theory

The theories of Van der Waals attraction and double layer repulsion can be combined to discuss the stability of colloidal systems as a function of ion concentration. This is commonly referred to as DLVO theory, after the scientists who developed it: Deryaguin Landau Verwek and Overbeek. The total potential energy between two charged colloids can be written as a function of the distance between them (r)

$$V_{DLVO}(r) = V_A(r) + V_R(r) \tag{7.96}$$

with V_D the attractive potential from Van der Waals interactions, and V_R the repulsive potential from the double layer. Using Eq. 7.31 and Eq. 7.95 , the full equation can be written as

$$V_{DLVO}(r) = -\frac{A_{ijk}R}{12\pi r} + 2\pi\varepsilon R\Psi_0^2 \ln(1+e^{-\kappa r}) \tag{7.97}$$

with R the radius of the colloid, Ψ_0 the surface potential, κ^{-1} the Debye length, and A_{ijk} the Hamaker constant. We understand that, as the ionic strength (c) increases. the repulsive potential is increasingly screened ($\kappa \sim \sqrt{c}$). Meanwhile, the attractive Van der Waals potential remains unchanged. It results that the potential energy barrier between the colloids collapses at sufficient ion concentration ($V_{DLVO} < 0$ for all r). The colloidal suspension is de-stabilized, and begins to aggregate. These dynamics are visualized in the following figure.

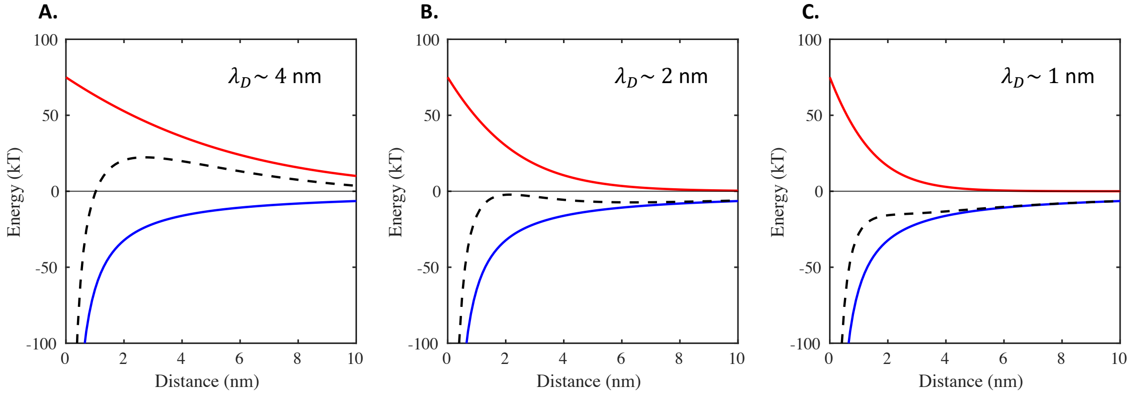

Figure 7.8. DLVO theory Solutions to Eq. 7.97 for increasing ion concentrations. V_D (Van der Waals) is plotted in blue, V_R (repulsive) is plotted in red, and the sum V_{DLVO} in black. Ion concentrations (c) in each figure are: **(A)** 5mM, **(B)** 30mM and **(C)** 75mM. κ is determined using Eq. 7.47, such that $\kappa \sim \sqrt{c}$. Constants are: R = 1μm, Ψ_0= -10mV, A_{ijk} = 10^{-20}J, and $\varepsilon = \varepsilon_0\varepsilon_r$ with ε_0 vacuum permittivity $8.85 * 10^{-12}$ F m^{-1} and relative permittivity ε_r = 80. As the ion concentration increases, the repulsive potential is increasingly screened. Meanwhile, the attractive Van der Waals potential remains unchanged. It results that the net repulsive barrier between colloids collapses at sufficient ion concentration.

Bibliography

[1] Pierre-Gilles de Gennes. Soft Matter (Nobel Lecture). *Angewandte Chemie International Edition in English*, 31(7):842–845, 1992.

[2] Emanuela Del Gado, Davide Fiocco, Giuseppe Foffi, Suliana Manley, Veronique Trappe, and Alessio Zaccone. *Fluids, Colloids and Soft Materials*. John Wiley and Sons, Ltd, 2016.

[3] M. C. Marchetti, J. F. Joanny, S. Ramaswamy, T. B. Liverpool, J. Prost, Madan Rao, and R. Aditi Simha. Hydrodynamics of soft active matter. *Reviews of Modern Physics*, 85(3):1143–1189, 2013.

[4] Peter J. Lu and David A. Weitz. Colloidal Particles: Crystals, Glasses, and Gels. *Annual Review of Condensed Matter Physics*, 4(1):217–233, 2013.

[5] Theodore Hueckel, Glen M. Hocky, and Stefano Sacanna. Total synthesis of colloidal matter. *Nature Reviews Materials*, 6(11):1053–1069, 2021.

[6] Stephen G. Lipson, Henry Lipson, and David Stefan Tannhauser. *Optical Physics*. Cambridge University Press, 3 edition, 1995.

[7] A Einstein. The motion of elements suspended in static liquids as claimed in the molecular kinetic theory of heat. *Annalen der physik*, 17(8):549 – 560, 07 1905.

[8] Jean Perrin. Mouvement brownien et realite moleculaire. *Le Radium*, 6(12):353–360, 00 1909.

[9] Casper van der Wel, Rohit K. Bhan, Ruben W. Verweij, Hans C. Frijters, Zhe Gong, Andrew D. Hollingsworth, Stefano Sacanna, and Daniela J. Kraft. Preparation of Colloidal Organosilica Spheres through Spontaneous Emulsification. *Langmuir*, 33(33):8174–8180, 2017.

[10] Mena Youssef and Stefano Saccana. *Synthesis and Directed Assembly of Colloids with Novel Functions*. PhD thesis, NYU Graduate School of Arts and Sciences, 2019.

[11] Sven H Behrens and David G Grier. The charge of glass and silica surfaces. *The Journal of Chemical Physics*, 115(14):6716–6721, 2001.

[12] R.J. Hunter and L.R. White. *Foundations of Colloid Science*. Number Bd. 2 in Foundations of Colloid Science. Clarendon Press, 1987.

[13] Tharwat F. Tadros. *Interfacial Phenomena and Colloid Stability: Volume 1 Basic Principles*. De Gruyter, Berlin, München, Boston, 2015.

[14] J.C. Berg. *An Introduction to Interfaces & Colloids: The Bridge to Nanoscience*. World Scientific, 2010.

[15] Hideyo Tsurusawa, Shunto Arai, and Hajime Tanaka. A unique route of colloidal phase separation yields stress-free gels. *Science Advances*, 6(41):eabb8107, 2020.

[16] Mena Youssef, Alexandre Morin, Antoine Aubret, Stefano Sacanna, and Jérémie Palacci. Rapid characterization of neutral polymer brush with a conventional zetameter and a variable pinch of salt. *Soft Matter*, 16(17):4274–4282, 2020.

[17] S. Sacanna, W. T. M. Irvine, P. M. Chaikin, and D. J. Pine. Lock and key colloids. *Nature*, 464(7288):575–578, 2010.

[18] S.M. Oversteegen and H.N.W. Lekkerkerker. On the accuracy of the Derjaguin approximation for depletion potentials. *Physica A: Statistical Mechanics and its Applications*, 341:23–39, 2004.

[19] S.K. Friedlander. *Smoke, Dust, and Haze: Fundamentals of Aerosol Dynamics*. Topics in chemical engineering. Oxford University Press, 2000.

[20] S R Forrest and T A Witten Jr. Long-range correlations in smoke-particle aggregates. *Journal of Physics A: Mathematical and General*, 12(5):L109, 1979.

[21] D. A. Weitz and M. Oliveria. Fractal Structures Formed by Kinetic Aggregation of Aqueous Gold Colloids. *Physical Review Letters*, 52(16):1433–1436, 1983.

[22] W.C.K. Poon and M.D. Haw. Mesoscopic structure formation in colloidal aggregation and gelation. *Advances in Colloid and Interface Science*, 73:71–126, 1997.

[23] D. A. Weitz, J. S. Huang, M. Y. Lin, and J. Sung. Limits of the Fractal Dimension for Irreversible Kinetic Aggregation of Gold Colloids. *Physical Review Letters*, 54(13):1416–1419, 1985.

[24] Juan J. Cerdà, Tomás Sintes, C. M. Sorensen, and A. Chakrabarti. Kinetics of phase transformations in depletion-driven colloids. *Physical Review E*, 70(1):011405, 2004.

[25] Sam E. Griffiths, Nick Koumakis, Aidan T. Brown, Teun Vissers, Patrick B. Warren, and Wilson C. K. Poon. Diffusion, phase behavior, and gelation in a two-dimensional layer of colloids in osmotic equilibrium with a polymer reservoir. *The Journal of Chemical Physics*, 155(7):074903, 2021.

[26] E M Purcell. Life at low Reynolds number. *American Journal of Physics*, 45(1):3–11, 1977.

[27] Jana Schwarz-Linek, Jochen Arlt, Alys Jepson, Angela Dawson, Teun Vissers, Dario Miroli, Teuta Pilizota, Vincent A. Martinez, and Wilson C.K. Poon. Escherichia coli as a model active colloid: A practical introduction. *Colloids and Surfaces B: Biointerfaces*, 137:2–16, 2016.

[28] Knut Drescher, Jörn Dunkel, Luis H. Cisneros, Sujoy Ganguly, and Raymond E. Goldstein. Fluid dynamics and noise in bacterial cell–cell and cell–surface scattering. *Proceedings of the National Academy of Sciences*, 108(27):10940–10945, 2011.

[29] M D Manson, P Tedesco, H C Berg, F M Harold, and C Van der Drift. A protonmotive force drives bacterial flagella. *Proceedings of the National Academy of Sciences*, 74(7):3060–3064, 1977.

[30] Ekaterina Krasnopeeva, Chien-Jung Lo, and Teuta Pilizota. Single-Cell Bacterial Electrophysiology Reveals Mechanisms of Stress-Induced Damage. *Biophysical Journal*, 116(12):2390–2399, 2019.

[31] Howard C. Berg. Motile Behavior of Bacteria. *Physics Today*, 53(1):24–29, 2000.

[32] Howard C. Berg and Douglas A. Brown. Chemotaxis in Escherichia coli analysed by Three-dimensional Tracking. *Nature*, 239(5374):500–504, 1972.

[33] Allison P. Berke, Linda Turner, Howard C. Berg, and Eric Lauga. Hydrodynamic Attraction of Swimming Microorganisms by Surfaces. *Physical Review Letters*, 101(3):038102, 2007.

[34] Xiao-Lun Wu and Albert Libchaber. Particle Diffusion in a Quasi-Two-Dimensional Bacterial Bath. *Physical Review Letters*, 84(13):3017–3020, 2000.

[35] Gastón Miño, Thomas E. Mallouk, Thierry Darnige, Mauricio Hoyos, Jeremi Dauchet, Jocelyn Dunstan, Rodrigo Soto, Yang Wang, Annie Rousselet, and Eric Clement. Enhanced Diffusion due to Active Swimmers at a Solid Surface. *Physical Review Letters*, 106(4):048102, 2010.

[36] G. L. Miño, J. Dunstan, A. Rousselet, E. Clément, and R. Soto. Induced diffusion of tracers in a bacterial suspension: theory and experiments. *Journal of Fluid Mechanics*, 729:423–444, 2013.

[37] Alys Jepson, Vincent A. Martinez, Jana Schwarz-Linek, Alexander Morozov, and Wilson C. K. Poon. Enhanced diffusion of nonswimmers in a three-dimensional bath of motile bacteria. *Phys. Rev. E*, 88:041002, Oct 2013.

[38] Kyriacos C. Leptos, Jeffrey S. Guasto, J. P. Gollub, Adriana I. Pesci, and Raymond E. Goldstein. Dynamics of enhanced tracer diffusion in suspensions of swimming eukaryotic microorganisms. *Phys. Rev. Lett.*, 103:198103, Nov 2009.

[39] Raphaël Jeanneret, Dmitri O. Pushkin, Vasily Kantsler, and Marco Polin. Entrainment dominates the interaction of microalgae with micron-sized objects. *Nature Communications*, 7(1):12518, 2016.

[40] R Di Leonardo, L Angelani, D Dell Arciprete, G Ruocco, V Iebba, S Schippa, M P Conte, F Mecarini, F De Angelis, and E Di Fabrizio. Bacterial ratchet motors. *Proceedings of the National Academy of Sciences of the U.S.A*, 107(21):9541 – 9545, 00 2010.

[41] Andrey Sokolov, Mario M. Apodaca, Bartosz A. Grzybowski, and Igor S. Aranson. Swimming bacteria power microscopic gears. *Proceedings of the National Academy of Sciences*, 107(3):969–974, 2010.

[42] Gaszton Vizsnyiczai, Giacomo Frangipane, Claudio Maggi, Filippo Saglimbeni, Silvio Bianchi, and Roberto Di Leonardo. Light controlled 3D micromotors powered by bacteria. *Nature Communications*, 8(1):15974, 2017.

[43] Jochen Arlt, Vincent A. Martinez, Angela Dawson, Teuta Pilizota, and Wilson C. K. Poon. Painting with light-powered bacteria. *Nature Communications*, 9(1):768, 2018.

[44] Jessica M. Walter, Derek Greenfield, Carlos Bustamante, and Jan Liphardt. Light-powering Escherichia coli with proteorhodopsin. *Proceedings of the National Academy of Sciences*, 104(7):2408–2412, 2007.

[45] L Angelani, C Maggi, M L Bernardini, A Rizzo, and R Di Leonardo. Effective Interactions between Colloidal Particles Suspended in a Bath of Swimming Cells. *Physical Review Letters*, 107(13):138302, 09 2011.

[46] Shreyas Gokhale, Junang Li, Alexandre Solon, Jeff Gore, and Nikta Fakhri. Dynamic clustering of passive colloids in dense suspensions of motile bacteria. *Phys. Rev. E*, 105:054605, May 2022.

[47] D Ray, C Reichhardt, and C J Olson Reichhardt. Casimir effect in active matter systems. *Physical Review E*, 90(1):013019, 07 2014.

[48] Raymond Adkins, Itamar Kolvin, Zhihong You, Sven Witthaus, M Cristina Marchetti, and Zvonimir Dogic. Dynamics of active liquid interfaces. *Science*, 377(6607):768–772, 2022.

[49] Megan E. Szakasits, Wenxuan Zhang, and Michael J. Solomon. Dynamics of Fractal Cluster Gels with Embedded Active Colloids. *Physical Review Letters*, 119(5):058001, 2017.

[50] Megan E. Szakasits, Keara T. Saud, Xiaoming Mao, and Michael J. Solomon. Rheological implications of embedded active matter in colloidal gels. *Soft Matter*, 15(40):8012–8021, 2019.

[51] Keara T Saud, Mahesh Ganesan, and Michael J Solomon. Yield stress behavior of colloidal gels with embedded active particles. *Journal of Rheology*, 65(2):225–239, 2021.

[52] S.K Friedlander and C.S Wang. The self-preserving particle size distribution for coagulation by brownian motion. *Journal of Colloid and Interface Science*, 22(2):126–132, 1966.

[53] Srinivas Vemury and Sotiris E. Pratsinis. Self-preserving size distributions of agglomerates. *Journal of Aerosol Science*, 26(2):175–185, 1995.

[54] Steffen Rulands, Fabienne Lescroart, Samira Chabab, Christopher J. Hindley, Nicole Prior, Magdalena K. Sznurkowska, Meritxell Huch, Anna Philpott, Cedric Blanpain, and Benjamin D. Simons. Universality of clone dynamics during tissue development. *Nature Physics*, 14(5):469–474, 2018.

[55] J. Adler and Bonnie Templeton. The Effect of Environmental Conditions on the Motility of Escherichia coli. *Journal of General Microbiology*, 46(2):175–184, 1967.

[56] Tohru Minamino, Yasuo Imae, Fumio Oosawa, Yuji Kobayashi, and Kenji Oosawa. Effect of Intracellular pH on Rotational Speed of Bacterial Flagellar Motors†. *Journal of Bacteriology*, 185(4):1190–1194, 2003.

[57] R. Di Leonardo, D. Dell'Arciprete, L. Angelani, and V. Iebba. Swimming with an Image. *Physical Review Letters*, 106(3):038101, 2011.

[58] Eric Lauga, Willow R. DiLuzio, George M. Whitesides, and Howard A. Stone. Swimming in Circles: Motion of Bacteria near Solid Boundaries. *Biophysical Journal*, 90(2):400–412, 2006.

[59] Antoine Lagarde, Noémie Dagès, Takahiro Nemoto, Vincent Démery, Denis Bartolo, and Thomas Gibaud. Colloidal transport in bacteria suspensions: from bacteria collision to anomalous and enhanced diffusion. *Soft Matter*, 16(32):7503–7512, 2020.

[60] A. E. Patteson, A. Gopinath, M. Goulian, and P. E. Arratia. Running and tumbling with E. coli in polymeric solutions. *Scientific Reports*, 5(1):15761, 2015.

[61] Roberto Cerbino and Veronique Trappe. Differential Dynamic Microscopy: Probing Wave Vector Dependent Dynamics with a Microscope. *Physical Review Letters*, 100(18):188102, 00 2008.

[62] L. G. Wilson, V. A. Martinez, J. Schwarz-Linek, J. Tailleur, G. Bryant, P. N. Pusey, and W. C. K. Poon. Differential Dynamic Microscopy of Bacterial Motility. *Physical Review Letters*, 106(1):018101, 00 2011.

[63] David Germain, Mathieu Leocmach, and Thomas Gibaud. Differential dynamic microscopy to characterize Brownian motion and bacteria motility. *American Journal of Physics*, 84(3):202–210, 2016.

[64] M A Vigeant and R M Ford. Interactions between motile Escherichia coli and glass in media with various ionic strengths, as observed with a three-dimensional-tracking microscope. *Applied and Environmental Microbiology*, 63(9):3474–3479, 1997.

[65] Albert T. Poortinga, Rolf Bos, Willem Norde, and Henk J. Busscher. Electric double layer interactions in bacterial adhesion to surfaces. *Surface Science Reports*, 47(1):1–32, 2002.

[66] Aidan T. Brown, Ioana D. Vladescu, Angela Dawson, Teun Vissers, Jana Schwarz-Linek, Juho S. Lintuvuori, and Wilson C. K. Poon. Swimming in a crystal. *Soft Matter*, 12(1):131–140, 2015.

[67] Jan Brugues and Daniel Needleman. Physical basis of spindle self-organization. *Proceedings of the National Academy of Sciences of the U.S.A*, 111(52):18496 – 18500, 12 2014.

[68] Torsten Wittmann, Anthony Hyman, and Arshad Desai. The spindle: a dynamic assembly of microtubules and motors. *Nature Cell Biology*, 3(1):E28 – E34, 01 2001.

[69] Clifford P Brangwynne, Gijsje H Koenderink, Frederick C MacKintosh, and David A Weitz. Cytoplasmic diffusion: molecular motors mix it up. *The Journal of Cell Biology*, 183(4):583 – 587, 11 2008.

[70] Ming Guo, Allen J Ehrlicher, Mikkel H Jensen, Malte Renz, Jeffrey R Moore, Robert D Goldman, Jennifer Lippincott-Schwartz, Frederick C MacKintosh, and David A Weitz. Probing the Stochastic, Motor-Driven Properties of the Cytoplasm Using Force Spectrum Microscopy. *Cell*, 158(4):822 – 832, 08 2014.

[71] Ludovic Berthier and Jorge Kurchan. Non-equilibrium glass transitions in driven and active matter. *Nature Physics*, 9(5):310 – 314, 2013.

[72] Patrick Pietzonka, Etienne Fodor, Christoph Lohrmann, Michael E. Cates, and Udo Seifert. Autonomous Engines Driven by Active Matter: Energetics and Design Principles. *Physical Review X*, 9(4):041032, 2019.

[73] Yi Peng, Zhengyang Liu, and Xiang Cheng. Imaging the emergence of bacterial turbulence: Phase diagram and transition kinetics. *Science Advances*, 7(17):eabd1240, 2021.

[74] Koblan Wilfried Ebagninin, Adel Benchabane, and Karim Bekkour. Rheological characterization of poly(ethylene oxide) solutions of different molecular weights. *Journal of Colloid and Interface Science*, 336(1):360–367, 2009.

[75] Hilding Faxen. Der Widerstand gegen die Bewegung einer starren Kugel in einer zahen Flussigkeit, die zwischen zwei parallelen ebenen Wanden eingeschlossen ist. *Annalen der Physik*, 373(10):89–119, 00 1922.

[76] Alison E. Patteson, Arvind Gopinath, Prashant K. Purohit, and Paulo E. Arratia. Particle diffusion in active fluids is non-monotonic in size. *Soft Matter*, 12(8):2365–2372, 2016.

[77] J. Schwarz-Linek, C. Valeriani, A. Cacciuto, M E Cates, D Marenduzzo, A. N. Morozov, and W. C. K. Poon. Phase separation and rotor self-assembly in active particle suspensions. *Proceedings Of The National Academy Of Sciences Of The United States Of America*, 109(11):4052 – 4057, 2012.

[78] Matthew Spellings, Michael Engel, Daphne Klotsa, Syeda Sabrina, Aaron M Drews, Nguyen H P Nguyen, Kyle J M Bishop, and Sharon C Glotzer. Shape control and compartmentalization in active colloidal cells. *Proceedings Of The National Academy Of Sciences Of The United States Of America*, 112(34):E4642 – E4650, 08 2015.

[79] Nguyen H. P. Nguyen, Daphne Klotsa, Michael Engel, and Sharon C. Glotzer. Emergent Collective Phenomena in a Mixture of Hard Shapes through Active Rotation. *Physical Review Letters*, 112(7):075701, February 2014.

[80] Alexander P Petroff, Xiao-Lun Wu, and Albert Libchaber. Fast-Moving Bacteria Self-Organize into Active Two-Dimensional Crystals of Rotating Cells. *Physical Review Letters*, 114(15):158102, 04 2015.

[81] Clare J. Dibble, Michael Kogan, and Michael J. Solomon. Structure and dynamics of colloidal depletion gels: Coincidence of transitions and heterogeneity. *Physical Review E*, 74(4):041403, 2006.

[82] S Torquato and M Avellaneda. Diffusion and reaction in heterogeneous media: Pore size distribution, relaxation times, and mean survival time. *The Journal of Chemical Physics*, 95(9):6477–6489, 1991.

[83] D Zeb Rocklin, Lilian Hsiao, Megan Szakasits, Michael J Solomon, and Xiaoming Mao. Elasticity of colloidal gels: structural heterogeneity, floppy modes, and rigidity. *Soft matter*, 17(29):6929–6934, 2021.

[84] Jader Colombo, Asaph Widmer-Cooper, and Emanuela Del Gado. Microscopic Picture of Cooperative Processes in Restructuring Gel Networks. *Physical Review Letters*, 110(19):198301, 2013.

[85] Sophie Ramananarivo, Etienne Ducrot, and Jeremie Palacci. Activity-controlled annealing of colloidal monolayers. *Nature Communications*, 10(1):3380, 07 2019.

[86] B. van der Meer, L. Filion, and M. Dijkstra. Fabricating large two-dimensional single colloidal crystals by doping with active particles. *Soft Matter*, 12(14):3406–3411, 2016.

[87] Ahmad K Omar, Yanze Wu, Zhen-Gang Wang, and John F Brady. Swimming to Stability: Structural and Dynamical Control via Active Doping. *Acs Nano*, 13(1):560–572, 12 2018.

[88] Kiichiro Taniguchi, Reo Maeda, Tadashi Ando, Takashi Okumura, Naotaka Nakazawa, Ryo Hatori, Mitsutoshi Nakamura, Shunya Hozumi, Hiroo Fujiwara, and Kenji Matsuno. Chirality in Planar Cell Shape Contributes to Left-Right Asymmetric Epithelial Morphogenesis. *Science*, 333(6040):339–341, 2011.

[89] Shunya Hozumi, Reo Maeda, Kiichiro Taniguchi, Maiko Kanai, Syuichi Shirakabe, Takeshi Sasamura, Pauline Spéder, Stéphane Noselli, Toshiro Aigaki, Ryutaro Murakami, and Kenji Matsuno. An unconventional myosin in Drosophila reverses the default handedness in visceral organs. *Nature*, 440(7085):798–802, 2006.

[90] Tzer Han Tan, Alexander Mietke, Junang Li, Yuchao Chen, Hugh Higinbotham, Peter J. Foster, Shreyas Gokhale, Jörn Dunkel, and Nikta Fakhri. Odd dynamics of living chiral crystals. *Nature*, 607(7918):287–293, 2022.

[91] Jörn Dunkel, Victor B. Putz, Irwin M. Zaid, and Julia M. Yeomans. Swimmer- tracer scattering at low Reynolds number. *Soft Matter*, 6(17):4268–4276, 2010.

[92] Alexander Morozov and Davide Marenduzzo. Enhanced diffusion of tracer particles in dilute bacterial suspensions. *Soft Matter*, 10(16):2748–2758, 2014.

[93] Dmitri O. Pushkin and Julia M. Yeomans. Fluid Mixing by Curved Trajectories of Microswimmers. *Physical Review Letters*, 111(18):188101, 2013.

[94] Dmitri O. Pushkin, Henry Shum, and Julia M. Yeomans. Fluid transport by individual microswimmers. *Journal of Fluid Mechanics*, 726(18):5–25, 2013.

[95] Arnold J. T. M. Mathijssen, Raphaël Jeanneret, and Marco Polin. Universal entrainment mechanism controls contact times with motile cells. *Physical Review Fluids*, 3(3):033103, 2018.

[96] M. V. Smoluchowski. Drei Vortrage uber Diffusion, Brownsche Bewegung und Koagulation von Kolloidteilchen. *Zeitschrift fur Physik*, 17:557–585, January 1916.

[97] Ivan Palaia and Anđela Šarić. Controlling cluster size in 2D phase-separating binary mixtures with specific interactions. *The Journal of Chemical Physics*, 156(19):194902, 2022.

[98] A. P. Thompson, H. M. Aktulga, R. Berger, D. S. Bolintineanu, W. M. Brown, P. S. Crozier, P. J. in 't Veld, A. Kohlmeyer, S. G. Moore, T. D. Nguyen, R. Shan, M. J. Stevens, J. Tranchida, C. Trott, and S. J. Plimpton. LAMMPS - a flexible simulation tool for particle-based materials modeling at the atomic, meso, and continuum scales. *Comp. Phys. Comm.*, 271:108171, 2022.

[99] Alexander Stukowski. Visualization and analysis of atomistic simulation data with OVITO-the Open Visualization Tool. *Modelling and Simulation in Materials Science and Engineering*, 18(1):015012, 2010.

[100] Linda M. Seymour, Janille Maragh, Paolo Sabatini, Michel Di Tommaso, James C. Weaver, and Admir Masic. Hot mixing: Mechanistic insights into the durability of ancient Roman concrete. *Science Advances*, 9(1):eadd1602, 2023.